Assessment of the force spectrum induced by turbulence on an array of cylinders in incompressible axial flow

Pieter Aerts

Supervisors: Prof. dr. ir. Joris Degroote, Prof. dr. ir. Jan Vierendeels
Counsellor: Ir. Jeroen De Ridder

Master's dissertation submitted in order to obtain the academic degree of
Master of Science in Electromechanical Engineering

Department of Flow, Heat and Combustion Mechanics
Chairman: Prof. dr. ir. Jan Vierendeels
Faculty of Engineering and Architecture
Academic year 2014-2015

UNIVERSITEIT
GENT

Assessment of the force spectrum induced by turbulence on an array of cylinders in incompressible axial flow

Pieter Aerts

Supervisors: Prof. dr. ir. Joris Degroote, Prof. dr. ir. Jan Vierendeels
Counsellor: Ir. Jeroen De Ridder

Master's dissertation submitted in order to obtain the academic degree of
Master of Science in Electromechanical Engineering

Department of Flow, Heat and Combustion Mechanics
Chairman: Prof. dr. ir. Jan Vierendeels
Faculty of Engineering and Architecture
Academic year 2014-2015

UNIVERSITEIT
GENT

Preface

A thesis is the icing on the cake for every student. As someone with interests in nuclear engineering and fluid mechanics, this subject was just right for me. Apart from the knowledge I gained during the writing and performing the simulations, especially a feeling of pride remains. Pride that I was able to create a scientific work in just under a year time. Proud of my thesis, like a parent of its child. A thesis is the icing on the cake for every student, and why would I be any different?

I would like to thank both professor J. Degroote and professor J. Vierendeels for giving me the opportunity to write this thesis. Without their letters of approval, I would have been unable to gain access to extensive calculation units, causing the computational capacity to be inadequate to complete this work. Also thanks for aiding and commenting on my work, essentially upgrading my thesis.

Special thanks go out to Jeroen De Ridder for bringing the notion of counsellor to a whole new level. Thank you for being there, even in the weekends, and helping me with all kinds of issues, both in flow and engineering applications, as with the software. The learning curve of the OpenFOAM flow simulation program became much less steep because of you. I really appreciated the last-minute proofreads, and your comments greatly enhanced the thesis.

I would have never gotten this far if it wasn't for my parents, who allowed me to follow my dreams and supported me both psychologically and financially throughout my studies. Moral support also came from friends, especially Enya De Winne, Zoé Claeys, the guys from Stranger Dimensions, Cedric De Pauw and Laurens De Graeve. The latter two deserve an additional word of gratitude, for their help with the lay-out.

I conclude these acknowledgements by wishing the best of luck to Laurent De Moerloose, who will be continuing this thesis subject in the academic year 2015-2016, under the counselling of Jeroen De Ridder, and supervised by both professor J. Degroote and J. Vierendeels.

Permission to lease-lend

Ghent, 22^{th} of May, 2015

The author

Pieter Aerts

Assessment of the force spectrum induced by turbulence on an array of cylinders in incompressible axial flow

Pieter Aerts

Supervisors: Prof. dr. ir. Joris Degroote, Prof. dr. ir. Jan Vierendeels
Counsellor: Ir. Jeroen De Ridder

Master's dissertation submitted in order to obtain the academic degree of
Master of Science in Electromechanical Engineering

Department of Flow, Heat and Combustion Mechanics
Chairman: Prof. dr. ir. Jan Vierendeels
Faculty of Engineering and Architecture
Academic year 2014-2015

Abstract

Arrays of cylinders, subjected to turbulent axial flows, are often encountered in nuclear reactor cores. The flow induces pressure fluctuations on the cylinders, causing them to vibrate slightly. These vibrations give rise to long-term failure mechanisms, like fatigue, and fretting due to impacting of closely spaced cylinders. Simulations evaluating the distribution of pressure fluctuations amplitude and frequency on the cylinder surface, are performed on a realistic nuclear core geometry. The frequency and position dependency of the pressure fluctuations is extracted, indicating that larger vortices induce larger pressures. A parameter study, extracting the influence of the Reynolds number, the spacing between cylinders, and the array configuration, is performed. The induced pressure amplitude decreases with decreasing Reynolds number and increasing array spacing. The correlation between pressure fluctuations is strongly dependent on both the Reynolds number and array spacing. The latter also determines the existence of a vortex street: a sequence of alternating large scale vortices, enhancing mixing between subchannels, caused by a Kelvin-Helmholtz instability in a mixing layer. The methods used in this thesis can be used to analyse nuclear reactor cores with respect to pressure fluctuations and structural safety.

Keywords

Flow induced vibrations, Large-Eddy Simulation, spectral analysis, turbulent vortices, vortex street

Assessment of the force spectrum induced by turbulence on an array of cylinders in incompressible axial flow

Pieter Aerts

Supervisors: Jeroen De Ridder, Joris Degroote, Jan Vierendeels

Abstract - **Arrays of cylinders, subjected to turbulent axial flows, are often encountered in nuclear reactor cores. The flow induces pressure fluctuations on the cylinders, causing them to vibrate slightly. These vibrations give rise to long-term failure mechanisms, like fatigue, and fretting due to impacting of closely spaced cylinders. Simulations evaluating the distribution of pressure fluctuations amplitude and frequency on the cylinder surface, are performed on a realistic nuclear core geometry. The frequency and position dependency of the pressure fluctuations is extracted, indicating that larger vortices induce larger pressures. A parameter study, extracting the influence of the Reynolds number, the spacing between cylinders, and the array configuration, is performed. The induced pressure amplitude decreases with decreasing Reynolds number and increasing array spacing. The correlation between pressure fluctuations is strongly dependent on both the Reynolds number and array spacing. The latter also determines the existence of a vortex street: a sequence of alternating large scale vortices, enhancing mixing between subchannels, caused by a Kelvin-Helmholtz instability in a mixing layer. The methods used in this thesis can be used to analyse nuclear reactor cores with respect to pressure fluctuations and structural safety.**

Keywords - **Flow induced vibrations, Large-Eddy Simulation, spectral analysis, turbulent vortices, vortex street**

introduction

Cylinder bundles subjected to axial flow, are a geometry often encountered in nuclear reactor cores (ref. 5) and tube-in-tube heat exchangers. The vortices present in the turbulent flow, induce pressure fluctuations on the cylindrical surfaces, and exert forces on the structure. Due to these fluctuating forces, the cylinders start vibrating. However small, these vibrations can lead to structural failure in the long term, e.g. fatigue, or fretting due to impacting on adjacent cylinders or spacers (ref. 6).

This thesis evaluates the forces exerted by the flow on the cylinders, by computing the pressures induced on the cylinder walls. Wall-pressure frequency spectra are obtained and analysed, extracting the influence of the position on the cylinder, Reynolds number, array spacing, and array configuration on the pressure magnitude, its frequency distribution, and the spatial coherence between pressure fluctuations.

To obtain these spectral distributions, LES (large eddy simulations) are performed on cases with different geometric and flow parameters. Spectra from cases, each with a different Reynolds number, array spacing or array configuration, are compared to the spectra obtained with the reference case.

The simulations were performed with incompressible fluids with constant flow properties, in the absence of heat transfer, on rigid cylinders.

Methodology

Out of all different CFD (computational fluid dynamics) methods, LES is the most suitable for this particular study. RANS (Reynolds-averaged Navier Stokes) models all turbulent scales, and is less suited for boundary layer analysis, which is a prerequisite to study the wall-pressures. with DNS (direct Navier-Stokes) simulations, highly accurate results can be obtained, but at the cost of very high computation loads, as all turbulent scales are resolved. LES is a trade-off between both, and resolves only the large turbulent scales, while modelling the others. It combines sufficiently accurate results with acceptable computational loads.

The flow domain on which the LES simulations are performed, contains only one cylinder. This significantly reduces the grid size, hence the computational load. However, the interpretation of the results is less straightforward, and it should be checked if this flow domain is representative for the entire array. An example of such a flow domain is given in Figure 1 in solid line. On this figure, the cylinder diameter D and pitch P are indicated.

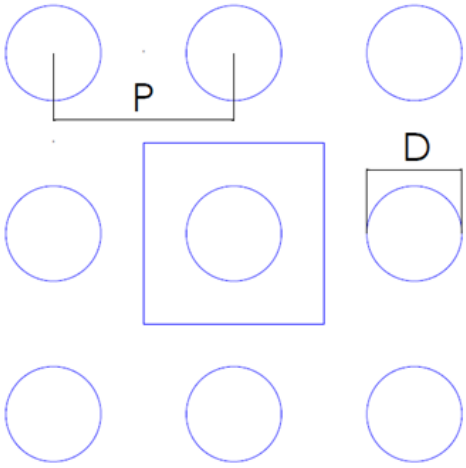

Figure 1: Top view of square array flow domain, with indication of the cylinder diameter D and pitch P.

The flow domain side walls coincide with the midlines between adjacent rods. The flow domain length L is chosen to be $15D_h$, with $D_h = 4\frac{P^2 - \frac{\pi}{4}D^2}{\pi D}$ the hydraulic diameter of a square array.

It was confirmed that the flow domain length is large enough to allow large scale vortices to be present in the simulations. Grid spacings are taken from the literature (ref. 7) and the convergence was studied by progressively refining them. The dimensionless grid spacings are set at $\Delta x^+ = 100$, $\Delta y^+ = 2$ and $\Delta z^+ = 20$. Although the solution is not completely grid independent, the grid dependency is only weak, which is sufficient for LES simulations. The axial resolution limits the scope to Strouhal numbers $St = \frac{fD_h}{U}$, the dimensionless frequency, up to 1.25, with f the fluctuation frequency and U the flow velocity. Larger frequency vortices have lower length scales and do not span multiple grid cells.

On the cylinder wall, a no-slip condition is imposed, which means that the velocity is zero on the surface. Between all opposite flow domain planes, such as inflow, outflow and side planes, periodic boundary conditions are imposed. The planes are then connected in terms of flow path while separated in space: fluid flowing out of one plane enters the other one and vice versa. The periodic boundary conditions between the inlet and outlet planes simulate infinitely long cylinders, eliminating entrance effects. Those between opposite side planes, simulate the continuity of the array. However, they also have an impact on the solution.

The initial velocity field is constructed by a random generator: on a uniform axial velocity field, random perturbations are imposed. They aid the transition to a fully developed turbulent regime. All other flow parameters are chosen uniform throughout the flow domain, but their initial state is quickly forgotten by the flow. To couple the flow parameters, some adaptation time is needed.

The solver is an LES solver, resolving the large scales, with dynamic Lagrangian averaging and a Smagorinski sub-grid scale model, modelling the small scales. The solver introduces a virtual pressure difference between the inlet and outlet plane, because the boundary conditions would otherwise eliminate the driving force.

The studied wall-pressure spectra are Power Spectral Density (PSD), Cross-Spectral Density (CSD) and coherence (γ) functions. They originate from a Fourier transform. The Discrete Fourier Transform (DFT) X of a time signal x obtained at N time steps,

is defined as

$$X_m = \sum_{k=0}^{N-1} x(k) exp\left(-j2\pi \frac{mk}{N}\right) , \quad m = 0, ..., N-1 . \tag{1}$$

Nyquist's theorem (ref. 4) limits the frequency resolution and lower and upper frequency data as a function of the number of time steps and time batch length.
The PSD auto-correlates the Fourier transform, and is given as

$$PSD_{\vec{x_1}\vec{x_1}}(St) = 2\left(X_{\vec{x_1}}(St) X^*_{\vec{x_1}}(St)\right)\frac{f_s}{N} , \tag{2}$$

with x_1 a space vector. The spectrum amplitude is normalised by $\frac{f_s}{N}$: the ratio of sample frequency to the number of samples. The PSD visualizes the pressure magnitude as a function of position on the cylinder and fluctuation frequency.
The CSD cross-correlates the Fourier transform at different points x_1 and x_2. It is defined as

$$CSD_{\vec{x_1}\vec{x_2}}(St) = 2\left(X_{\vec{x_1}}(St) X^*_{\vec{x_2}}(St)\right)\frac{f_s}{N} , \tag{3}$$

where X^* represents the complex conjugate of X. In fluid mechanics, for pressure spectra, both PSD and CSD functions are made dimensionless by a factor $\frac{1}{\rho^2 U^3 D_h}$, with ρ the fluid density.
The coherence is a dimensionless representation of the CSD, normalised by the PSD in both points (ref. 1):

$$\gamma_{\vec{x_1}\vec{x_2}}(St) = \frac{CSD_{\vec{x_1}\vec{x_2}}(St)}{\sqrt{PSD_{\vec{x_1}\vec{x_1}}(St) PSD_{\vec{x_2}\vec{x_2}}(St)}} . \tag{4}$$

It represents the correlation between the pressure fluctuations at different positions on the cylinder, per frequency band.
To eliminate outliers and reduce variance, the spectra are averaged over space and time. The time averaging, splitting the time data of length t_0 into N time batches of length $\frac{t_0}{N}$, inherently causes a reduction in frequency resolution and limits the minimal frequency in the spectra.

The spectra are a function of the frequency, represented dimensionless by the Strouhal number, and one - for a PSD -, or two - for a CSD or coherence - points on the cylinder surface. The position on the cylinder is represented by a circumferential coordinate θ and an axial coordinate x. Because of the boundary conditions and the method of spectra calculation, the axial coordinate loses its meaning as absolute coordinate, and is only present as an axial distance between two points $\overline{x}$. The circumferential position on the cylinder surface for a square array, is visualised in Figure 2, with in blue the simulated flow domain, and in black the flow domain as it is interpreted due to the boundary conditions.

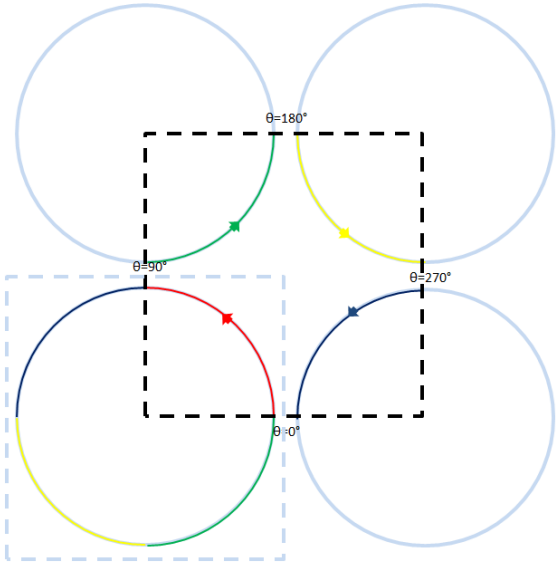

Figure 2: A square array configuration with the studied flow domain in blue dashed lines. A point on the flow domain cylinder in the green, yellow, or blue region is equivalent to the point on another cylinder arc of the same colour, as indicated by the evolution of θ. An equivalent flow domain is drawn in black dashed lines.

Results and discussion

In a first study, the influence of the position and frequency on the pressure amplitudes and their correlation in different points, is extracted qualitatively. To validate the results, the reference case is compared against Curling's correlation (ref. 2), which is based on experiments on a similar array geometry.
A second study compares cases with a variation in Reynolds number, cylinder spacing, and array configuration. The influence of these parameters on the pressure amplitude and their correlation in different

Table 1: The flow and geometric properties of the different case.

Name	Config.	D [m]	P [m]	D_h [m]	U [$\frac{m}{s}$]	Re_{D_h} [-]
reference	□	0.2	0.217	0.1	140	14,000
Re 10000	□	0.2	0.217	0.1	100	10,000
Re 6800	□	0.2	0.217	0.1	68	6,800
PD 1.3	□	0.2	0.26	0.2304	60	14,000
hexagonal	△	0.2	0.2332	0.1	140	14,000

points is extracted qualitatively.
The relevant geometric and flow parameters of the different cases are given in Table 1, with $Re_{D_h} = \frac{D_h U}{\nu}$ the Reynolds number, and ν the kinematic viscosity.

Power spectral density spectra

The PSD of the reference case is given in Figure 3.

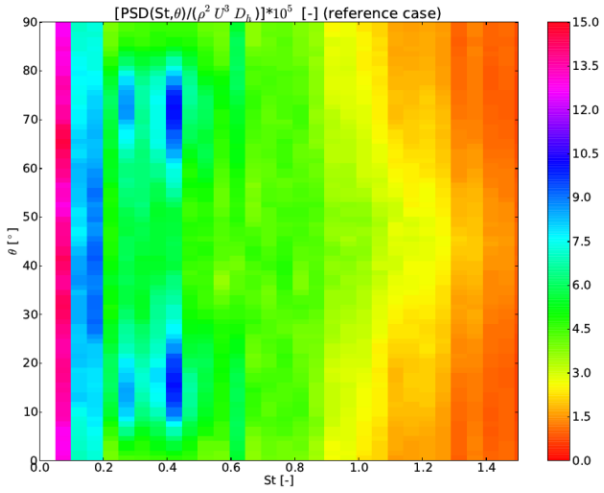

Figure 3: Dimensionless PSD contour plot for the reference case.

The pressure amplitude is high at low frequencies: large scale vortices induce large pressure fluctuations. At higher frequencies, the pressure amplitude first decreases, but then shows a maximum at a Strouhal number in between 0.25 and 0.45, near adjacent cylinders. This is because an important vortex street is present near the gap region, with its axis of convection at the position of this maximum. The velocity contours on a side plane of the flow domain for the reference case, are given in Figure 4.

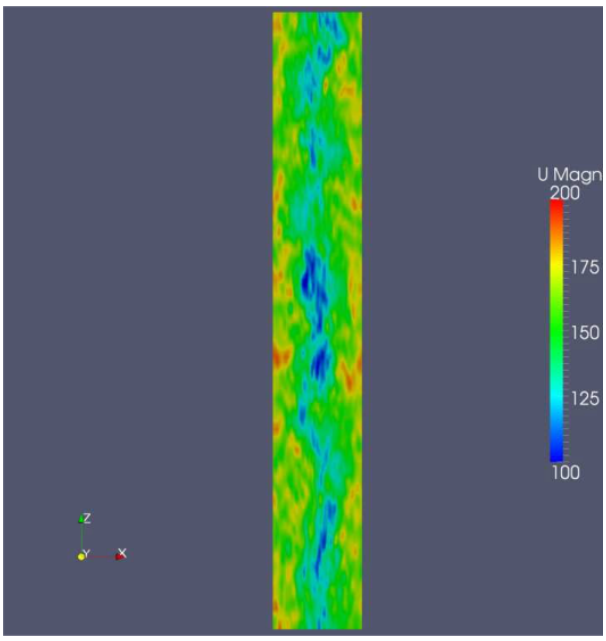

Figure 4: The velocity magnitude along a flow domain side plane.

The zigzagging velocity contour indicates a vortex street: an alternating sequence of large scale vortices, enhancing mixing between adjacent subchannels. The vortex street results from a Kelvin-Helmholtz instability in the mixing layer between the high-velocity subchannel and low-velocity gap flows (ref. 5).

At even higher frequencies, the pressure amplitudes drop to zero, but the spectrum remains broader in the subchannel region.

At lower Reynolds numbers, the global pressure amplitude drops, but the distribution over the dimensionless frequency range is not influenced. For less closely spaced arrays, the pressure amplitude drops, and the pressure peak is shifted towards larger Strouhal numbers, and towards the subchannel region.
For both decreasing Reynolds number and increas-

ing free-flow section, the pressure drop over a unit length decreases. this indicates a weakening of the turbulence intensity and vortex street, and results in lower pressure amplitudes. The shift in maximum is because the vortex street is absent in more open geometries.

Coherence spectra

The coherence between pressures in points at the same axial coordinate, and one point's circumferential position fixed in the subchannel region, is given in Figure 5.

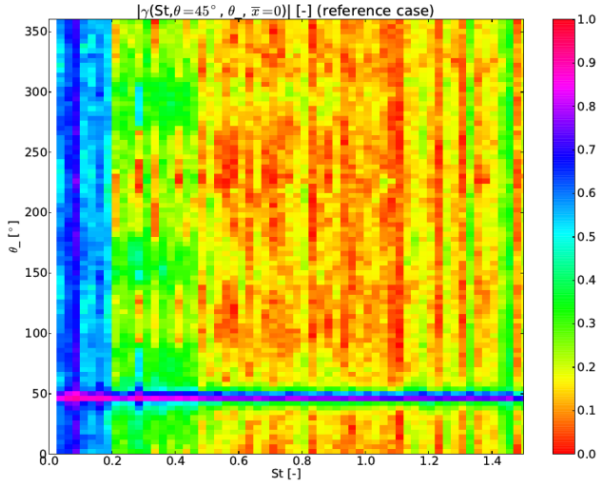

Figure 5: Coherence amplitude contour plot between points at the same axial coordinate, and one point's circumferential position fixed in the subchannel region, for the reference case.

The cross-correlation between pressures is highest at points on the same or adjacent cylinders, and small in the gap regions. At high frequencies, the coherence is no longer significant. Smaller vortices do not exists at both sides of a gap simultaneously, and their spanwise length is too small to induce pressures at diagonally opposite cylinders. The high coherence at $\theta' = 45°$ is the CSD equalling the PSD at $\theta = \theta'$. The coherence phase is identically zero for $\overline{x} = 0$: the vortices cross the points simultaneously in time. For decreasing Reynolds number or increasing cylinder spacing, the coherence amplitude increases over the entire circumferential and frequency range. In both cases, the main flow velocity decreases and the spanwise length of the vortices increases, allowing them to induce pressures over longer distances.

The coherence contour plots of the reference case for two points at $\theta = 0°$, separated over an axial distance $\overline{x}$, are given in Figure 6 and 7.

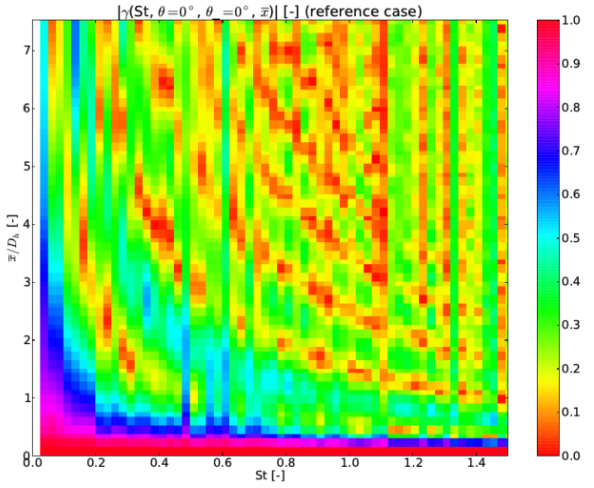

Figure 6: Coherence amplitude contour plot between points in the same gap region, separated over an axial distance, for the reference case.

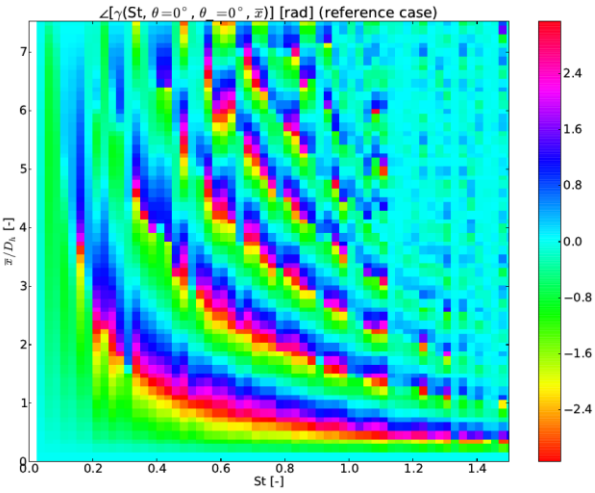

Figure 7: Coherence phase contour plot between points in the same gap region, separated over an axial distance, for the reference case.

Coherence amplitudes are high for low Strouhal and axial distance combinations. This shows the dis-

sipation of small vortices over distance, and verifies Curling's observation that the coherence is proportional to $exp(-j2\pi f\frac{\overline{x}}{U})$ (ref. 2), with $j = \sqrt{-1}$ the imaginary unit. In (ref. 3), the bands in the spectra are explained as the result of the convection of a series of irrotational vortices.
The coherence plots for varying Reynolds number or array spacing do not vary significantly. This is however only true on a dimensionless frequency axis: in an absolute sense, the eddy turnover time $\frac{l}{U}$ or the amount of periods completed per time unit, with l the length scale of the vortex (ref. 8), increases for lower flow velocities, as the time to convect these vortices over the same distance increases.
For triangular arrays, the vortices are correlated over significantly smaller distances.

Conclusions

In this thesis, the forces on a cylinder bundle, induced by an axial flow, are evaluated by computing the frequency spectra of the pressures on the cylinder walls. These pressures need to be limited to avoid excessive cylinder vibration, causing failure in the long run. The influence of the position, Reynolds number, pitch-over-diameter ratio, and array configuration on the pressure fluctuation amplitude and frequency, are extracted by performing LES simulations on a flow domain containing a single cylinder.

In closely spaced arrays, a vortex street, resulting from a Kelvin-Helmholtz instability in the mixing layer between the high-velocity subchannel and low-velocity gap flow, is responsible for high pressure fluctuations, especially in the low frequency range. The convection and dissipation of vortices is visualized in the coherence spectra, correlating pressures in points at different axial positions along the cylinder surface.

An open geometry in a low Reynolds number flow limits the pressure fluctuation amplitudes: the reduced Reynolds number and larger flow section limit the turbulence in the main flow, while the latter also reduces the importance of the vortex street.

As the major pressure amplitudes are induced by the largest vortices, eliminating these vortices, e.g. by introducing mechanical obstructions in the flow, might be most advantageous from a structural point of view. However, these vortices significantly enhance the mixing between subchannels, and are desired for heat transfer applications.

References

1. J. S. Bendat & A. G. Piersol, (2010), Random Data: Analysis and Measurement Procedures, 4th edition, Wiley

2. L. R. Curling & M. P. Paidoussis, (1991), Measurements and characterisation of wall-pressure fluctuations on cylinders in a bundle in turbulent axial flow; Part 1: Spectral characteristics, Journal of Sound and Vibration (1992) 157 (3) pg 405-433

3. J. De Ridder & J. Degroote & K. Van Tichelen et. al, (2015), Predicting turbulence-induced vibration in axial annular flow by means of large-eddy simulations, Journal of Fluids and Structures, Draft under review

4. G. Heinzel & A. Rüdiger & R. Schilling, (2002), Spectral and spectral density estimation by the Discrete Fourier Transform (DFT), including a comprehensive list of window functions and some new flat-top windows, Max-Planck Institut für gravitationphysik, Hannover (Germany)

5. L. Meyer, (2010), From discovery to recognition of periodic large scale vortices in rod bundles as source of natural mixing between subchannels - a review, Nuclear Engineering and Design 240 (2010) 1575-1588

6. M. P. Paidoussis, (2004), Fluid-structure interactions: slender structures and axial flow, Volume 2, Elsevier academic press, London, Great Britain

7. U. Piomelli, (2012), Large-eddy simulation of turbulent flows part 1: introduction, Von Karman institute for fluid dynamics: lecture series 2012, Queens university, Lecture in Sint-Genesius-Rode, Belgium

8. `http://www.eng.utah.edu/~mcmurtry/Turbulence/turblt.pdf`, 16/05/2015

Contents

List of Figures

List of Tables

Abbreviations

CFD : computational fluid dynamics
CSD : cross-spectral density
DFT : discrete Fourier transform
DNS : direct Navier-Stokes
LES : large eddy simulation
PSD : power-spectral density
SGS : sub-grid scale
VKI : Von Karman institute

List of symbols

General Symbols

A : the free-flow section $[m^2]$
$A_{cylinder}$: the circumferential cylinder surface area $[m^2]$
a : coefficient in Curling's CSD-correlation $[-]$
B_y : the bias factor for cell widths in the radial direction $[-]$
b_s : coefficient in Curling's CSD-correlation $[-]$
C_s : the Smagorinski constant $[-]$
C_K : the Kolmogorov constant $[-]$
D : the cylinder diameter $[m]$
D : the flow domain
D_h : the hydraulic diameter $[m]$
$\frac{D}{Dt}$: the material derivative $[s^{-1}]$
E : general energy scale $[J]$
E : the tensor of the total error of the approximated Germano identity $[Pa]$
e : the error tensor of the approximated Germano identity $[Pa]$
F_{shear} : the shear force along the cylinder surface $[N]$
f : general function
f : the frequency $[Hz]$
f_{LM} : transported Lagrangian dynamic model parameter $[\frac{Pa^2}{s}]$
f_{MM} : transported Lagrangian dynamic model parameter $[\frac{Pa^2}{s}]$
f_{Ny} : the Nyquist frequency $[Hz]$
f_{res} : the frequency resolution $[Hz]$
f_s : the sampling frequency $[Hz]$
G : filtering function
h : the grid size $[m]$
j : the imaginary unit $[-]$

K_{max} : reference wave number $[m^{-1}]$
k : the wave number $[m^{-1}]$
L : general length scale $[m]$
L : the resolved turbulent stress tensor $[Pa]$
L : the cylinder length $[m]$
l : length scale $[m]$
l : coefficient in Curling's CSD-correlation $[-]$
l_s : the characteristic length scale $[m]$
M : Lagrangian dynamic model tensor $[Pa]$
N : the number of time steps in a time series $[-]$
N : the grid size $[-]$
N_x : the number of cells in the longitudinal direction $[-]$
n : proportionality constant between the grid size and the filter width $[-]$
n : the number of time batches $[-]$
n : the cell-to-cell expansion ratio $[-]$
P : the array pitch $[m]$
P_w : the wetted perimeter $[m]$
p : the pressure $[Pa]$
q : the turbulent energy $[J]$
Re_x : the Reynolds number, based on a length scale x $[-]$
S : the strainrate tensor $[s^{-1}]$
St : the Strouhal number $[-]$
T : the subtest stress tensor $[Pa]$
T : a time interval $[s]$
t : time variable $[s]$
t : the length of the time domain $[s]$
t_L : the eddy turn-over time $[s]$
U : the fluid free-flow velocity $[\frac{m}{s}]$
U_c : the convection speed $[\frac{m}{s}]$
u : the fluid velocity in the axial direction $[\frac{m}{s}]$
u_τ : the shear velocity $[\frac{m}{s}]$
W : weighing function $[-]$
X : the complex Fourier transform of a time series x
x : the axial coordinate $[m]$
x : general space coordinate $[m]$
x : scalar time series
$\overline{x}$: the axial distance between two points $[m]$
y : the radial distance from the cylinder surface $[m]$
z : the circumferential distance $[m]$

z : function giving the pathline of a particle in the time $[m]$

γ : the coherence of a time signal $[-]$
$\overline{\Delta}$: the grid filter width $[m]$
$\widehat{\Delta}$: the test filter width $[m]$
δ : the chronecker delta $[-]$
ϵ : the turbulence dissipation rate $[\frac{m^2}{s^3}]$
ϵ_ν : the viscous dissipation rate $[\frac{m^2}{s^3}]$
ζ_1 : coefficient in Curling's CSD-correlation $[-]$
ζ_2 : coefficient in Curling's CSD-correlation $[-]$
θ : the circumferential coordinate $[rad$ or $^\circ]$
θ' : the circumferential coordinate $[rad$ or $^\circ]$
θ_d : the angular difference in Curling's CSD-correlation $[rad]$
κ : the turbulent structure wave number $[m^{-1}]$
λ : the spacing between two consecutive vortices in the same subchannel $[m]$
μ : the dynamic viscosity $[Pa \cdot s]$
ν : the kinematic viscosity $[\frac{m^2}{s}]$
ν_T : the eddy viscosity $[\frac{m^2}{s}]$
ρ : the gravimetric density $[\frac{kg}{m^3}]$
τ : the SGS stress tensor $[\frac{m^2}{s^2}]$
τ_w : the wall shear stress $[Pa]$
$\widehat{\tau}$: the subgrid stress tensor $[Pa]$
$\frac{\partial}{\partial x}$: the partial derivative to a variable x
ω : the radial frequency $[\frac{rad}{s}]$

Prescripts, subscripts and superscripts

Δ : cell width

$_0$: integral range parameter
$_{i,\ j,\ k}$: direction along a coordinate axis
$_{SGS}$: sub-grid scale variable
$_\tau$: variable based on the local friction

* : the complex conjugate
$^+$: dimensionless wall unit

$\overline{x}$: variable filtered by the grid filter
$\widehat{x}$: variable filtered by the test filter

Chapter 1

Literature review

The literature review starts with a section about the goal and the relevance of the thesis. The underlying fluid mechanics theory is described hereafter. In a third section, the definition and generation of frequency spectra is discussed.

1.1 Global introduction

The goal of this thesis is the study of axial flow over bundles of cylinders, and the vibration of these cylinders by forces exerted by the flow. The study of these axial-flow induced vibrations of slender structures has long been overshadowed by the study of cross-flow induced vibrations (ref. [15]). The vibration amplitudes of the latter are several orders of magnitudes larger, resulting in immediate and severe mechanical consequences. Axial-flow induced vibrations generally have much smaller vibration amplitudes, in the order of $10^{-3}D$ to $10^{-2}D$, with D the cylinder diameter. Therefore, failure of the structure occurs very gradually: mechanically by fretting, wear and fatigue, and chemically by stress-corrosion cracking. Another mode of failure by fluido-elastic instability, like buckling, only occurs at very high fluid velocities without practical value (ref. [15]) and is not treated in this thesis.

Two particular applications of closely spaced cylinder bundles in axial flow, are nuclear reactors and pipe-in-pipe heat exchangers. Both nuclear cores and heat exchangers nuclear cores have high life expectancies, and cylinder replacement is very costly or even impossible. Products contained in the cylinders must be confined at all costs, as spills might cause unwanted chemical reactions or release of radioactive substances. Even small vibration

amplitudes pose problems due to close cylinder spacing or vicinity of spacers separating cylinders. Impacting of cylinders onto each other or onto the spacers accelerates fretting and failure.
Although following simulations and results are equally valid for heat exchangers, the main focus is on nuclear applications. The square and triangular array configurations are frequently used in reactor cores and spent fuel pools (ref. [13]) and therefore studied here. A top view of these configurations is given in Figure 1.1. On this figure, the cylinder diameter D and the distance between adjacent cylinder midpoints - the pitch P - are indicated.

The vibrations induced by axial flow on slender structures are of a stochastic nature (ref. [15]). To cope with this randomness, probabilistic methods are employed. The power distribution of the vibrations over the frequency range is studied using frequency spectra. The coherence of different frequency vibrations at different locations and times is evaluated using power and cross-spectral density functions.

The incompressible fluid and adiabatic system assumptions are expected to strongly reduce the computational time, as the energy conservation equation is omitted and pressure wave effects do not occur. These assumptions presumably have little influence on the solution. Fluid densities are approximately constant at moderate temperatures. For cylinders emanating little or no heat, the system is approximately adiabatic, as the friction heat losses are negligible and fluid specific heat capacities are high.
The simulation of rigid cylinders prevents the study of the cylinder vibrations. However, the pressures on the cylinder surface give a good indication of the resulting cylinder motion. The influence of the cylinder vibration on the pressure distribution over its surface is negligible, as turbulence-induced vibrations have a one-way coupling between the flow and the structural motion: the turbulence influences the structural motion but not the other way around (ref. [18]). Rigid structures allow for stationary computational meshes, which strongly reduces computational load.

1.2 Fluid mechanics

The cause of the pressure fluctuations on the cylinder surface is discussed in this section. First, the phenomenon turbulence is treated, along with the boundary layer analysis and the vortex energy cascade. Further, a vortex street, specific for axial flow in cylinder bundles, is discussed. This phenomenon is the major contributor to the fluctuating pressure distribution on the cylinder surface.

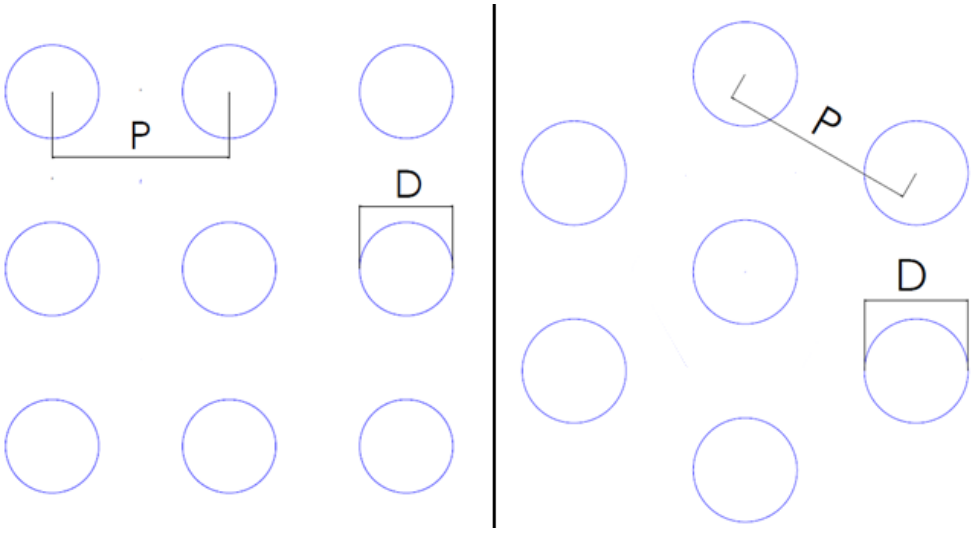

Figure 1.1: Top view of a square (left) and triangular (right) array configuration.

Many things in this chapter have been extracted from U. Piomelli, 2012 (ref. [16]). No further referrals to this work will be made.

1.2.1 Turbulence - Definition

An introductory course to the LES (large-eddy simulation) model lectured at the VKI (Von Karman Institute) postulates the following definition of turbulence: "*Turbulence is an irregular, chaotic state of fluid motion that occurs when the instabilities present in the initial or boundary conditions are amplified, and a self-sustained cycle is established in which turbulent eddies (coherent regions of vorticity) are generated and destroyed* ".

Important in this definition are the keywords 'chaotic' and 'irregular'. Turbulence exhibits a kind of randomness: it consists of coherent structures, turbulent eddies or vortices, random in location and time of occurrence, superposed on a random background motion. These structures are however not completely random in nature: the turbulent velocity fluctuations in different directions and in different points are correlated (ref. [17]).
The development of turbulence is largely influenced by the initial and boundary conditions and the details of the perturbations in them. Consequently, the flow field is extremely sensitive to these conditions: different solutions diverge exponentially in time, although the statistical flow properties are identical.

For turbulence to develop and be self-sustaining, the flows Reynolds number has to be

sufficiently large. this number is defined as

$$Re_L = \frac{\rho L U}{\mu} = \frac{L U}{\nu} \ , \tag{1.1}$$

where ρ, μ and $\nu = \frac{\mu}{\rho}$ are the fluid density, dynamic viscosity and kinematic viscosity respectively. U is the free-flow velocity, and L is a characteristic length scale (the length L of a flat plate, the diameter D of a pipe, or the hydraulic diameter $D_h = 4 \cdot \frac{A}{P_w}$ of more complex geometries, with A the free flow cross-section and P_w the wetted perimeter).

An important effect of turbulence is the enhanced mixing (ref. [17]). The increase in momentum transfer between different flow layers is of particular interest in the boundary layer, where it results in an increased friction between the solid body and the flow, leading to a higher skin friction coefficient.

1.2.2 Turbulence - Boundary layer

The boundary layer of a turbulent flow near a solid wall is usually subdivided in a number of layers and sub-layers, depending on the dimensionless wall units. The dimensionless velocity in these layers follows a characteristic pattern described by the law of the wall (ref. [17]).
Wall units are made dimensionless with the shear velocity u_τ and the characteristic length scale l_s, which are defined as

$$u_\tau = \sqrt{\frac{\tau_w}{\rho}} \text{ and } l_s = \frac{\nu}{u_\tau} \ , \tag{1.2}$$

with τ_w the wall shear stress.
With these quantities, the distance normal to the solid boundary - y - and the velocity parallel to the boundary - u - can be made dimensionless:

$$y^+ = \frac{y}{l_s} \text{ and } u^+ = \frac{u}{u_\tau} \ . \tag{1.3}$$

Dimensionless quantities are denoted by a superscript $^+$.

Starting from the solid boundary, the first layer encountered is the wall layer (Fig. 1.2). It comprises the bottom 10 to 20% of the boundary layer, or more general, the region where $y^+ < 400$. In this layer, large velocity gradients are present, and significant production and dissipation of turbulence occurs. This layer consists of three sub-layers (ref. [17]).

The viscous sub-layer makes up the region where $y^+ < 5$. Here, viscous effects are important, and they greatly surpass the Reynold stress effects. The linear law of the wall applies: $u^+ = y^+$ (ref. [17]).
The second part of the wall layer is formed by the buffer layer. This is a transition layer in which the viscous effects become progressively less important. The peak production of turbulent kinetic energy occurs here, at $y^+ = 12$.
The final sub-layer is the logarithmic layer. It stretches over a range of y^+-values from 30 to 400, and is in fact an overlap between the wall layer and the outer layer. In this region, the logarithmic layer of the wall applies: $u^+ = \frac{1}{K}\ln(y^+) + B$ where K and B are approximately constant, taken as $K = 0.41$ and $B = 5.25$ (ref. [3]).
The outer layer forms the final 80 to 90 % of the boundary layer. Here, an exchange of fluid between the boundary layer and the free stream occurs.

The law of the wall

$$\begin{cases} u^+ = y^+, & y^+ < 5 \\ u^+ = \frac{1}{K} ln(y^+) + B, & y \in]30, 400[\end{cases}, \tag{1.4}$$

depicted in Figure 1.2, is only valid for flows over a flat plate. Since external flow over cylinders is the subject of the study here, the law won't apply to the obtained results. However, it is still approximately valid for cylinders with large diameters, as the curvature of the surface is very small there. For cylinders with smaller diameters, the surface curvature has a profound effect, lowering the dimensionless velocity in the logarithmic and outer layers (ref. [4]).

1.2.3 Turbulence - Energy cascade

In a turbulent flow, eddies of different sizes or length scales are present, with their dynamics depending on their sizes. They are divided into three categories according to their length-scales: the integral, inertial and Kolmogorov ranges. These ranges participate in an energy cascade: turbulent kinetic energy is produced at the largest scales and transferred to smaller and smaller ones, until it is dissipated at the smallest scales (ref. [17]).

The integral range comprises the largest eddies. The production of turbulent kinetic energy requires high levels of anisotropy in the flow, present at the largest scales as they are most affected by the boundary conditions. They are responsible for the main part of the turbulent kinetic energy production. Their length- and velocity-scales - l_0 and u_0 - are of the same magnitude as those of the mean turbulent flow. The Reynolds number

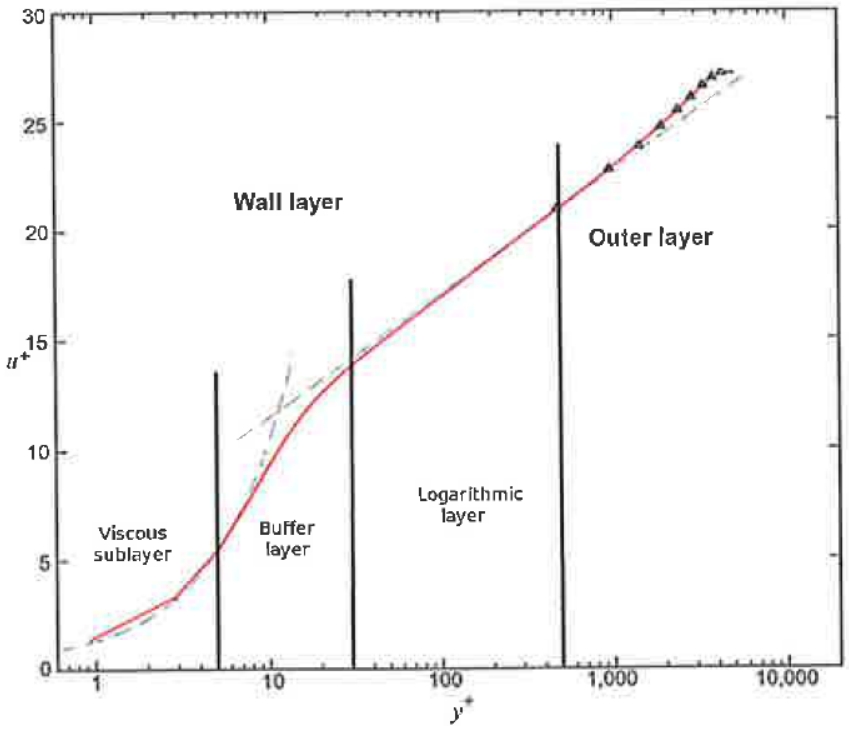

Figure 1.2: the law of the wall for a flat plate (ref.[16]).

corresponding to these eddies is much larger than unity.

$$Re_{l_0} = \frac{l_0 u_0}{\nu} \approx \frac{LU}{\nu} \gg 1 \tag{1.5}$$

The viscous forces are negligible compared to the inertial ones, and there is no dissipation of turbulent kinetic energy. As these scales are unable to dissipate the energy, it is transferred to smaller scales (ref. [17]).

The Kolmogorov hypothesis of local isotropy states that the memory of the boundary layer, responsible for anisotropy, is quickly lost as turbulent kinetic energy is transferred to smaller scales. The inertial range, and especially the Kolmogorov range, are considered more and more isotropic and do not produce turbulent kinetic energy anymore, as it requires anisotropy (Kolmogorov, 1941).

The inertial range includes eddies with sufficiently large length- and velocity-scales to assure a Reynolds number well above unity, preventing turbulent kinetic energy dissipation. Turbulent kinetic energy production is also impossible, regarding the low level of anisotropy at these scales. In this range, energy is only transferred to smaller scales (ref. [17]).

Once the turbulent kinetic energy is transferred to the eddies in the Kolmogorov range, dissipation starts. These scales are small and their velocity is low, causing the Reynolds number to drop below unity and the viscous forces to become more important than the inertial ones. These viscous forces dissipate the kinetic energy of the smallest eddies.

To properly illustrate the amount of turbulent kinetic energy at different length-scales, Figure 1.3 shows the energy spectrum. The Kolmogorov similarity hypothesis postulates a universal form of the statistics in the inertial and Kolmogorov ranges, defining them uniquely by the kinematic viscosity ν and the dissipation rate ϵ, and proposes following analytical form of the energy spectrum (Kolmogorov, 1941).

$$E(\kappa) = C_K \epsilon^{\frac{2}{3}} \kappa^{-\frac{5}{3}} \tag{1.6}$$

Here, C_K is the Kolmogorov constant and κ is the wave number, which is inversely proportional to the length scale.

1.2.4 Vortex street

A peculiarity with axial flow over rod bundles, is the high mixing intensity, even at low Reynolds numbers. This intense mixing is aided by large-scale quasi periodic vortices transporting mass, momentum and energy between adjacent subchannels connected by the gaps separating the rods. In nuclear terminology, the free-flow section in between cylinder groups is often called a subchannel. These subchannels are connected through gaps in between adjacent cylinders. The intense mixing at low Reynolds numbers, implying low pressure losses, is important for heat transfer applications.
Although, historically, there has been some discussion about the nature of these vortices (ref. [13]), in the current view, an instability resembling a Kelvin-Helmholtz instability is held responsible for this phenomenon.

A Kelvin-Helmholtz like instability is formed in the mixing layer between the high velocity subchannel flow and the lower velocity flow in the gap region, where the vicinity of the cylinder walls slows down the flow. Differences in axial velocity allow the formation of large scale eddies, and the connection of different subchannels through a gap allows the eddies to stabilize and exist in both adjacent subchannels. Hence a vortex street appears, with alternating eddies rotating in opposite senses in adjacent subchannels. This also explains the correlation between the vortices in different subchannels.

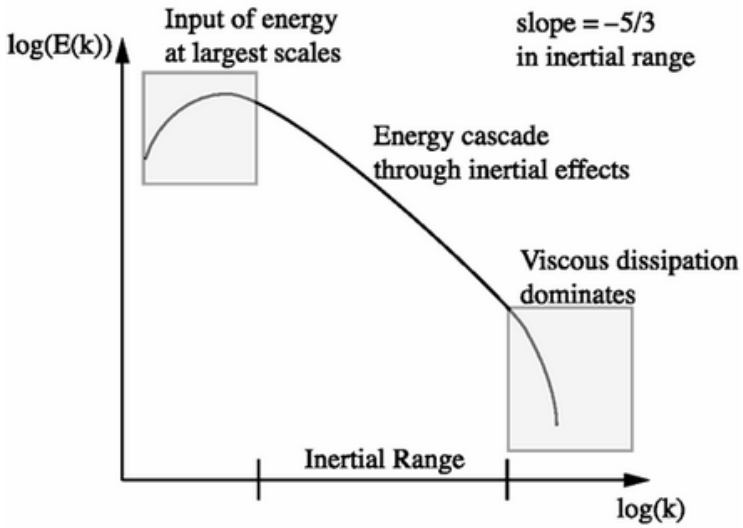

Figure 1.3: The turbulent kinetic energy spectrum (ref. [2]).

Möller (ref. [14]) devised an experimental relation for the Strouhal number, the dimensionless frequency based on the local shear velocity,

$$St_{\tau}^{-1} = \left(\frac{fD}{u_{\tau}}\right)^{-1} = 0.808\frac{P-D}{D} + 0.056 \ , \tag{1.7}$$

with f the fluctuation frequency.
In later work, Guellouz and Tavoularis (ref. [9]) found an experimental correlation for the convection speed U_c of the vortex street and the spacing λ between consecutive vortices.

$$\begin{aligned} U_c &= 1.04U\left(1 - exp\left(-10.9\tfrac{P}{D} + 10.6\right)\right) \\ \lambda &= 18.7(P-D) + 2.4D \end{aligned} \tag{1.8}$$

1.3 Frequency spectra

As already introduced in Section 1.1, a spectral analysis of the pressure distribution, spatial and temporal, on the cylinder surface, is the final goal of this thesis. The frequency spectra of interest are the power spectral density (PSD), cross-spectral density (CSD), and coherence, which is derived from the PSD and CSD. In the definition of these spectra, Fourier-transformed variables appear. Hence, a first subsection is devoted to the discrete Fourier transform (DFT).

Frequency spectra visualize the distribution of frequencies present in a time signal in a frequency-amplitude diagram. It is a convenient way of calculating the power distribution

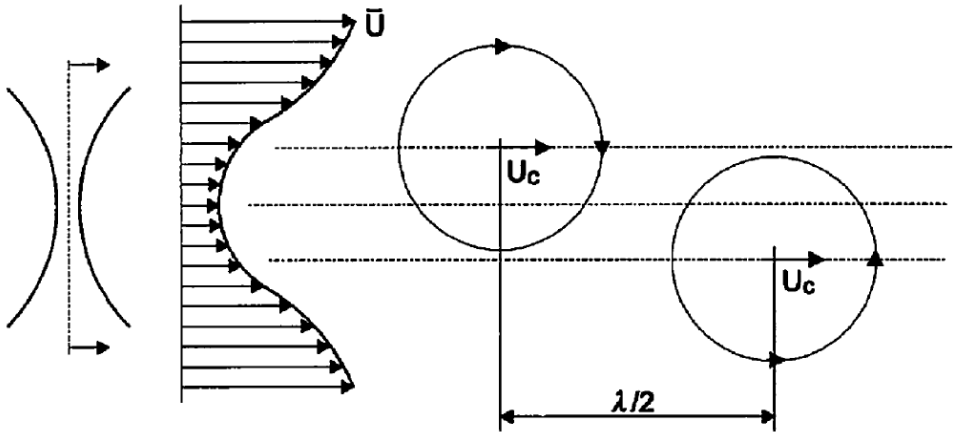

Figure 1.4: An alternating vortex street in adjacent subchannels (ref. [13]).

of an electrical signal (ref. [10]) or a random time signal in general (ref.[11]), over the frequencies present in the signal.

1.3.1 Discrete Fourier Transform (DFT)

The Fourier transform decomposes a time signal in its frequency components. If this time signal is a discrete series, a discrete Fourier transform (DFT) is used. A scalar time series x measured at N different time steps is Fourier-transformed into a complex signal X as (ref. [10])

$$X_m = \sum_{k=0}^{N-1} x(k) exp\left(-j2\pi \frac{mk}{N}\right) \ , \ m = 0, ..., N-1 \ , \tag{1.9}$$

with $j = \sqrt{-1}$ the imaginary unit.
For real time series x, $X_{N-m} = X_m^*$, $m = 0, ..N-1$ is valid, with X^* the complex conjugate of X. Therefore, only half of the spectrum needs to be computed. This half of the spectrum is referred to as the one-sided Fourier function.
From the Nyquist theorem (ref. [10]), the maximal useful frequency equals the Nyquist frequency $f_{Ny} = \frac{f_s}{2}$, with f_s the sampling frequency. The frequency resolution, or the number of data points per frequency interval, equals $f_{res} = \frac{f_s}{N}$. To investigate high frequency signals, the sampling frequency should be high, while for a high frequency resolution and to investigate low frequency signals, a high number of sampling points is important.

1.3.2 Power Spectral Density (PSD)

A PSD function is defined as an overlapped segmented averaging of modified periodograms (ref. [10]). A periodogram is a DFT of one segment of the time series, modified refers to the application of a time-domain window function, and averaging reduces the variance of spectral estimates. The PSD function statistically auto-correlates the Fourier transforms of a time series evaluated at a given point. It is defined as (ref. [10])

$$PSD_{\vec{x_1}\vec{x_1}}(St) = 2\left(X_{\vec{x_1}}(St)X^*_{\vec{x_1}}(St)\right)\frac{f_s}{N} \ . \tag{1.10}$$

The Strouhal number in above definition represents a dimensionless frequency and is defined in fluid dynamics as $St = \frac{fD_h}{U}$. The factor two originates from the one-sided Fourier transform, whereas the factor $\frac{f_s}{N}$ corrects the amplitude of the spectrum for the number of sample points. Indeed, the spectrum amplitude becomes independent of the number of time steps.

Comparison of different PSD functions is facilitated when the spectra are dimensionless. In fluid mechanics, PSD functions of pressure variables are made dimensionless as

$$\frac{PSD}{\rho^2 U^3 D_h} \ . \tag{1.11}$$

As incompressible fluids are used in the simulations, and for a dimensionless analysis, the density has no further influence on the simulations or post-processing results, ρ is chosen unity.

1.3.3 Cross-Spectral Density (CSD)

The cross-spectral density function visualizes the correlation of a time signal at two points in space per frequency band in a frequency-amplitude diagram. It is the cross-correlation of the Fourier transform of a time series evaluated at two points in space. Note that a PSD function is a special case of a CSD function, where the two points in space are identical. The CSD-function is defined as (ref. [7])

$$CSD_{\vec{x_1}\vec{x_2}}(St) = 2\left(X_{\vec{x_1}}(St)X^*_{\vec{x_2}}(St)\right)\frac{f_s}{N} \ , \tag{1.12}$$

and is a complex function, as opposed to the real PSD function.

CSD functions are made dimensionless similar to the way PSD functions are made dimensionless, and for the same reasons.

$$\frac{CSD}{\rho^2 U^3 D_h} \tag{1.13}$$

1.3.4 Coherence

By comparison of spectra of different time series, the differences in signal amplitude are easily extracted. It is however more challenging to extract the differences in the correlation of the signals between different points, as the CSD amplitudes are heavily influenced by the signal amplitude. To filter out this signal amplitude influence, a dimensionless CSD spectrum is proposed. The coherence normalizes the CSD spectrum by the PSD spectra in both correlated points. As the PSD is based on an auto-correlation function, and the CSD on a cross-correlation function, the PSD amplitude in a point is an upper limit to the CSD amplitude. The resulting spectrum is named the coherence and is defined as (ref. [1])

$$\gamma_{\vec{x_1}\vec{x_2}}(St) = \frac{CSD_{\vec{x_1}\vec{x_2}}(St)}{\sqrt{PSD_{\vec{x_1}\vec{x_1}}(St) PSD_{\vec{x_2}\vec{x_2}}(St)}} \ . \tag{1.14}$$

The coherence allows comparison of the cross-correlation between points over different time series: their coherence functions are represented on the same scale.

Chapter 2

Methodology

To study the flow over the cylinder arrays, computational fluid dynamics (CFD) simulations are performed, using the open source software OpenFOAM. In this chapter, the methodology employed in these simulations and in the post-processing are explained in depth.

The chapter starts with a discussion about the choice of flow domain and mesh. The boundary and initial conditions are treated hereafter.
An introduction to LES, a simulation method in which the large scale eddies are resolved while the small scale ones are modelled, is given next. The filter function and its characteristics are described. The Smagorinski sub-grid scale model is discussed. The part about the LES ends with an introduction to dynamic models, with a focus on the Lagrangian dynamic model.
The final part of this chapter is about the generation of the spectral functions.

2.1 Flow domain

The primary goal of the thesis is to investigate the forces exerted by a turbulent axial flow on an array of cylinders. The most widely used type of cylinder arrays in nuclear reactors, are those with square and triangular configurations (ref. [13]), which are studied here. The major parameters of these arrays are the cylinder diameter D, the cylinder pitch P (the distance between the centerpoints of adjacent cylinders), and the cylinder length L orthogonal to the plane (Fig. 2.1). As in this thesis, only the forces induced by turbulence are investigated, excluding the inlet and outlet effects at the cylinder edges, an infinitely

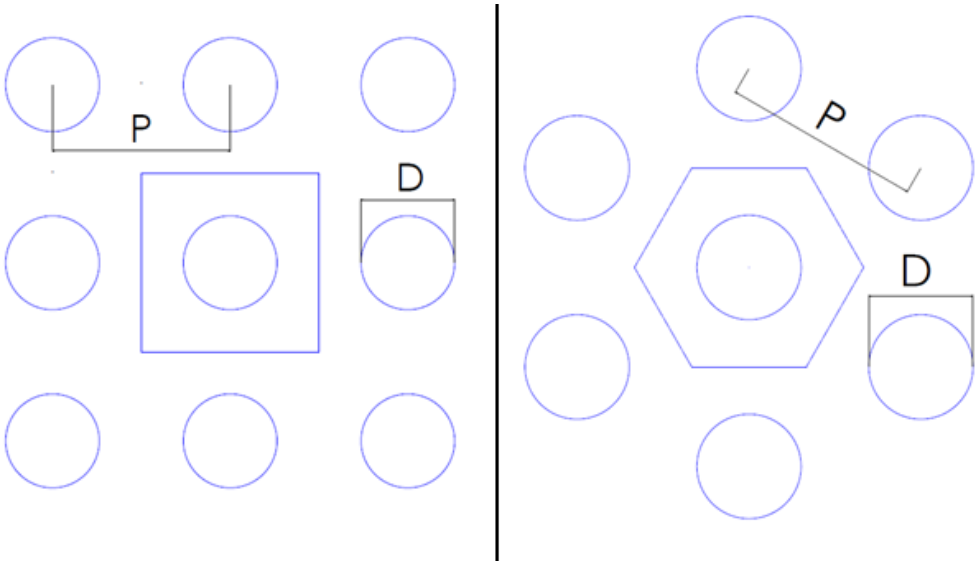

Figure 2.1: Top view of a square (left) and triangular (right) array configuration. The flow domain boundaries are given in solid line.

long cylinder is simulated.

In a first approach, one cylinder is taken representative for an entire array. A flow domain containing one cylinder is significantly smaller than one containing an entire array. Hence the grid is smaller and the computational load is strongly reduced.
A polygonal flow domain with a cylinder cut out is considered (Fig. 2.1). The edges of the polygons are the mid-lines between two adjacent cylinders. In contrast to the cross section of the flow domain, which is fixed by the array configuration and cylinder pitch, the length can be chosen freely. However, it should be long enough to allow large scale structures to be generated, otherwise they will not appear. Large scale structures break down over time into smaller ones and are the main source of turbulent eddies. Their absence will severely influence the solution and will reduce the amplitude of the spectra over the entire frequency range. The length scales of the large structures are comparable to the hydraulic diameter of the array (ref. [16]). As such, a length-over-hydraulic diameter ratio $\frac{L}{D_h}$ of 15 is chosen. In the following chapter (sec. 3.2) a simulation with a larger $\frac{L}{D_h}$-ratio is performed to check the length-convergence of the flow domain.
The chosen computational flow domain envelops one cylinder of an array. To investigate the influence of this choice of flow domain on the solution, a study checking the representativity of this flow domain for an entire cylinder array should be performed by comparing the solutions on flow domains containing n^2 cylinders (for square arrays), with n an integer.

For higher n, the influence of the boundary layers on the central subchannel or cylinder decreases. This should validate if the realistic coupling between adjacent subchannels is present. However, due to the large grid sizes, and high computational loads, accompanying flow domains enveloping multiple cylinders, this study was not yet finished by the thesis due date. Hence, the representativity of the flow domain remains but an assumption as it was not proven.

2.2 Mesh

By subdividing the flow domain in quadrilateral building blocks and meshing the edges, a high-quality prismatic mesh is generated. An example of a mesh for a quadrilateral building block of a square array flow domain is given on the left-hand side of Figure 2.2. The building block is meshed in the tangential direction along the yellow edges, in the radial direction along the green edges, and in the longitudinal direction along the red edges. Afterwards, the interior is subdivided in rectangular prismatic cells. The quadrilateral elements of the hexagonal flow domain are meshed in a similar manner. The building blocks are assembled to a full flow domain. The resulting mesh for a square array flow domain is shown on the right-hand side of Figure 2.2. For visualisation purposes, a very coarse mesh is shown, with a mesh size on the order of 10^3 cells. The meshes used in the simulations have mesh sizes 3 orders of magnitude larger.

The LES model resolves the large scale structures and models the smaller scales. To resolve these large scale structures, the simulation has to be able to follow them. This is only possible with a sufficiently fine grid: the vortices have to span multiple grid cells to be visible. Eddies smaller than the cells, so-called sub-grid scales (SGS), are modelled.

Boundary layer cell widths are made dimensionless in the same way as the dimensionless distance to the wall (sec. 1.2.2), thus

$$\Delta x^+ = \frac{\Delta x}{l_s} \text{ , } \Delta y^+ = \frac{\Delta y}{l_s} \text{ and } \Delta z^+ = \frac{\Delta z}{l_s} \text{ .} \tag{2.1}$$

The characteristic length scale l_s is derived from equation 1.2, and the wall shear stress arises from a momentum balance in the longitudinal direction. The wall shear force F_{shear} is equal to the pressure difference Δp along the cylinder, multiplied by the flow-through area A.

$$F_{shear} = \tau_w \cdot A_{cylinder} = \Delta p \cdot A \Leftrightarrow \tau_w = \Delta p \frac{A}{A_{cylinder}} = \Delta p \frac{A}{\pi D L} \tag{2.2}$$

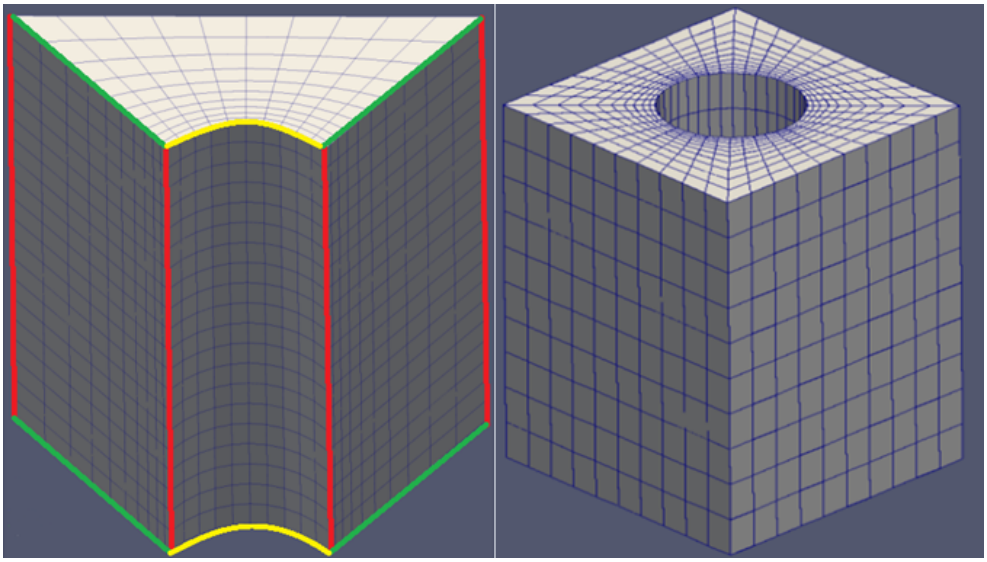

Figure 2.2: Mesh of a quadrilateral building block (left), and a full flow domain (right).

$A_{cylinder}$ represents the circumferential cylinder surface area. The flow-through area A differs for square and triangular array configurations. For a square array it equals

$$A = P^2 - \frac{\pi}{4}D^2 \Rightarrow \tau_w = \Delta p \frac{P^2 - \frac{\pi}{4}D^2}{\pi DL} \ , \tag{2.3}$$

and for a triangular array

$$A = 6\frac{1}{2}\frac{P}{2}\frac{P}{2cos(\frac{\pi}{6})} - \frac{\pi}{4}D^2 = \frac{1}{4}\left(2\sqrt{3}P^2 - \pi D^2\right) \Rightarrow \tau_w = \Delta p \frac{2\sqrt{3}P^2 - \pi D^2}{4\pi DL} \ . \tag{2.4}$$

Because the pressure gradient over the cylinder length is not known a priori, a precursor flow simulation on a coarse grid is run. The resulting pressure drop over the flow domain gives an indication of the magnitude of the pressure drop in the actual simulation.

The radial dimensionless cell width normal to the solid boundary - Δy^+ - should be smaller than two: for a LES-simulation y^+ should be smaller than unity (ref. [20]), since no sub-grid scale model with enhanced wall treatment is used. This sizing only applies to the cells closest to the solid boundary: as eddies further away from the boundary are larger in size, larger cell sizes are allowed there (ref. [16]). To reduce the grid size, grading in the radial direction is recommended. The cell-to-cell expansion factor n should be limited, here to 1.02, to avoid loss of information between large and small cells (ref. [20]). Along with the starting cell width Δy_1 and the edge length L_y, the number of cells N_y and the bias factor

B_y, or ratio between end and start cell widths, are determined (ref. [19]).

$$\begin{aligned}
&\Delta y_i = n^{i-1}\Delta y_1 \ , \ i = 1, \cdots, N_y \\
&L_y = \textstyle\sum_{i=1}^{i=N_y} \Delta y_i = \Delta y_1 \sum_{i=1}^{i=N_y} n^{i-1} = \Delta y_1 \frac{n^{N_y}-1}{n-1} \\
&\Rightarrow N_y = \text{round}\left[\frac{\ln\left(\frac{n-1}{\Delta y_1}L_y+1\right)}{\ln(n)}\right] \\
&B_y = \frac{\Delta y_{N_y}}{\Delta y_1} = \frac{n^{N_y-1}\Delta y_1}{\Delta y_1} = n^{N_y-1}
\end{aligned} \tag{2.5}$$

Cell widths in the direction of the flow - x - or in the circumferential direction - z - are subjected to less severe conditions. Δx^+ and Δz^+-values of 100 and 20 respectively can be used for the inner boundary layer (ref. [16]), although a convergence study of the grid is advised, which is performed in section 3.1. In the x- and z-directions, the mesh is not graded, since the dynamics are dominated by quasi-streamwise vortices with dimensions constant in wall-units (ref. [16]).

The dimensional grid size is based on the chosen dimensionless cell width sizes and equations 2.1, and 2.3 or 2.4.

2.3 Initial and boundary conditions

For turbulent flow problems, the initial and boundary conditions have a profound influence on the final solution (sec. 1.2.1). A careful choice of these conditions increases the accuracy and real-world representativity of the simulations.

2.3.1 Initial conditions

The amount, location and size of the turbulent scales is very dependent on geometry and flow parameters. Not all these parameters are known a priori. The generation of an accurate physical turbulent velocity field is impractical due to its complexity.
A more practical solution is the generation of a random non-physical initial velocity field. After some time, the randomness is dissipated and replaced by physical structures.

The initial velocity field is constructed by a random generator: superposed on a uniform axial velocity field is a random perturbation. This perturbation amounts up to a maximum of 10% of the axial velocity magnitude in any direction. It assists the transition to a

turbulent regime and allows for fast vortex generation. Although most of the randomness is dissipated very quickly (Fig. 2.3), the remainder ensures fast transition. The other initial fields are taken uniform throughout the flow domain, but their values are quickly forgotten by the flow.

The advantages of such an initialisation are its ease of implementation and the homogeneousness of the parameters throughout the flow domain. A disadvantage is that the initial fields are not coupled and some adaptation time is needed.
As turbulent motions are correlated (ref. [16]) and the initial velocity field is random, some development time is needed to allow the turbulent vortices to become physical. After this development time, data acquisition starts. For accuracy reasons, no data acquisition starts before the flow has travelled 140 hydraulic diameters.

2.3.2 Boundary conditions

First, a categorisation of flow domain end planes is made. An isometric view of a square array flow domain is shown in Figure 2.4. The grey cylindrical surface in the middle is referred to as the cylinder wall, the green and blue planes parallel to the cylinder axis are the side planes, the red plane on top is the outlet plane, and a similar plane at the bottom the inlet plane (not shown on the figure).

The cylinder is modelled as a wall with a smooth surface. For the velocity, a no-slip condition is imposed, which means that the velocity equals zero on the entire surface. For all other flow parameters - the pressure, SGS viscosity and the Lagrangian dynamic model parameters (explained further in section 2.4.3)- a zero-gradient condition is imposed: the change of the parameter with the distance from the cylinder surface becomes zero at the cylinder surface.

Periodic boundary conditions for all flow parameters are imposed pairwise between side planes at opposite sides of the flow domain, and between the inflow and outflow planes. These conditions between two faces are a convenient way of repeating a computational domain an infinite number of times along a direction of homogeneity. The two faces are connected in terms of flow path, while they are separated in space: flow going out of the flow domain along one plane flows in again across the other one and vice versa. The main advantage is the efficient reduction of computational domain, which strongly reduces computation time. However, the domain has to remain at least twice as large as the length

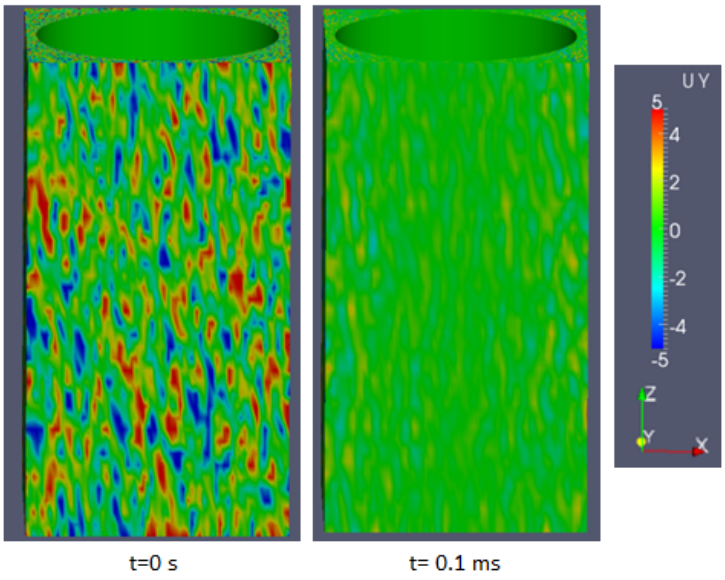

Figure 2.3: Velocity fluctuations in the flow domain at two time instants, illustrating the fast dissipation of randomness.

scales of the longest structures in the flow, otherwise these structures will not appear in the flow and the solution will be less accurate (sec. 2.1).

The use of periodic boundary conditions on side planes at opposite sides of the flow domain simulates the continuity of the array of cylinders. However, some implicit assumptions are made. The flow in all domain building blocks in the array is assumed to be identical. In addition to this, it is impossible to observe certain modes: those in which a symmetrical motion of the fluid is present, would imply in- or outflow along both opposite side planes.

As periodic boundary conditions between the inflow and outflow planes would eliminate the driving force, a virtually added axial pressure gradient is implemented in the solver. The fluid leaving the flow domain along the outflow plane flows back in across the inflow plane. This simulates an infinite cylinder length and filters out the entrance effects. Again, some implicit assumption are made: the flow is identical when translated over the length of the flow domain in longitudinal direction. An important consequence is that the wavelength of the largest structure in the flow is limited to half the length of the flow domain. This is the reason why the $\frac{L}{D_h}$-ratio of the flow domain is taken at such a large value (sec. 2.1).

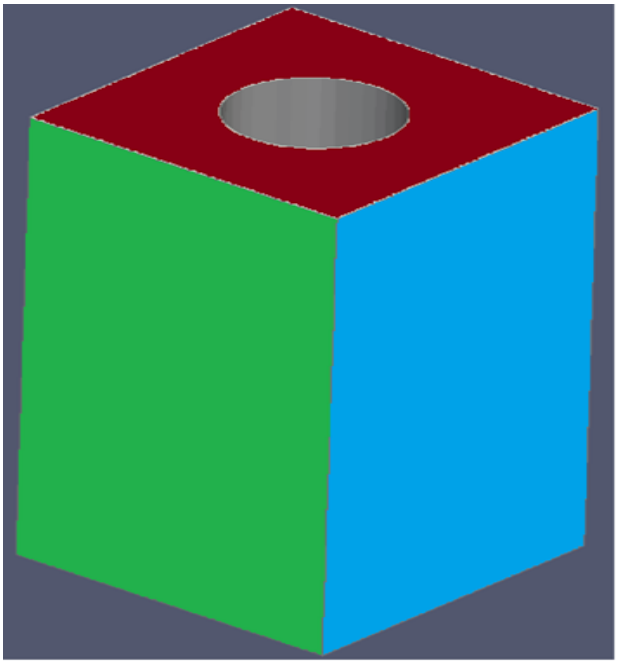

Figure 2.4: An isometric view of a square array flow domain. In grey the cylinder, red the outflow plane, and green and blue the side planes.

2.4 Large-Eddy Simulation model

The LES-model is a numerical method for (turbulent) flow simulations. It resolves the large-scale turbulent eddies while modelling the smaller scales. Justification for the modelling of the smaller scales is found in the Kolmogorov hypothesis of local isotropy (sec. 1.2.3): the small scales are more homogeneous and isotropic, and less affected by boundary conditions. Models describing these scales are more broadly applicable with less adjustments. They exploit the similarity of the small scales in the inertial and Kolmogorov ranges, and them being solely defined by the kinematic viscosity and the dissipation rate (sec. 1.2.3). The models use the residual stresses to accurately reproduce the energy transfer in a statistical sense.

Many things in this section have been extracted from U. Piomelli, 2012 (ref. [16]). The section about the Lagrangian dynamic model has been entirely taken over from C. Meneveau et. al. , 1995 (ref. [12]). No further referrals to these works will be made.

2.4.1 Filter

Filtered Navier-Stokes equations

The flow in or over an arbitrary geometry is governed by the Navier-Stokes equations. For a viscous incompressible Newtonian fluid with constant fluid properties, in the absence of body forces and heat transfer, they are given by

$$\begin{array}{ll} \text{conservation of mass} & \frac{\partial u_j}{\partial x_j} = 0 \\ \text{conservation of momentum} & \frac{\partial u_i}{\partial t} + \frac{\partial}{\partial x_j}(u_i u_j) = -\frac{1}{\rho}\frac{\partial p}{\partial x_i} + \nu \frac{\partial^2 u_i}{\partial x_i^2} \ , \end{array} \tag{2.6}$$

with u the velocity, ρ the density, p the pressure and ν the kinematic viscosity. In all of the above, Einstein's summation applies over repeated indices. The conservation of energy is omitted because the flow properties are independent of temperature, and heat transfer is not addressed here.

In a LES, the Navier-Stokes equations are filtered: filtered variables are used in the equations. A filtered variable is denoted by an overhead bar and defined as

$$\overline{f}(x) = \int_D f(x') G\left(x, x', \overline{\Delta}\right) dx' \ , \tag{2.7}$$

with D the flow domain, G the filtering function, and $\overline{\Delta}$ the filter width.
The goal of this filtering operation is to reduce the importance of smaller scale motions: instead of resolving these motions, they will be modelled and appear in the filtered Navier-Stokes equations as residual terms.
By applying this filter to equation 2.6, one obtains

$$\begin{array}{ll} \text{conservation of mass} & \frac{\partial \overline{u_j}}{\partial x_j} = 0 \\ \text{conservation of momentum} & \frac{\partial \overline{u_i}}{\partial t} + \frac{\partial}{\partial x_j}(\bar{u}_i \bar{u}_j) = -\frac{1}{\rho}\frac{\partial \overline{p}}{\partial x_i} - \frac{\partial \tau_{ij}}{\partial x_j} + \nu \frac{\partial^2 \overline{u_i}}{\partial x_i \partial x_j} \ . \end{array} \tag{2.8}$$

The Navier-Stokes equations govern the evolution of the large-scale motions. The effect of the small-scale motions on the large ones appears through a residual stress term $\tau_{ij} = \overline{u_i u_j} - \bar{u}_i \bar{u}_j$, also referred to as the SGS stress.

Filter width

The filter width $\overline{\Delta}$ is related to the smallest scales of motion that are still resolved and is usually chosen proportional to the grid size h: $\overline{\Delta} = n \cdot h$, with n a constant. For anisotropic

grids, h can be chosen an algebraic average: $h = (h_x h_y h_z)^{1/3}$.
Relating the filter width and the grid size is a convenient choice, as they both limit the smallest scales of motion that are still resolved (sec. 2.2). With this choice, a reduction in grid size induces a reduction in filter width, ensuring the LES approaching a DNS simulation (Direct Navier Stokes simulation, a simulation technique that resolves all scales) for a reducing grid size.

Filter function

The filter function defines the weight assigned to the structures in the transition region between scales larger and scales smaller than the filter width. A multitude of filters exist, but only the simple tophat-filter is discussed here. It is defined (in real space) as

$$G(x) = \begin{cases} \frac{1}{\overline{\Delta}} & |x| \leq \frac{1}{2}\overline{\Delta} \\ 0 & otherwise \end{cases} , \tag{2.9}$$

and depicted in Figure 2.5. Its simplicity and capability to smooth out small scale fluctuations makes it a filter of choice.

2.4.2 Sub-grid scale models

The goal of a subgrid scale model is to represent energy transfer between resolved and unresolved scales. Two energy equations, one for the resolved and one for the unresolved scales, represent the energy transfer with the other scales and with the surroundings. The transport equation for $\overline{q}^2 = \bar{u}_i \bar{u}_j$, twice the total resolved energy, becomes

$$\begin{aligned} \frac{\partial \overline{q}^2}{\partial t} + \underbrace{\frac{\partial}{\partial x_j}\left(\bar{q}^2 \bar{u}_j\right)}_{\text{advection}} = \; & -2 \underbrace{\frac{\partial}{\partial x_j}\left(\bar{p}\bar{u}_j\right)}_{\text{pressure diffusion}} + \underbrace{\frac{\partial}{\partial x_j}\left(\nu \frac{\partial \overline{q}^2}{\partial x_j}\right)}_{\text{viscous diffusion}} - 2 \underbrace{\frac{\partial}{\partial x_j}\left(\tau_{ij}\overline{u_i}\right)}_{\text{SGS diffusion}} \\ & -2 \underbrace{\nu \frac{\partial \overline{u_i}}{\partial x_j}\frac{\partial \overline{u_i}}{\partial x_j}}_{\text{viscous dissipation}} + 2 \underbrace{\tau_{ij}\overline{S_{ij}}}_{\text{SGS dissipation}} . \end{aligned} \tag{2.10}$$

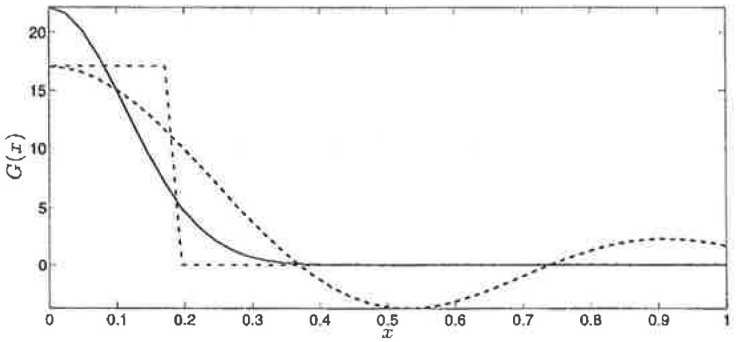

(a) Tophat filter in real space (- - -)

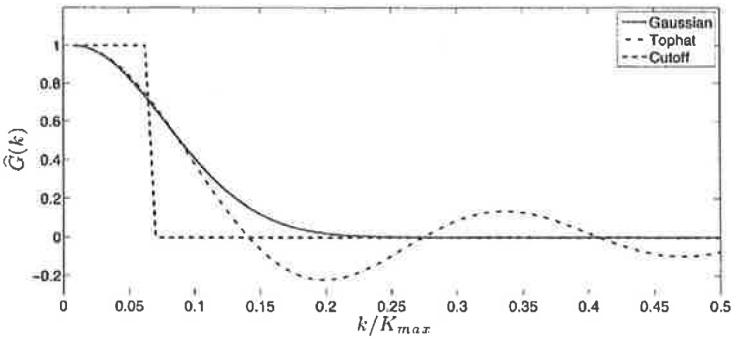

(b) Tophat filter in wave space (- - -)

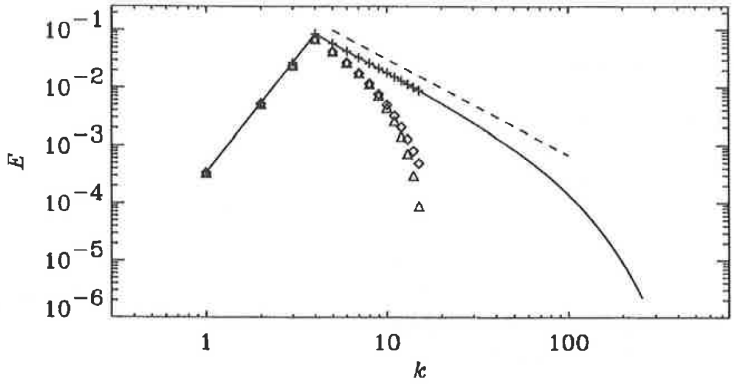

(c) Filtering of the turbulent energy spectrum by a tophat filter (△)

Figure 2.5: Visualisation of the tophat filter (ref. [16]).

The transport equation for $q_{SGS}^2 = \tau_{kk}$, twice the SGS-energy, is given by

$$\begin{aligned}\frac{\partial q_{SGS}^2}{\partial t} + \underbrace{\frac{\partial}{\partial x_j}\left(q_{SGS}^2 \overline{u_j}\right)}_{\text{advection}} = & \underbrace{-\frac{\partial}{\partial x_j}\left(\overline{u_i u_i}\,\overline{u_j} - \overline{u_i u_i u_j}\right)}_{\text{turbulent transport}} \underbrace{-2\frac{\partial}{\partial x_j}\left(\overline{p u_j} - \bar{p}\,\overline{u_j}\right)}_{\text{pressure diffusion}} + \underbrace{\frac{\partial}{\partial x_j}\left(\nu \frac{\partial q_{SGS}^2}{\partial x_j}\right)}_{\text{viscous diffusion}} \\ & \underbrace{+2\frac{\partial}{\partial x_j}\left(\tau_{ij}\overline{u_i}\right)}_{\text{SGS diffusion}} \underbrace{-2\,\nu\left(\overline{\frac{\partial u_i}{\partial x_j}\frac{\partial u_i}{\partial x_j}} - \frac{\partial \overline{u_i}}{\partial x_j}\frac{\partial \overline{u_i}}{\partial x_j}\right)}_{\text{viscous dissipation}} \underbrace{-2\,\tau_{ij}\overline{S_{ij}}}_{\text{SGS dissipation}} ,\end{aligned} \tag{2.11}$$

with $\bar{S_{ij}} = \frac{1}{2}\left(\frac{\partial \bar{u_i}}{\partial x_j} + \frac{\partial \bar{u_j}}{\partial x_i}\right)$ the large scale strainrate tensor.
In these equations the diffusion and advection terms are solely responsible for the redistribution of energy. The dissipation terms in the resolved energy equation appear as source terms in the unresolved one, while dissipation terms in the unresolved energy equation convert kinetic energy to heat. Along with the other conservation equations, the system is closed.

Eddy viscosity models

Eddy viscosity models relate the SGS-stresses to the large scale strainrate tensor.

$$\tau_{ij} - \frac{\delta_{ij}}{3}\tau_{kk} = -2\nu_T\overline{S_{ij}} \tag{2.12}$$

Herein, δ_{ij} is the chronecker delta. This equation needs closure for the eddy viscosity ν_T. For simplicity reasons, this eddy viscosity is often obtained algebraically to avoid solving additional equations and increasing computation time. This is justifiable due to the Kolmogorov hypothesis of local isotropy (sec 1.2.3), assuming the small unresolved scales homogeneous and isentropic, offering a certain accuracy to even simple models. Additionally, the contribution of the SGS stresses compared to the total stresses is negligible, hence the severity of modelling errors is limited.
The algebraic model postulates a linear relation between the eddy viscosity and a characteristic length and velocity scale

$$\nu_T \sim l \cdot u_{SGS} \ . \tag{2.13}$$

The length scale l is taken equal to the filter width $l = \overline{\Delta}$: the most active of the unresolved scales are closest to the cutoff length. The characteristic velocity is chosen as the square root of the trace of the SGS-stress tensor: $u_{SGS}^2 = q_{SGS}^2 = \tau_{kk}$.
To avoid solving the transport equation for q_{SGS}^2, an equilibrium assumption is made: due to the short time scales of the small scales, it is assumed that they adjust to perturbations instantaneously, hence being in a state of equilibrium at any given moment. Neglecting all derivatives in equation 2.11, the transport equation for q_{SGS}^2 simplifies to

$$\epsilon_\nu = -\tau_{ij}\overline{S_{ij}} \ , \tag{2.14}$$

with $\epsilon_\nu = \nu\left(\overline{\frac{\partial u_i}{\partial x_j}\frac{\partial u_i}{\partial x_j}} - \frac{\partial \overline{u_i}}{\partial x_j}\frac{\partial \overline{u_i}}{\partial x_j}\right)$ the viscous dissipation rate.

Smagorinski model

One widely used type of eddy viscosity model is the Smagorinski model, developed by Smagorinski in 1963. It uses the equilibrium hypothesis, along with dimensional analysis, stating $\epsilon_\nu \sim \frac{q_{SGS}^3}{l}$. Combining this equation, along with equations 2.12, 2.13, 2.14, and the equations for the characteristic length and velocity scales, one obtains $q_{SGS} \sim \overline{\Delta}|\overline{S}|$, with $|\overline{S}| = \sqrt{2\bar{S}_{ij}\bar{S}_{ij}}$ the magnitude of the strain rate tensor. The eddy viscosity becomes

$$\nu_T = \left(C_s\overline{\Delta}\right)^2 |\overline{S}| \ , \tag{2.15}$$

where the value of the Smagorinski constant C_s is either chosen a priori with static models, or calculated during the simulation with dynamic models.

2.4.3 Lagrangian dynamic model

Dynamic model

A dynamic model evaluates the model coefficients for the SGS stresses during the calculation instead of a priori. They are computed directly from the resolved turbulent field of the LES simulation by sampling the turbulent stresses for the smallest resolved scales and extrapolating them to the SGS range. To do so, the resolved turbulent stresses are calculated using the Germano identity (ref. [8]) and a test filter $\widehat{\Delta}$, usually taken twice the width of the grid filter: $\widehat{\Delta} = 2\overline{\Delta}$.

$$L_{ij} = T_{ij} - \widehat{\tau_{ij}} \tag{2.16}$$

Here, $L_{ij} = \widehat{\overline{u_i}\overline{u_j}} - \overline{\overline{u_i}\overline{u_j}}$ represents the resolved turbulent stresses (Reynoldstresses from length scales in between the grid- and testfilter width), $T_{ij} = \widehat{\overline{u_i u_j}} - \overline{\overline{u_i}\overline{u_j}}$ the subtest stresses (Reynoldstresses from length scales smaller than the testfilter width), and $\widehat{\tau_{ij}} = \widehat{\overline{u_i u_j}} - \widehat{\overline{u_i}\overline{u_j}}$ the sub-grid stresses (Reynoldstresses from length scales smaller than the gridfilter width). Both the subtest and the subgrid stresses are approximated by an eddy viscosity model, in this case a Smagorinski model.

$$\begin{aligned} \widehat{\tau_{ij}} &= -2\left(C_s\overline{\Delta}\right)^2 |\overline{S}|\overline{S_{ij}} \\ T_{ij} &= -2\left(C_s\widehat{\Delta}\right)^2 |\widehat{\overline{S}}|\widehat{\overline{S_{ij}}} = -2\left(C_s 2\overline{\Delta}\right)^2 |\widehat{\overline{S}}|\widehat{\overline{S_{ij}}} \end{aligned} \tag{2.17}$$

Due to the approximation of the subtest and sub-grid scale stresses, the Germano identity is only approximately satisfied. This, along with an overdefined system for the Smagorinski constant, results in an error

$$e_{ij} = L_{ij} - (T_{ij} - \widehat{\tau_{ij}}) = L_{ij} - 2\overline{\Delta}^2\left(\widehat{C_s^2|\overline{S}|\overline{S_{ij}}} - 4C_s^2|\widehat{\overline{S}}|\widehat{\overline{S_{ij}}}\right) \ . \tag{2.18}$$

To obtain an optimal solution, this error should be minimized. This is done in a least-square sense, by taking an ensemble average over the error. By using Lagrangian averaging, this ensemble average is taken along pathlines. This is an obvious choice, as the pathlines are the natural direction of the fluid flow and the turbulent kinetic energy cascade.

The pathline of a particle at position x at time t is given by the function z(x,t,t'), giving its position at a time t'

$$z\left(x,t,t'\right) = x - \int_{t'}^{t} \overline{u}\left(z\left(x,t,t''\right),t''\right) dt'' \ . \tag{2.19}$$

The local error at time t' according to equation 2.18 becomes

$$\begin{aligned} e_{ij}\left(z,t''\right) &= L_{ij}\left(z,t''\right) - C_s^2\left(x,t''\right) M_{ij}\left(z,t''\right) \\ M_{ij} &= 2\overline{\Delta}^2 \left(\widehat{|\overline{S}|\overline{S}_{ij}} - 4\widehat{|\overline{S}|}\widehat{\overline{S}_{ij}}\right) \ . \end{aligned} \tag{2.20}$$

C_s^2 is left out of the filtering operation, keeping in mind that it doesn't vary strongly in space over the scale of the test filter, as it is determined by averaged equations. The total error E, being the pathline accumulation of the local error squared (the ensemble average), is obtained as

$$E = \int_{-\infty}^{t} e_{ij}(z,t')e_{ij}(z,t')W(t-t')dt' \ , \tag{2.21}$$

with W(t-t') a weighing function assigning a higher importance to errors closer to time t. When this total error is minimized, an expression for $C_s(x,t)$ is obtained

$$\begin{aligned} &\tfrac{\partial E}{\partial C_s^2} = 0 \Leftrightarrow C_s^2(x,t) = \tfrac{f_{LM}(x,t)}{f_{MM}(x,t)} \\ \text{with} \begin{cases} f_{LM}(x,t) = \int_{-\infty}^{t} L_{ij}(z,t')M_{ij}(z,t')W(t-t')dt' \\ f_{MM}(x,t) = \int_{-\infty}^{t} M_{ij}(z,t')M_{ij}(z,t')W(t-t')dt' \ . \end{cases} \end{aligned} \tag{2.22}$$

The increased computational load associated with the dynamic Lagrangian model is due to the need to solve additional transport equations for f_{LM} and f_{MM}.

2.5 Frequency spectra

In this section, a somewhat deeper analysis of the calculation and meaning of the frequency spectra is performed. Throughout the thesis, wall-pressure PSD and CSD spectra are used to quantify the effect of different parameters on the magnitude and frequency of the forces on the cylinders. First, the cylinder surface coordinates are defined, and the importance of

time and space averaging on the spectra is explained. Then, the effects of the choice of flow domain and boundary conditions on the calculation and interpretation of the spectra are discussed. The section ends with the description of Curling's correlation for CSD spectra.

2.5.1 Cylinder surface coordinates

The position of a point on the cylinder surface is given by a longitudinal coordinate and a circumferential coordinate. Because of the use of periodic boundary conditions between the inlet and outlet planes, the longitudinal coordinate loses its absolute meaning: only relative differences between axial coordinates of points are of importance. The circumferential coordinate - θ - is chosen such that is equals zero in the gap region (Fig. 2.6). Thus, in the gap region, θ_{gap} is given by

$$\begin{aligned} \theta_{gap} &= k \cdot 90^\circ \ , \ k \in \mathbb{Z} \text{ for square arrays and} \\ \theta_{gap} &= k \cdot 60^\circ \ , \ k \in \mathbb{Z} \text{ for triangular arrays ,} \end{aligned} \tag{2.23}$$

and in the subchannel region $\theta_{subchannel}$ by

$$\begin{aligned} \theta_{subchannel} &= \tfrac{2k+1}{2} \cdot 90^\circ \ , \ k \in \mathbb{Z} \text{ for square arrays and} \\ \theta_{subchannel} &= \tfrac{2k+1}{2} \cdot 60^\circ \ , \ k \in \mathbb{Z} \text{ for triangular arrays .} \end{aligned} \tag{2.24}$$

2.5.2 The importance of averaging

The plotting of raw PSD and CSD data results in a significant amount of scatter. To reduce this scatter and the influence of outliers, averaging in different variables is employed.

A double averaging in space is performed: in the longitudinal and in the circumferential direction.
For the longitudinal averaging, the circumferential coordinates are fixed, while the longitudinal coordinates are free to move from the bottom of the cylinder towards the top. Taking the average of the spectra over the number of gridpoints in the longitudinal direction results in a longitudinal averaged spectrum.
Circumferential averaging exploits the symmetry of the array configuration: shifting θ over 90° in a square array or 60° in a triangular one, results in a similar situation to the one before the shift. Taking the average of the spectra over the 4 (square configuration) or 6

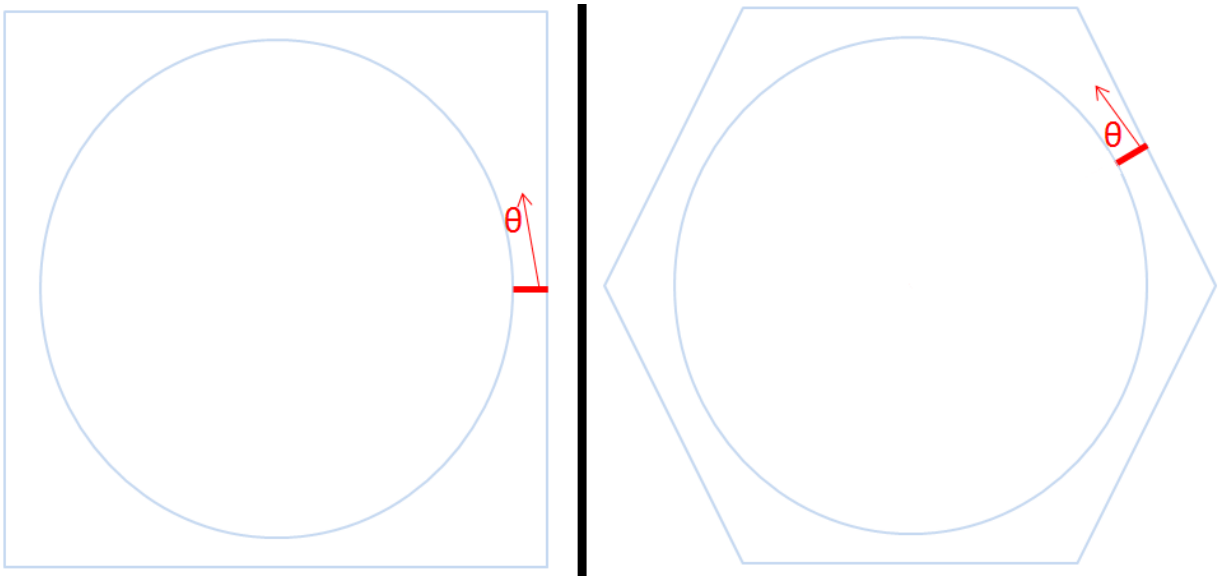

Figure 2.6: Indication of the zero reference value of the circumferential coordinate in a square (left) and triangular (right) array. $\theta = 0°$ corresponds to the gap region, and $\theta = 45°$ or $\theta = 30°$ to the subchannel region for square or triangular arrays respectively.

(triangular configuration) similar situations, gives the circumferential averaged spectrum. Averaging in space is performed in the square array as

$$CSD\left(St, \theta, \theta', \overline{x}\right) =$$
$$\frac{1}{4Nx} \sum_{m=0}^{m=N_x-1} \sum_{n=0}^{3} CSD\left(St, \theta + n\frac{\pi}{4}, \theta' + n\frac{\pi}{4}, \left(m + \frac{1}{2}\right)\frac{\Delta x}{L}, \left(\overline{x} + \left(m + \frac{1}{2}\right)\frac{\Delta x}{L}\right) mod L\right) , \tag{2.25}$$

with N_x the number of cells in the longitudinal direction, and *mod* the modulus. Similar expressions are used for the PSD and coherence spectra, and for the triangular configuration.

Averaging in time is performed by dividing the length of the time domain t over which the pressures are obtained, into n number of time batches, each with a time length $\frac{t}{n}$. The spectrum of each time batch is calculated, after which the average of the spectra is taken. A disadvantage of time-averaging is that by reducing the time length over which a spectrum is calculated, hence reducing the amount of samples, low frequency information is lost (Nyquist theorem, ref. [10]).

An example of this is shown in the figures below. Two PSD plots of square arrays are shown in Figure 2.7, one without averaging, and one with averaging in space and in time

over 10 time batches. By averaging over space and time, the scatter is significantly reduced and the influence of outliers becomes negligible.

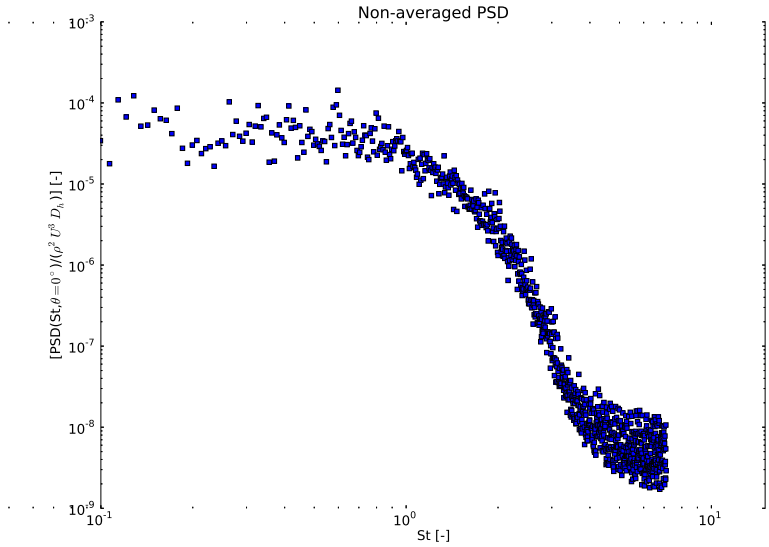

(a) PSD plot without averaging

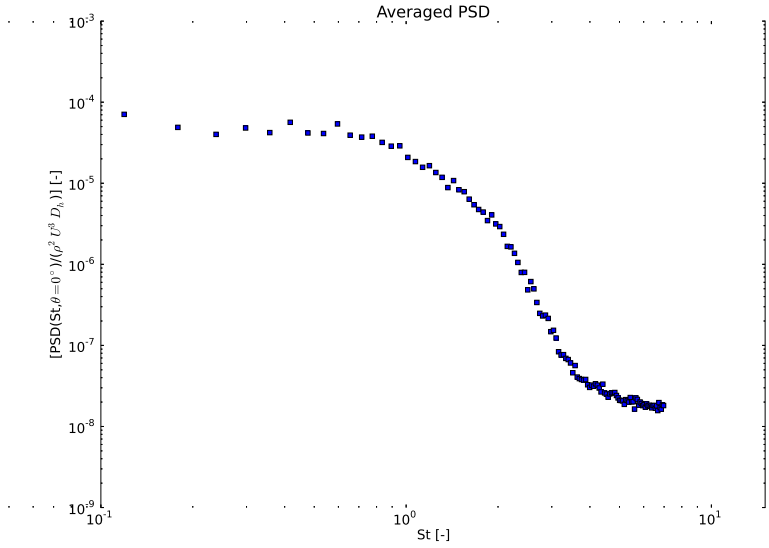

(b) PSD plot with averaging in space and in time over 10 time batches

Figure 2.7: Visualisation of the importance of averaging for spectral functions.

2.5.3 Flow domain and boundary conditions effects

The choice of flow domain and boundary conditions has a significant effect on the calculation and interpretation of the spectra, especially the CSD and coherence.

A first effect was already given in 2.5.1: because of the periodic boundary conditions between inlet and outlet plane, the limited flow domain length, and the absence of entrance effects, the absolute axial coordinate loses its meaning. Indeed, the flow at a point x_1 and a point x_2 translated axially over the flow domain length L with respect to x_1, is identical. Therefore, only relative axial coordinates, or differences in axial coordinates $\overline{x}$ have meaning. This, however, is beneficial, as it allows averaging over the axial direction (sec. 2.5.2).

A second effect of the limited flow domain length in combination with the periodic boundary conditions between inlet and outlet plane, is the limitation of the $\overline{x}$ in the CSD and coherence calculations. It is self-evident that spectra with an axial shift argument $\overline{x}$ larger than the flow domain length L, are identical to the same spectra with an axial shift argument $\overline{x}$ mod L.
However, a more stringent condition is present. Axial shifts larger than half the flow domain length are, due to the periodic boundary conditions between inlet and outlet plane, equivalent to a negative shift: $\overline{x} = (\overline{x} \bmod L) - \frac{L}{2}$. As absolute axial coordinates have no meaning, a negative shift or a positive shift over the same axial distance results in identical spectra. Thus, $\overline{x} \in [0, \frac{L}{2}]$ is representative for the entire range of axial shifts, as all $\overline{x'}$ can be reduced to $\overline{x} = |(\overline{x'} \bmod L) - \frac{L}{2}|$

While the two first effects had an influence on the calculation and limitations of the spectra, the periodic boundary conditions on the side walls of the flow domain have an influence on the interpretation of the spectra.
By looking at Figure 2.1, it might not seem like different quadrants of the flow domain are well connected. However, because of the periodic boundary conditions between opposite flow domain side planes, fluid is easily transported from one side of the flow domain to the other. It is therefore careless to assume that the cross-correlation between points in different quadrants of the cylinder equals the cross-correlation between different points on the same cylinder: these sides of the cylinder are only connected through gap regions and the flow exchangement through these gaps is negligible to the one through the flow domain boundaries. Hence, these spectra are interpreted as cross-correlations between points on different cylinders adjacent to the same subchannel. This, along with the circumferential

coordinate range for each arc, is given in Figure 2.8.

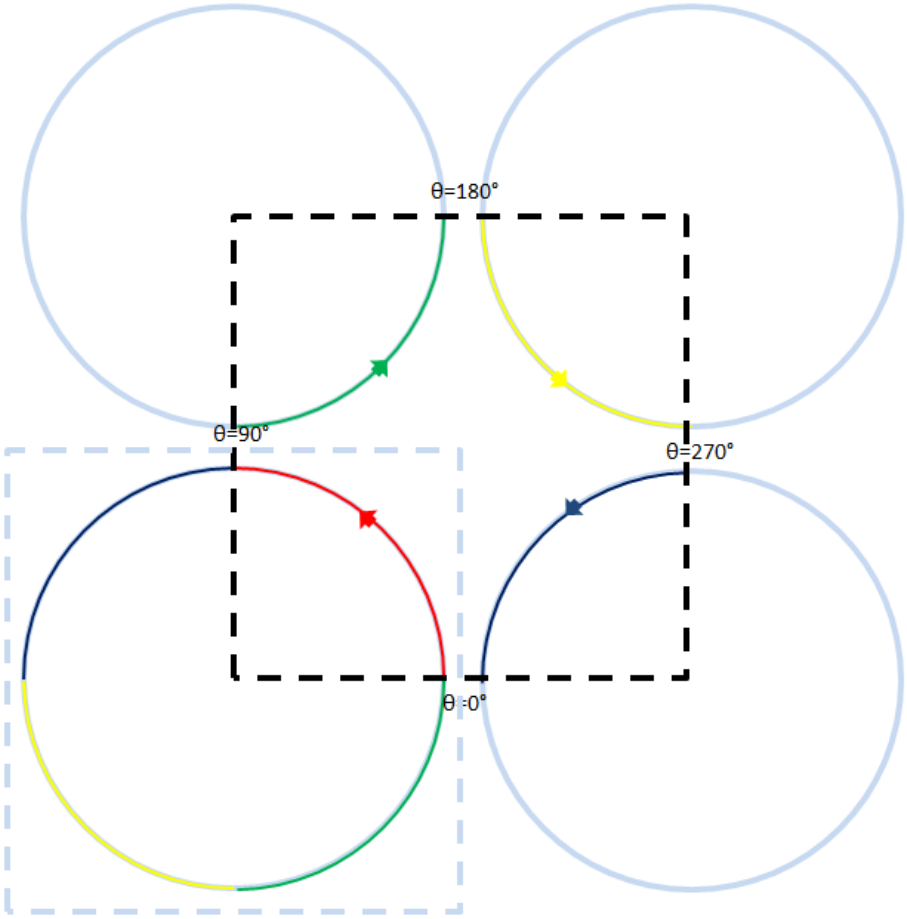

Figure 2.8: A square array configuration with the studied flow domain in blue dashed lines. A point on the flow domain cylinder in the green, yellow, or blue region is equivalent to the point on another cylinder arc of the same colour, as indicated by the evolution of θ. An equivalent flow domain is drawn in black dashed lines.

The blue flow domain is essentially transformed to an equivalent flow domain drawn in black dashed lines. On this flow domain, the same boundary conditions apply: periodic boundary conditions between inlet and outlet plane and between opposite flow domain sides, and wall conditions on the quarter-cylinder surfaces.
This approach limits the application of the spectral analysis, in a sense that cross-correlations between points adjacent to different subchannels can not be calculated, even when they are on the same cylinder.

2.5.4 Curling's correlation

Curling proposed a correlation for CSD spectra of wall-pressures between positions on the same cylinder, for square arrays subjected to an axial flow (ref. [5]). This correlation is used throughout the thesis to compare and validate the obtained results with, and is given in appendix A.
Curling's correlation is obtained experimentally with his cylinder bundle setup. In this setup, flexible cylinders are used, conflicting with the rigid cylinders simulated in this thesis. However, this should have no large influence on the wall-pressure spectra, as turbulence-induced vibrations have a one-way coupling between the flow and the structural motion (sec. 1.1). Entrance effects, however, do play an important role in the correlation, while they are filtered out in the simulations. The correlation is estimated to be valid for any Strouhal number larger than 0.25 and for any pitch and diameter combination. Although it is only validated for Strouhal numbers up to 3 and for one pitch-over-diameter ratio.
As shown in Figure 2.9, depicting the wall pressure CSD's between points at 0° and 30° for two different Reynolds numbers, there is a significant mismatch between the correlation and the data. This questions the accuracy of the correlation.
Despite these arguments against the correlation, it is used nevertheless, although only to roughly estimate the magnitude and trend of the spectra.

With regards to the discussion in the previous section (sec. 2.5.3), the comparison between the obtained spectral distributions and Curling's correlation is only valid for points in the same quadrant. For larger circumferential coordinate differences, the CSD and coherence functions of the simulation results will represent the cross-correlation between points on different cylinders adjacent to the same subchannel, while the functions for Curling's correlation will represent the cross-correlation between points on the same cylinder adjacent to different subchannels.

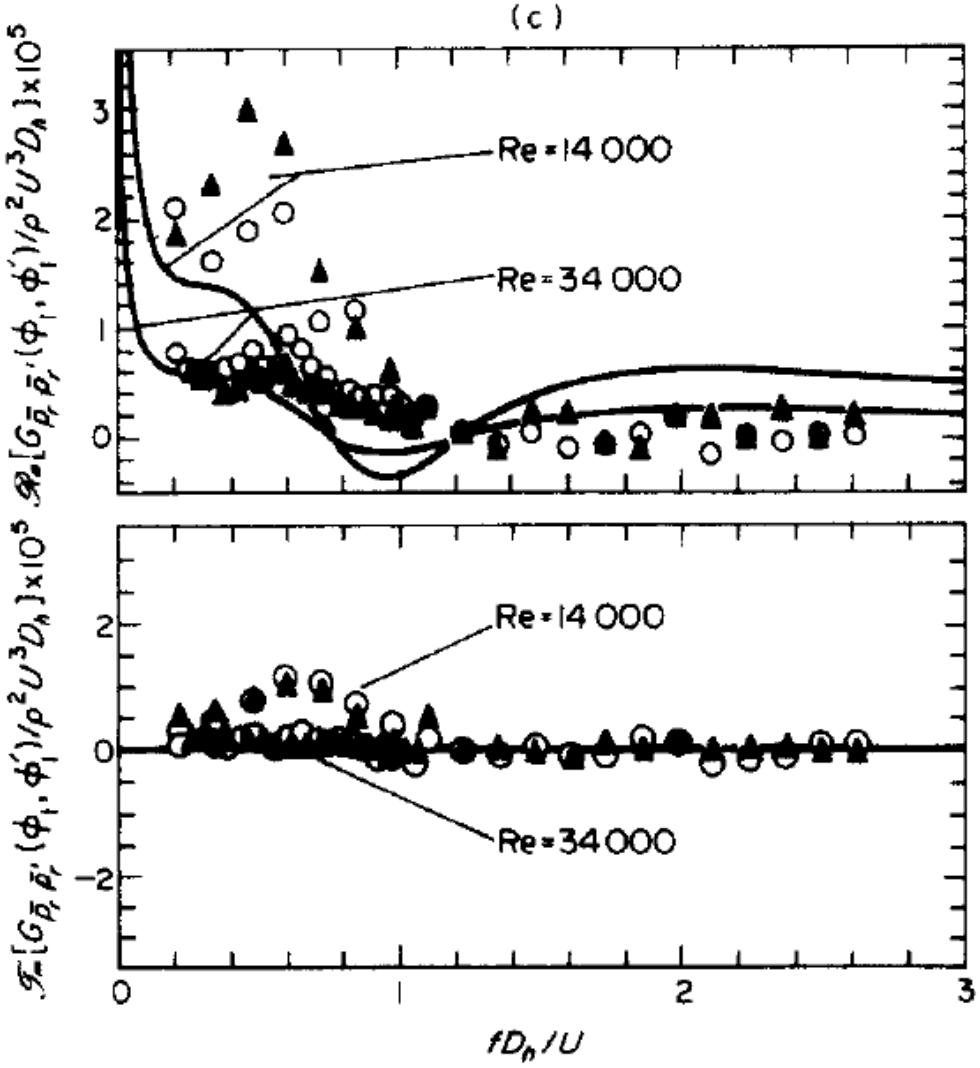

Figure 2.9: The real (top) and imaginary (bottom) parts of the wall pressure CSD·10^5 between points at 0° and 30° against the Strouhal number, according to Curling (ref. [5]). Triangles represent measurements at Re 14,000, circles measurements at Re 34,000. The correlation is drawn in solid line.

Chapter 3

Accuracy study

Before data can be interpreted, the accuracy of the calculations has to be checked. First, the convergence of the computational mesh is proven, followed by the length convergence of the flow domain.
The representativity of the one-cylinder representation of the full array is also part of the accuracy study, but as was already mentioned in section 2.1, these simulations were not yet finished by the thesis due date.

The accuracy studies are performed on only one case. Once the accuracy of this case is proven, other simulations with the same dimensionless quantities are assumed to be accurate as well. This strategy avoids performing identical accuracy calculations on subsequent simulations, and reduces the work load.
The dimensionless quantities for the grid convergence, are the dimensionless cell widths near the cylinder surface in all three directions. Simulations on grids with lower dimensionless cell widths than the converged grid, are grid independent as well.
For the flow domain length sensitivity study, the dimensionless parameter is the ratio of the flow domain length to the hydraulic diameter of the array. Simulations on flow domains with larger $\frac{L}{D_h}$-ratios than the length-converged flow domain, are flow domain length independent as well.

3.1 Grid convergence

A total grid convergence is achieved once the solution is completely independent from further grid refinement. For LES-simulations, this condition is relaxed to a solution that

no longer depends strongly on the grid size. To achieve full grid independency, the grid size is close to those required for DNS-simulations.

An initial simulation, named the reference case, has been created. Its properties are given in Table 3.1. The dimensionless wall units of the reference case are chosen $\Delta x^+ = 100$, $\Delta y^+ = 2$ and $\Delta z^+ = 20$, as discussed in Section 2.2. Once the pressure drop over the array is stable in time, the resulting dimensionless mean velocity distribution along a gap and along a subchannel is plotted against the log-law of the wall (Fig. 1.2). The mean velocity field is calculated by averaging the velocity field over 2000 time steps. This filters out the outliers and reduces the scatter. From this mean velocity field, the velocities along a gap or subchannel zone are selected. They are made dimensionless by dividing them by the previously calculated characteristic length and velocity scales (eq. 1.2).

Several identical cases with refined grids are simulated and compared to the reference case to study the grid convergence. Their dimensionless cell widths are given in Table 3.2. The dimensionless velocity distributions of these cases are plotted in Figure 3.1. As these plots do not differ much from the reference case, one builds up confidence that the grid is converged in all three directions.
The velocity distributions are drawn up to a dimensionless wall distance of 400, because the law of the wall is only valid up to this y^+-value (sec. 1.2.2). The simulation results in the gap region (Fig. 3.1(a)) however, are only given up to a y^+-value of 75. This is because the distance from the cylinder surface to the flow domain wall is small and corresponds to a maximum y^+-value of 75.
The curvature of the cylinder surface increases the dimensionless velocity in the logarithmic and outer layers, as opposed to the results obtained by Chung, Rhee and Sung (ref. [4]). A possible explanation is the annular flow geometry used in the paper. Further reasons for this disagreement have not been explored, as the main conclusion aimed for is the insensitivity of the solution to the grid size.

An additional verification of grid convergence is performed by comparing the PSD spectra of the wall pressures obtained with the different grids. In Figure 3.2, the PSD spectra in the gap region are compared to each other and to the correlation proposed by Curling (ref.

Table 3.1: The flow and geometric properties of the reference case.

Name	Configuration	D [m]	P [m]	$\frac{P}{D}$ [-]	D_h [m]	U [$\frac{m}{s}$]	ν [$\frac{m^2}{s}$]	Re_{D_h} [-]
reference case	square	0.2	0.217	1.085	0.1	140	0.001	14,000

Table 3.2: The grid properties of the cases used to check grid convergence.

Name	Δx^+ [-]	Δy^+ [-]	Δz^+ [-]	# cells
reference case	100	2	20	2,620,800
X30 case	60	2	20	4,368,000
X20 case	40	2	20	6,552,000
Y06 case	100	1.2	20	3,307,200
Z6 case	100	2	12	4,233,600

[5]).
Unlike the PSDs of the grids refined in the circumferential and radial direction, the PSDs of the grids refined in the longitudinal direction do not correspond to the PSD of the reference case. However, their disagreement is restricted to the high frequency domain (Fig. 3.2). When refining the grid in the longitudinal direction, vortices with smaller longitudinal dimensions are resolved. These smaller vortices correspond to high frequency variations and are responsible for the increased contribution of the high frequencies in the PSD spectrum. One could argue that a further refinement of the grid in the longitudinal direction is necessary to obtain accurate solutions. However, as the scope of this thesis is limited to a Strouhal number up to 1.25, the difference in the PSD spectra for the different grids is negligible. The grid size and hence the computation time can therefore be limited. As a Strouhal number of 1.25 corresponds to a high frequency (about 1.75kHz for the reference case), the practical applications of the research are in no way harmed by this limitation.
Note that the frequency ranges of the Y06 and X20 cases extend to higher Strouhal numbers. This is because the time step sizes in these simulations are smaller. As stated in section 1.3.1, smaller time step sizes generate higher frequency data.

3.2 Flow domain length-convergence

Once grid convergence is established, the convergence of the flow domain length needs to be checked. As specified by Piomelli et. al. (ref. [16]), the length of the flow domain has to be sufficiently large to allow the generation of large scale vortices. The presence or absence of these vortices is shown in the frequency spectra: they are responsible for an increase in the content over the entire frequency domain, as these large scale eddies, containing low frequency information, break down into smaller vortices, containing higher frequency information.

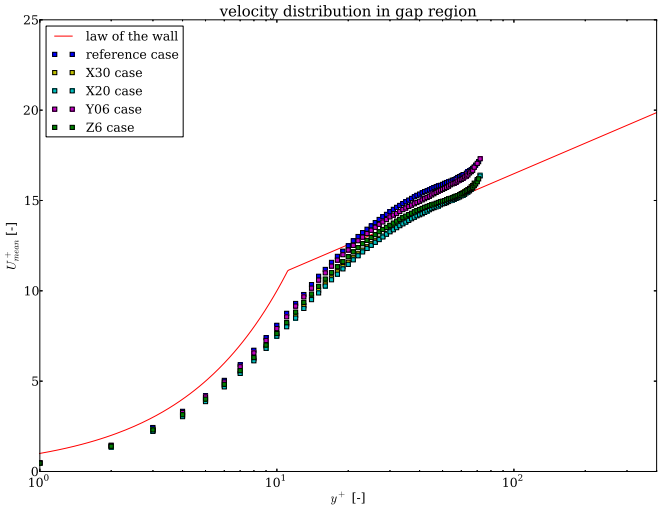

(a) Gap region

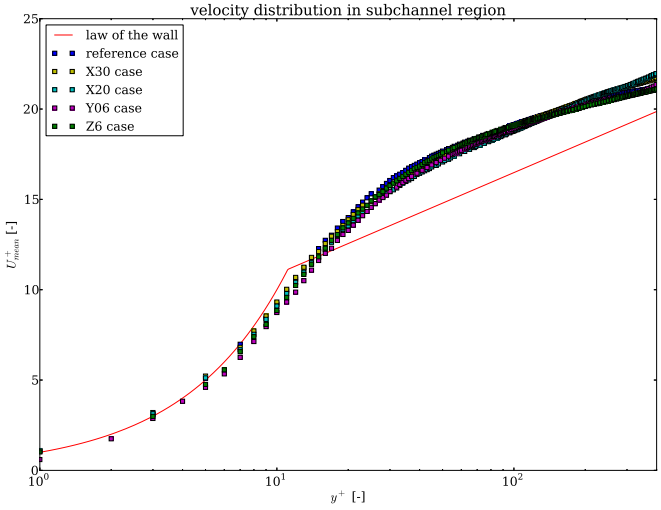

(b) Subchannel region

Figure 3.1: Dimensionless mean velocity distributions for simulations on different grids.

The geometry of the reference case is given in Table 3.3. The resulting $\frac{L}{D_h}$-ratio equals 15, as specified in section 2.1. To check the length convergence of the reference case, its wall-pressure PSD spectrum is compared to that of an identical simulation on a flow domain that is twice as long, referred to as the L/D_h 30 case. This PSD spectrum is obtained in the subchannel region: more large-scale vortices are expected to be present here, as the

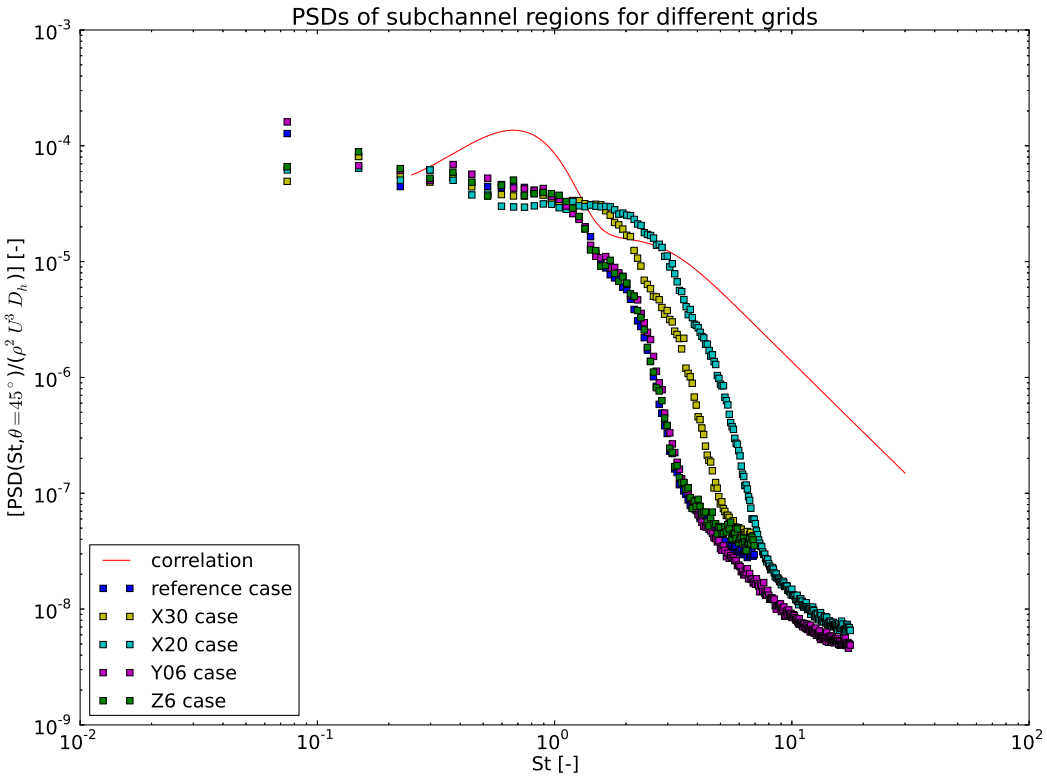

Figure 3.2: The dimensionless PSD spectrum in the subchannel region for the different grids as a function of the Strouhal number.

free flow section in the subchannel region is larger compared to the gap region. The result is given in Figure 3.3
Both PSD spectra correspond very well over the entire frequency range. This proofs that the flow domain length has no distinct influence on the solution: the solution is shown to be converged in terms of flow domain length.

To further prove the importance of a sufficiently long flow domain, and to show the consequences of a flow domain that is chosen too short, Figure 3.4 compares wall-pressure PSD plots of simulations run on a long flow domain - the L/D_h 30 case -, and a short one - the L/D_h 1 case - (Table 3.3). The wall-pressure amplitudes in the short flow domain are significantly lower over the entire frequency range, as was predicted in section 2.1. The lower frequency content in the the L/D_h 1 case could have been predicted earlier by comparing the pressure gradients over the flow domain: the $\frac{\Delta p}{L}$-ratio of L/D_h 30 case is a

Table 3.3: The flow domain properties of the cases used to check flow domain length convergence.

Name	D [m]	P [m]	L [m]	$D_h[m]$	$\frac{L}{D_h}$ [-]	# cells
reference case	0.2	0.217	1.5	0.1	15	2,620,800
L/D_h 30 case	0.2	0.217	3	0.1	30	5,241,600
L/D_h 1 case	0.2	0.217	0.1	0.1	1	174,720

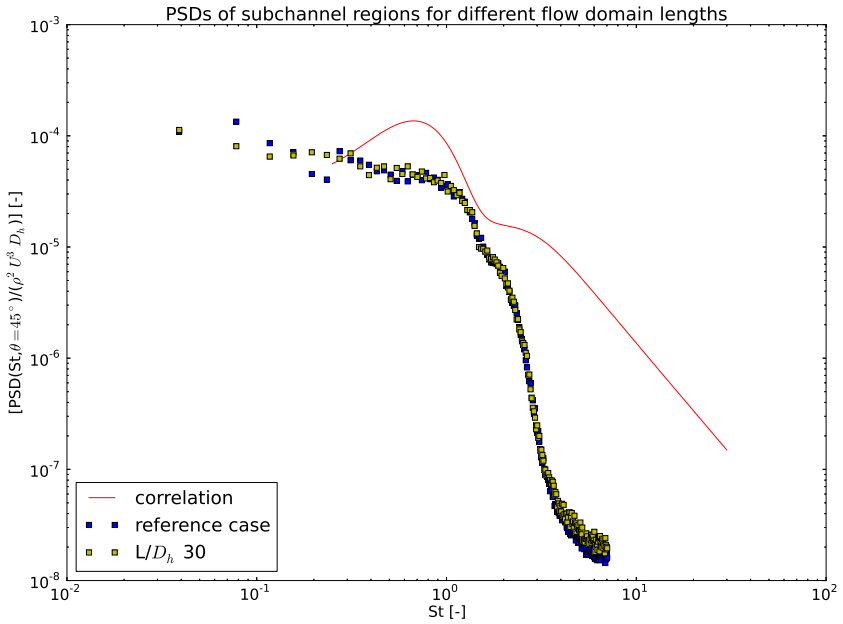

Figure 3.3: The dimensionless PSD spectrum in the subchannel region for two flow domains with different lengths, as a function of the Strouhal number.

factor 4 larger. This indicates a larger turbulence intensity, thus more and larger vortices are present, and the wall-pressure frequency content is higher.

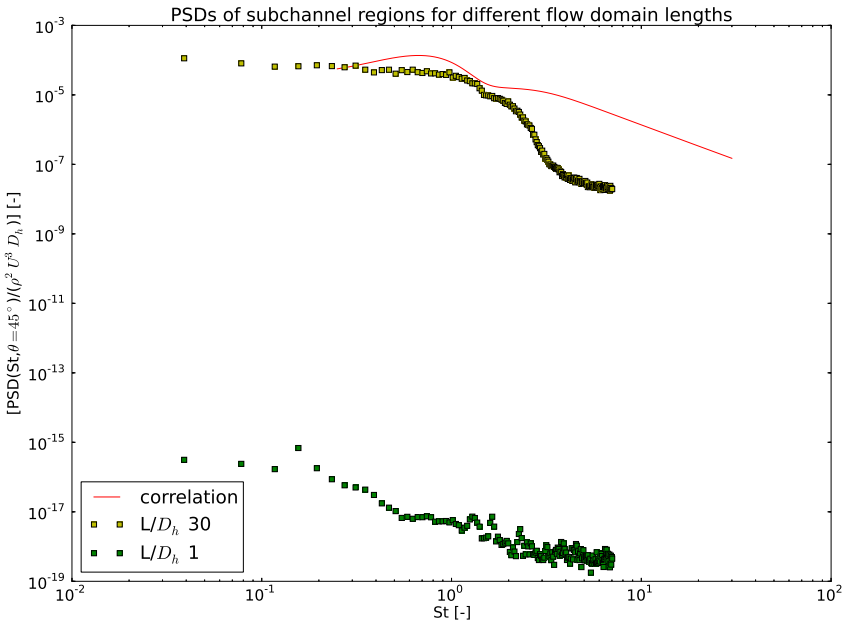

Figure 3.4: The dimensionless PSD spectrum in the subchannel region for two flow domains with different lengths as a function of the Strouhal number.

Chapter 4

Analysis of the pressure spectra in a square array

In this chapter, the results obtained with the reference case are discussed. PSD, CSD and coherence spectra of wall-pressures are plotted and studied. The most important features are pointed out, and the influence of Strouhal number and position on the cylinder are extracted from the results. The main geometric and flow properties of the reference case were given in Table 3.1 in chapter 3.

4.1 Power spectral density of pressure

Comparison of PSD functions at different positions on the cylinder is facilitated when the PSD amplitude is plotted as a function of position and frequency, as shown in Figure 4.1(a) for the reference case, and Figure 4.1(b) for Curling's correlation. In these contour plots, some resolution is sacrificed to obtain a better overview.
Because of the symmetry of the geometry, and the method of spectra calculation (sec. 2.5.2), only θ-values ranging from 0° to 90° are studied. Similar results are expected for PSD spectra at positions θ and $(90^\circ - \theta)$ because of additional geometry symmetry axis. θ was defined in Figure 2.6, section 2.5.1.

At very low frequencies, the amplitude of the pressure spectra is high, regardless of the position on the cylinder, indicating high amplitude fluctuations at low frequencies. Large vortices with large time-scales are responsible for these low-frequency fluctuations. One might be surprised that even in the tightly spaced gap region (at $\theta = k \cdot 90^\circ$, $k \in \mathbb{Z}$),

volumetric large scale vortices are present. However, as explained in section 1.2.4, there is a vortex street present at this location, consisting out of alternating large-scale vortices.

At higher frequencies or Strouhal numbers, the pressure spectra quickly drop. However, an increase in frequency content is noticeable at a Strouhal number between 0.25 and 0.45. This increase is larger for positions on the cylinder near the gap region, at $\theta = 15°$ and $\theta = 75°$. This can be explained when one assumes that the axis along which the vortex street is convected (sec. 1.2.4), is located at these positions. Figure 4.2 shows the velocity magnitude along a side plane of the flow domain. A lower velocity contour is observed near the gap region. The zigzagging nature of the contour can be explained by the alternating vortices at both sides of the gap. This also explains the alternating positive and negative velocity magnitudes in Figure 4.3, showing the velocity magnitude perpendicular to the flow domain side planes for two adjacent flow domain planes.
The vortex spacing λ, defined in Figure 1.4 in section 1.2.4, has a value in between 0.1m and 0.3m, based on Figure 4.3. Equation 1.8 predicts an vortex spacing of 0.15m. These values agree well.

For $St > 0.5$, the PSD decreases uniformly. This suggests that small, high frequency vortices induce smaller pressure amplitude fluctuations. These smaller vortices contribute more to the PSD amplitude in the subchannel region compared to the gap region. There, the vicinity of the cylinder walls increases damping and smaller vortices are dissipated faster.

The PSD obtained by the reference case corresponds reasonably well with Curling's correlation. However, the PSD peaks, present in the reference case near the gap region, are not present in the correlation. Instead, the correlation shows a strong increase in frequency content in the subchannel region for Strouhal number ranging from 0.5 to 1. The influence of entrance effects, the correlation's experimental uncertainty, and other explanations for this mismatch, were given in section 3.1. Also, based on the different location of the pressure peak, Curling's correlation does not take the vortex street into account. In the very low frequency range ($St < 0.25$), the correlation is not valid, which is the reason for the blank part in the figure.

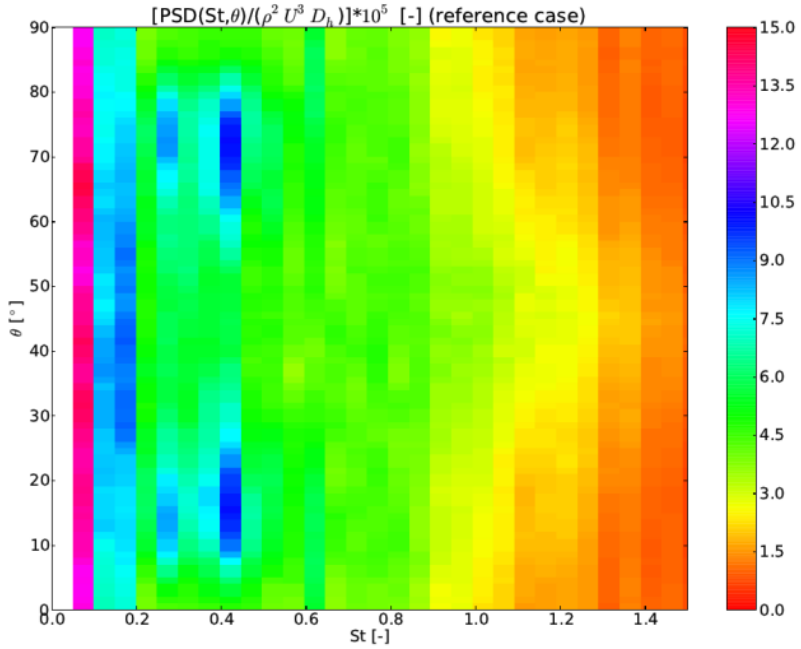

(a) reference case

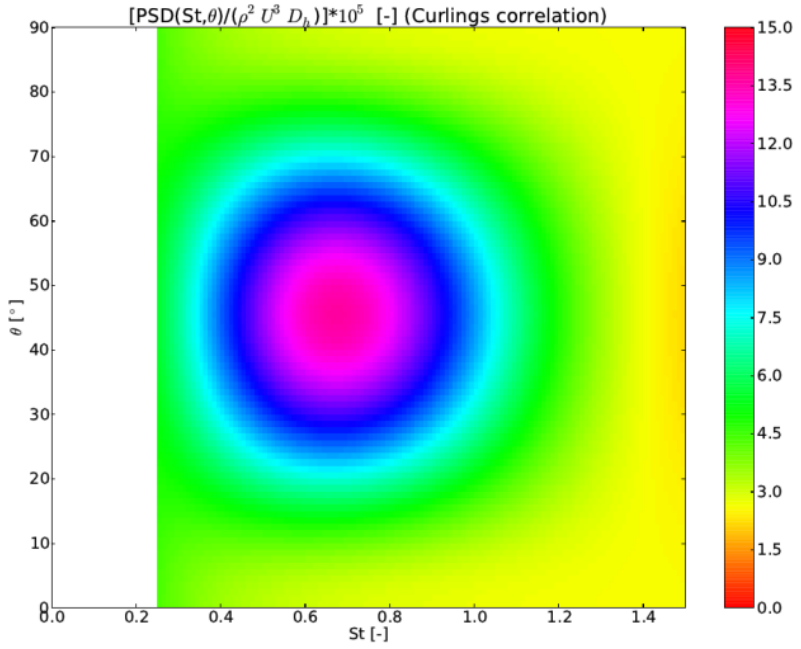

(b) Curling's correlation

Figure 4.1: Contour plots of the dimensionless PSD spectra as a function of the angular position on the cylinder and Strouhal number.

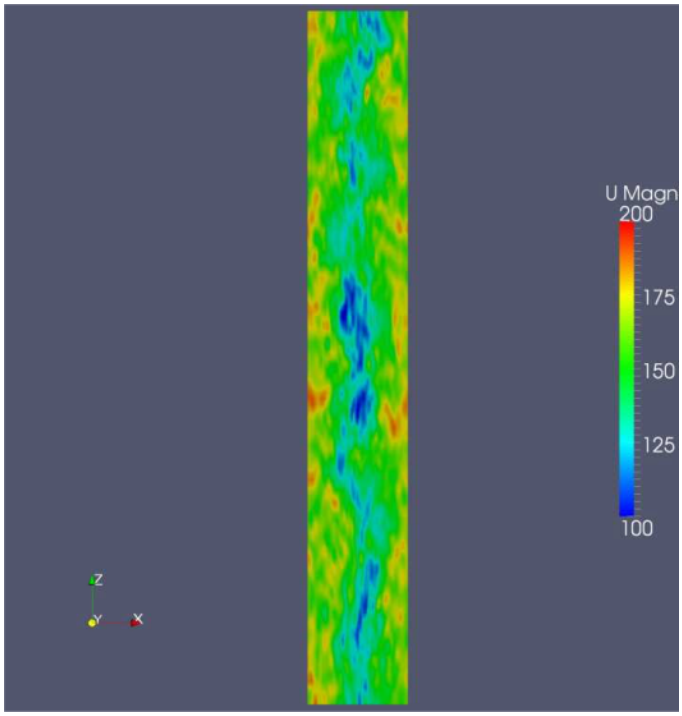

Figure 4.2: The velocity magnitude along a flow domain side plane.

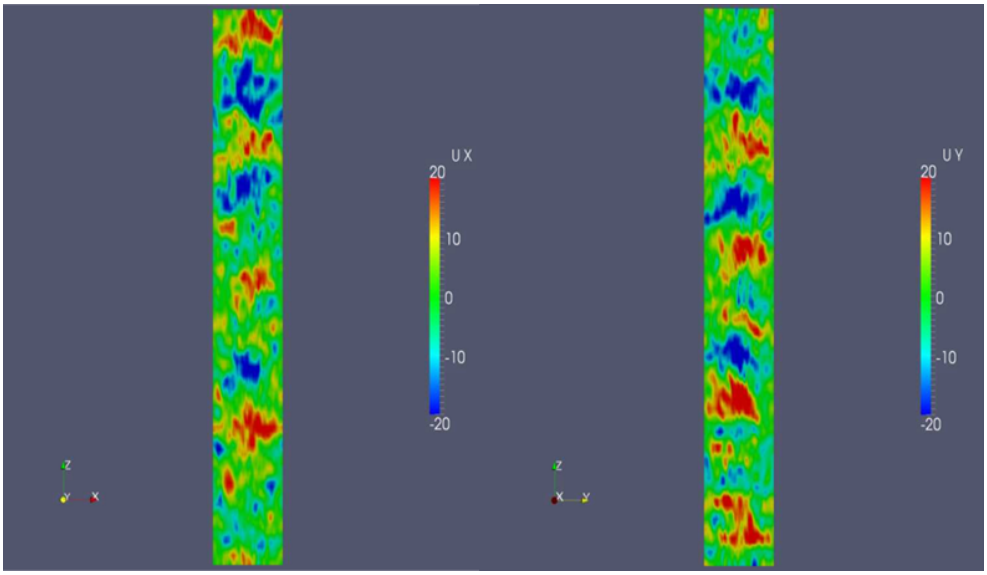

Figure 4.3: The velocity magnitude perpendicular to the main flow direction on the flow domain side planes, for two adjacent planes.

4.2 Cross-spectral density and coherence of pressure

The cross-correlation of the pressures is studied in two directions: one in which the circumferential coordinate is varied, and one where the axial coordinate changes. As CSDs and coherences are functions of 4 variables (St, θ, θ', and $\overline{x}$), one 2D contour plot is not sufficient to visualize all possible spectra, as was the case with the PSD plots.
To study the relation between different points on the cylinder surface, filtering out the influence of the pressure amplitude, coherence plots are made (sec. 1.3.4). The cross-spectral density can be extracted from the coherence and PSD (sec. 1.3.4).

$$\gamma_{\vec{x_1}\vec{x_2}}(St) = \frac{CSD_{\vec{x_1}\vec{x_2}}(St)}{\sqrt{PSD_{\vec{x_1}\vec{x_1}}(St)PSD_{\vec{x_2}\vec{x_2}}(St)}} \ , \tag{4.1}$$

hence, to avoid an overload of figures, only the coherences are plotted. Note that the phase angle of the CSD equals the one of the coherence. This follows from the coherence definition and the phase angle of the PSD being identically zero.

In contrast to the PSD analysis, the coherence analysis can not be limited to only one quarter of the flow domain. Due to the periodic boundary conditions, a shift in circumferential position of 90° or more, corresponds to the coherence between points on different cylinders, adjacent to the same subchannel (Fig. 2.8). The choice of a fixed circumferential coordinate, however, can be limited to to only one cylinder: due to the method of CSD and PSD calculation (sec. 2.5.2), a shift of this coordinate over 90° corresponds to an identical spectrum, also shifted over 90°.

The influence of the circumferential and axial coordinates on the CSD and coherence spectra are studied for a fixed circumferential coordinate in the gap region, and for one in the subchannel region. This corresponds to the two extreme cases.

4.2.1 Circumferential cross-correlation in gap region

The influence of the circumferential coordinate on the coherence is studied in Figures 4.4 and 4.5, which show the contour plots for the coherence amplitude and phase respectively for varying θ' and Strouhal number, for $\overline{x} = 0$, and a fixed circumferential coordinate in the gap region. The plots for Curling's correlation are only shown up to $\theta' = 90°$, in accordance with the reasoning in section 2.5.4. Note that because the fixed circumferential coordinate is chosen on a geometric symmetry axis, the plots are symmetric around that coordinate.

At first glance, there is again a good agreement between Curling's coherence amplitude plot (Fig. 4.4(b)) and the one obtained with the reference case (Fig. 4.4(a)). In section 1.3.4, it was stated that the PSD is an upper limit for the CSD. This can be observed in the plots. Indeed: the coherence magnitude at $\theta = 0°$ is unity, and larger than or equal to those at other circumferential positions, for all Strouhal numbers. Moving away from the gap region, the coherence magnitude quickly drops, especially at higher frequencies. This is because the large scale vortices span longer distances, thus they induce pressures at points separated over longer distances. The small vortices span much smaller distances. Another important observation is the high coherence magnitude in the gap region on the opposite side of the flow domain, at $\theta' = 180°$. This results mainly from the periodic boundary conditions between opposite sides of the flow domain, allowing vortices to exist at both subchannel sides simultaneously, thus highly correlating both sides. This was visualised in Figure 2.8. Only large scale vortices are physically capable of inducing pressure fluctuations at both sides of the subchannel, as only they span the entire subchannel width. The coherence magnitude in the same and opposite side gap regions, is a decreasing function of the Strouhal number. Keep in mind that the scope of the thesis is limited to Strouhal numbers equal to 1.25 (sec. 3.1).

The Coherence phase plots show a zero-phase difference over the entire cylinder perimeter and frequency range. The fluctuations are in phase because vortices cross both positions on the cylinder at the same time.

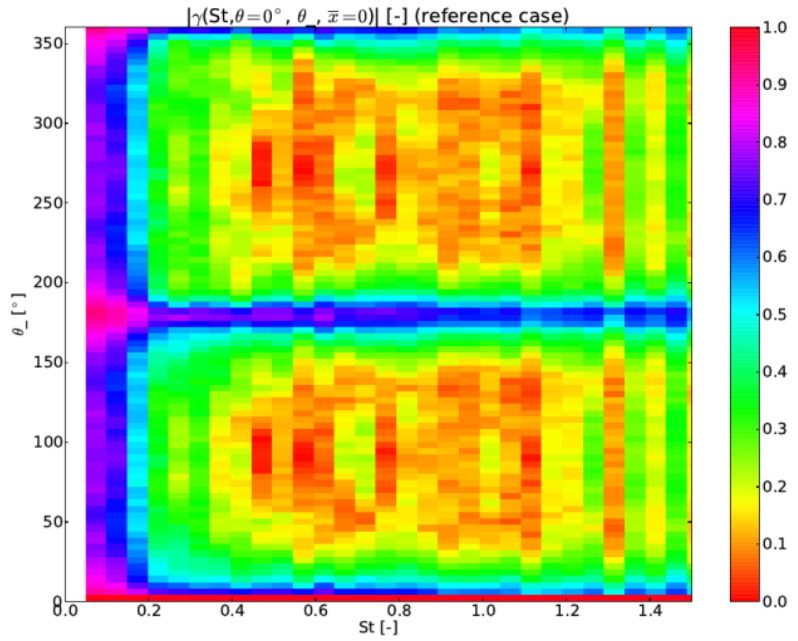

(a) reference case

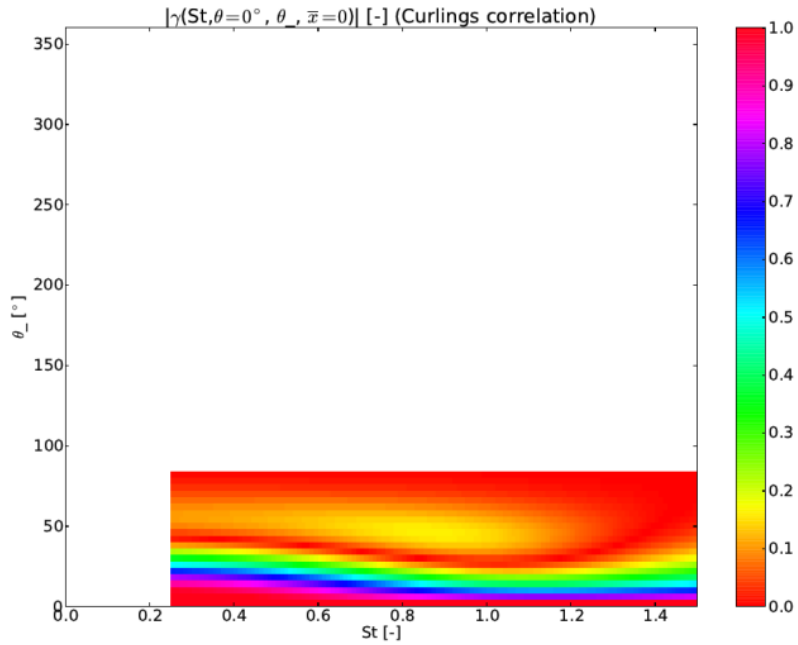

(b) Curling's correlation

Figure 4.4: Contour plots of the coherence amplitude between points at the same axial position, and one point's circumferential position fixed in the gap region.

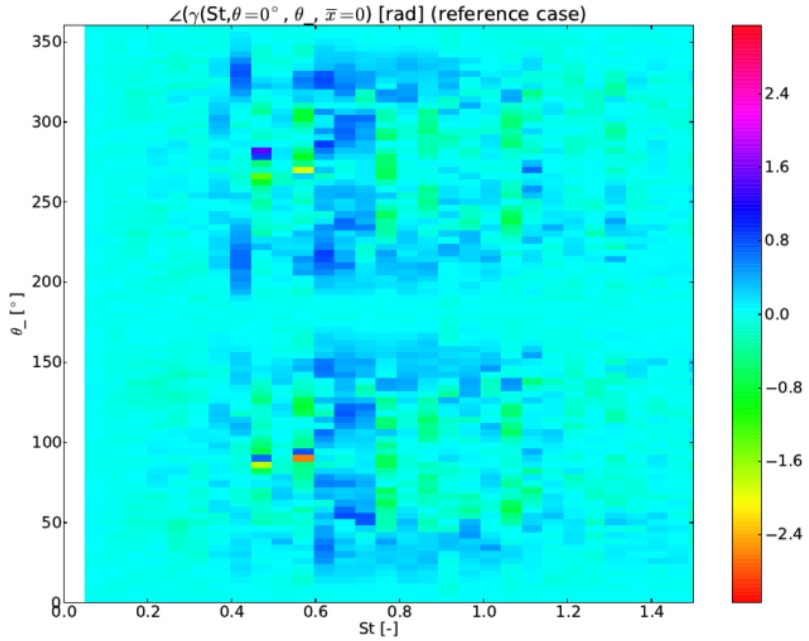

(a) reference case

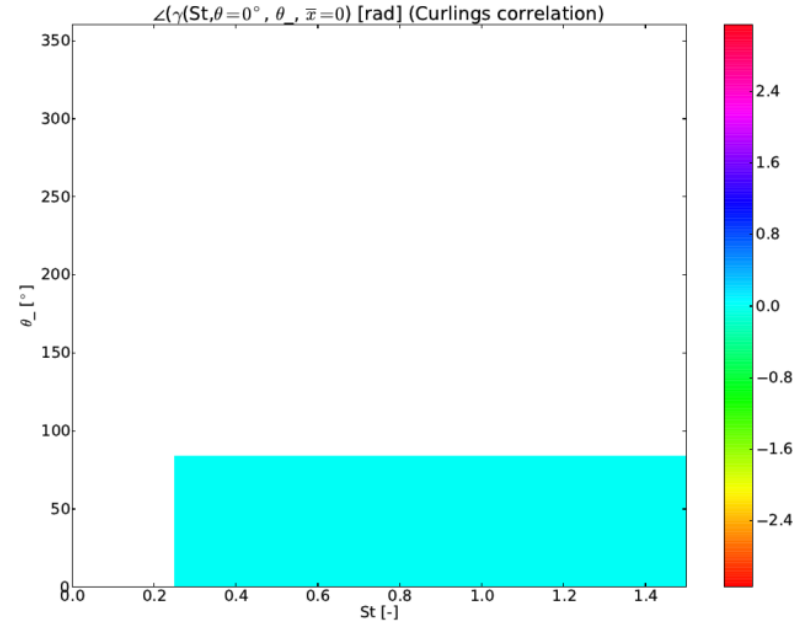

(b) Curling's correlation

Figure 4.5: Contour plots of the coherence phase between points at the same axial position, and one point's circumferential position fixed in the gap region.

4.2.2 Circumferential cross-correlation in the subchannel region

The same study as in the previous section is repeated here, but now for a fixed circumferential coordinate in the subchannel region. The coherence amplitude contour plots for the reference case and Curling's correlation are given in Figure 4.6. The phase plots are omitted because they are identically zero, as was explained in section 4.2.1. Once again, the fixed circumferential position is chosen on a geometric symmetry axis, hence the plots are symmetric around that coordinate.

The coherence amplitude in the subchannel region at $\theta' = \theta = 45°$ obviously is the highest, as at this position the CSD equals the PSD and consequently the coherence is unity. The magnitude quickly drops when moving away from this position. Curling's correlation shows the same trend, but less extreme.
In the first quadrant of the flow domain, the coherence in the low-frequency region up to $St = 0.5$ is important. Vortices large enough, responsible for the low St content, can span the distance from $\theta = 45°$ to $\theta \in]0°, 90°[$. In the same frequency range, the coherence on adjacent cylinders from $\theta \in [135°, 180°]$ and $\theta \in [270°, 315°]$ is high as well. Large scale vortices are able to span the subchannel width and influence adjacent cylinders. Diagonally adjacent cylinders are, however, not influenced by the same vortices, as the coherence amplitude for $\theta \in]180°, 270°[$ remains low.

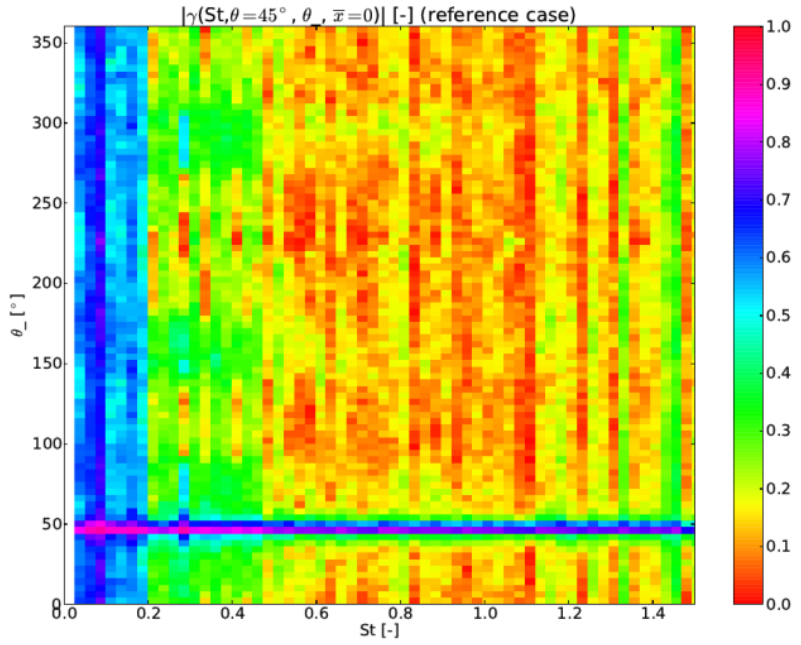

(a) reference case

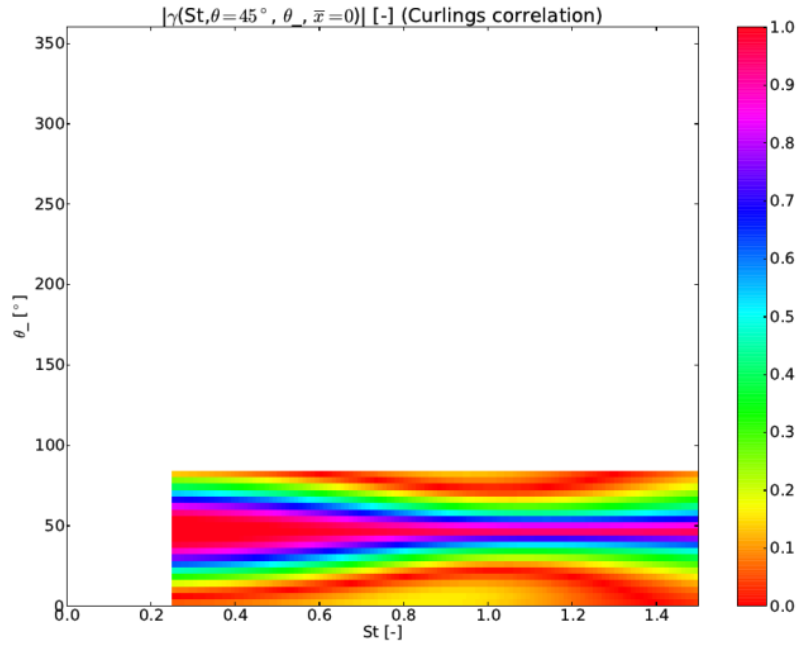

(b) Curling's correlation

Figure 4.6: Contour plots of the coherence amplitude between points at the same axial position, and one point's circumferential position fixed in the subchannel region.

4.2.3 Axial cross-correlation in the gap region

In this and the next section, the axial influence on the cross-correlation is analysed. First, the coherence is calculated between two points in the gap region, separated over an axial distance $\overline{x}$. Figures 4.7 and 4.8 show the coherence amplitude and phase for the reference case and Curling's correlation respectively.

The coherence amplitude plots for the reference case (Fig. 4.7(a)) and Curling's correlation (Fig. 4.8(a)) show a comparable evolution: the Strouhal number and axial distance between the points are inversely proportional for a constant coherence magnitude. Small vortices with high frequencies are quickly dissipated, and they do not exist anymore an axial distance $\overline{x}$ more downstream. Other small vortices generated by the energy cascade have taken their place. Curling proposes an exponential decay of coherence with distance and vortex frequency (ref. [5]).

$$\gamma \sim exp(-j2\pi f \frac{\overline{x}}{U}) \tag{4.2}$$

Larger vortices with lower frequencies are not dissipated as fast. They exist longer and consequently, they are able to induce pressure fluctuations further downstream. Therefore the coherence magnitude is large for low St and low $\overline{x}$.
A feature present in the reference case coherence plot but not in Curling's correlation, is intermittency: bands with coherence magnitude zero for constant $St \cdot \overline{x}$ can be observed. A better understanding of this phenomenon results from the analysis of the coherence phase plots.

The coherence phase plots for the reference case and Curling's correlation agree very well. Again, the effects of vortices dissipating more downstream is visible: for higher Strouhal numbers and axial separation, the phase becomes identically zero because the vortices are no longer correlated.
The bands in the plots are the result of the Fourier transform. The pressure distribution in time induced by the same turbulent structure a distance $\overline{x}$ more downstream, is the same, but shifted over a time $T = \frac{\overline{x}}{U_c}$. The Fourier transform of these functions therefore only differ by a factor $exp(-j\omega T)$, with $\omega = 2\pi f$ the radial frequency. Indeed, the Fourier transform of a signal shifted in time is given by

$$FT[f(t-T)](\omega) = FT[f(t)](\omega) \cdot exp(-j\omega T) \tag{4.3}$$

The frequency resolution is too low for the phase distribution to be clearly visible. This

is due to the extensive time-averaging (sec. 2.5.2) and the resolution limit imposed by the Nyquist theorem (sec. 1.3.1).
The coherence phase angle drops proportional to the Strouhal number, as is shown in Figure 4.9(b), showing the CSD phase plot for points in the gap region, spaced over an axial distance $\overline{x} = 3D_h$, as a function of the Strouhal number. This is a consequence of the convection transport of vortices with the flow. A vortex travels from the first to the second point in a time t, dependent on the convection speed U_c and the distance between the points $\overline{x}$. During that time, the vortex will complete a number of periods, dependent on its eddy turn-over time (ref. [21])

$$t_L = \frac{l}{U_c} \ . \tag{4.4}$$

The turn-over time of a small vortex is smaller than that of a large one. Hence, it will complete more periods over the same time or axial distance interval, and its phase will have dropped more.
The accompanying CSD amplitude plot in Figure 4.9(a) shows the amplitude distribution over the Strouhal number. This amplitude becomes zero everytime the phase angle crosses $\pm 180°$ and is at a maximum for phase angle 0°. This is the reason why the intermittency in Figure 4.7(a) is present. J. De Ridder et. al., 2015 (ref. [6]), encountered similar bands in CSD and coherence spectra of pressures on cylinders in axial flow, and attributed this to the transport of irrotational vortices. Figure 4.10 shows the pressure profile due to a regular series of irrotational vortices in solid line, and this same pressure distribution shifted over 180° in dashed line. Obviously, the CSD multiplying both pressure distributions, is at a maximum at phase difference 0° and near zero at 180°.

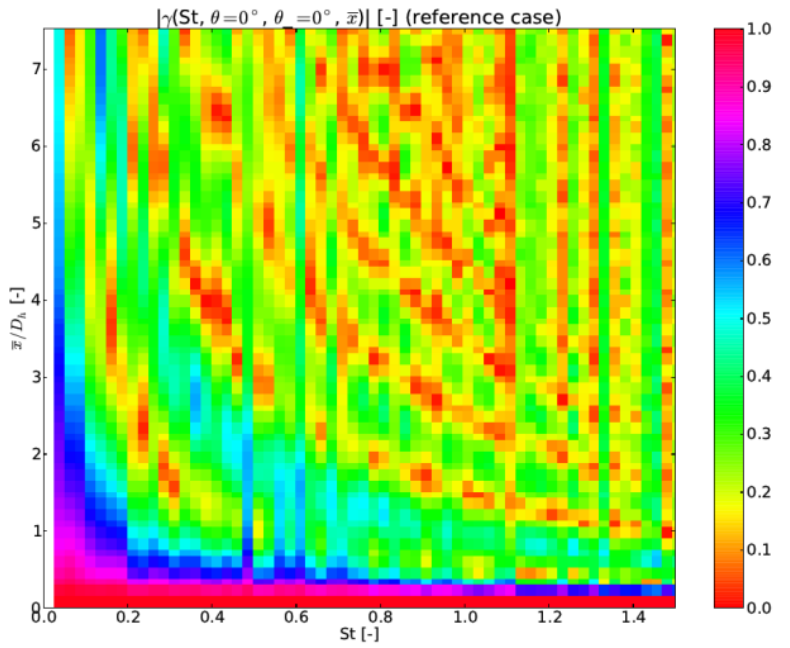

(a) amplitude

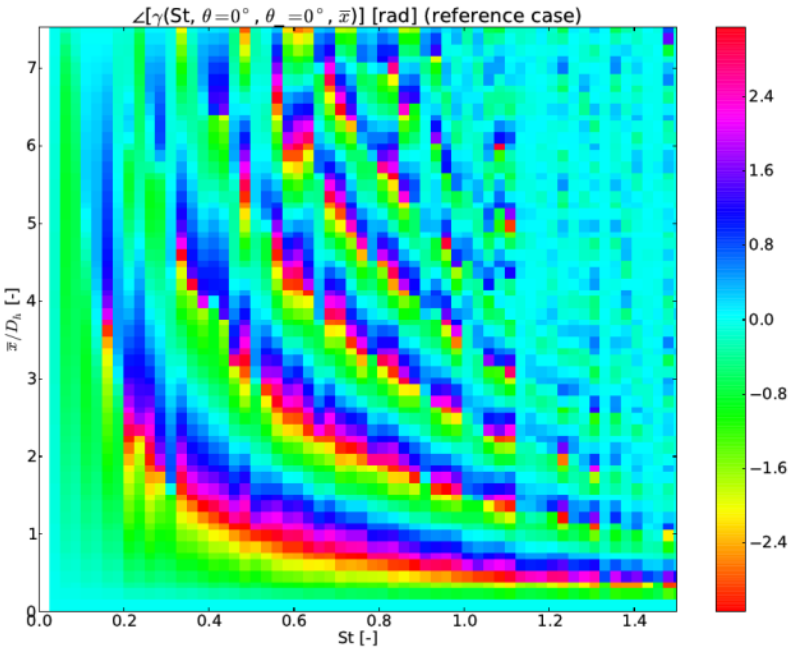

(b) phase

Figure 4.7: Contour plots of the coherence between points in the same gap region, separated over an axial distance, for the reference case.

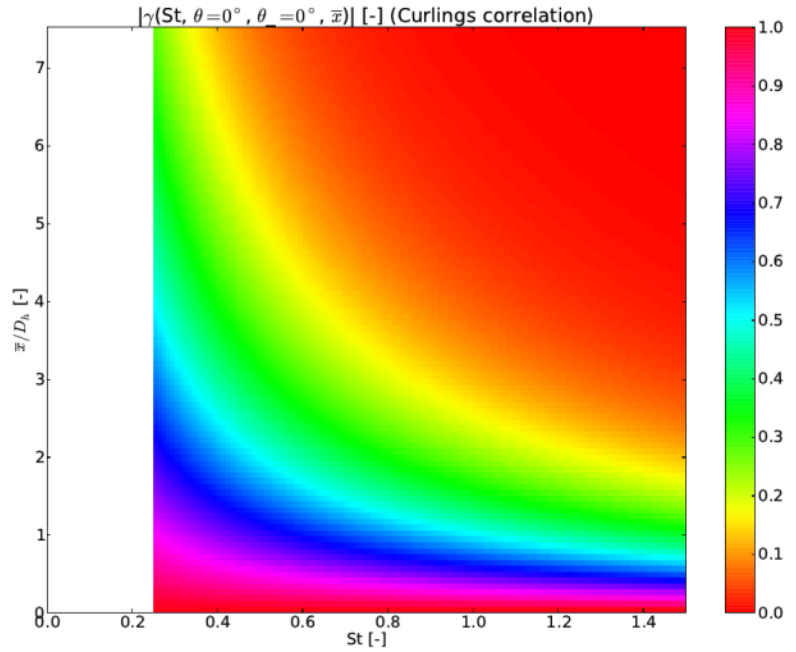

(a) amplitude

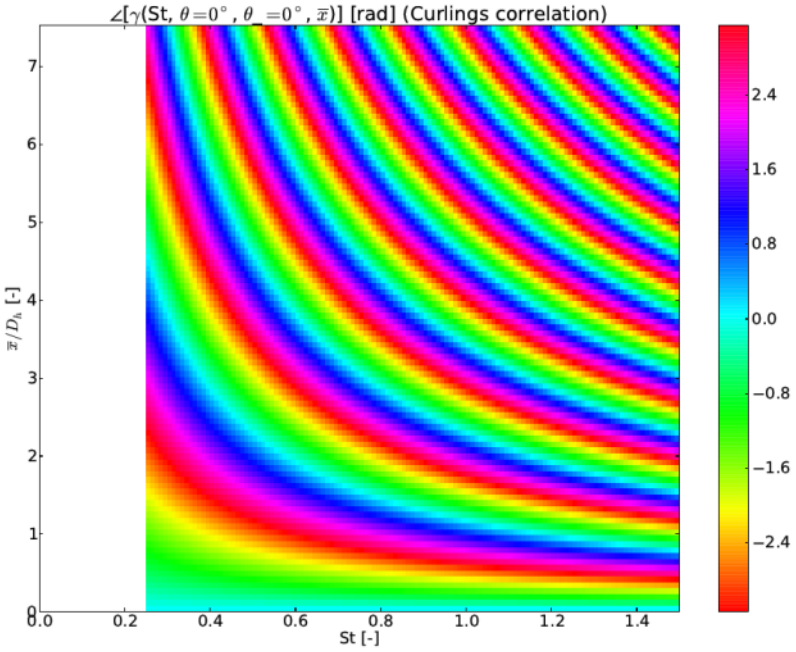

(b) phase

Figure 4.8: Contour plots of the coherence between points in the same gap region, separated over an axial distance, for Curling's correlation.

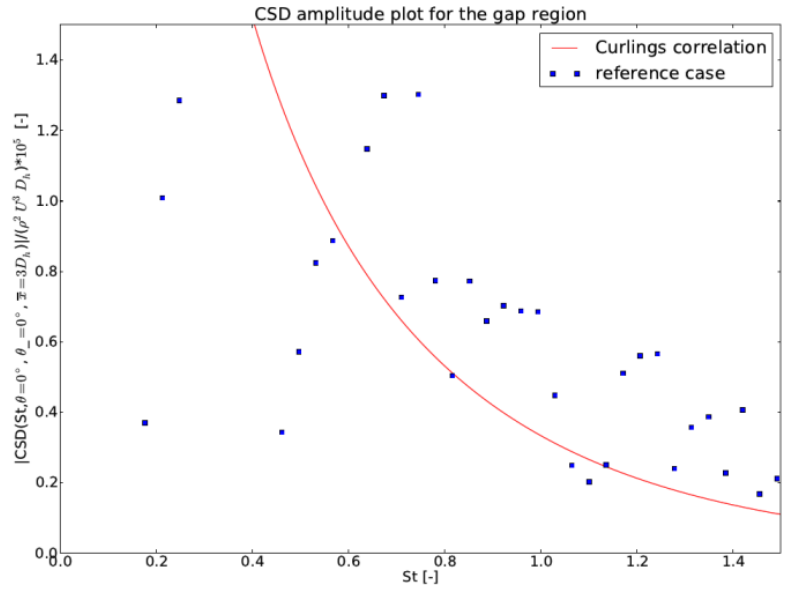

(a) amplitude

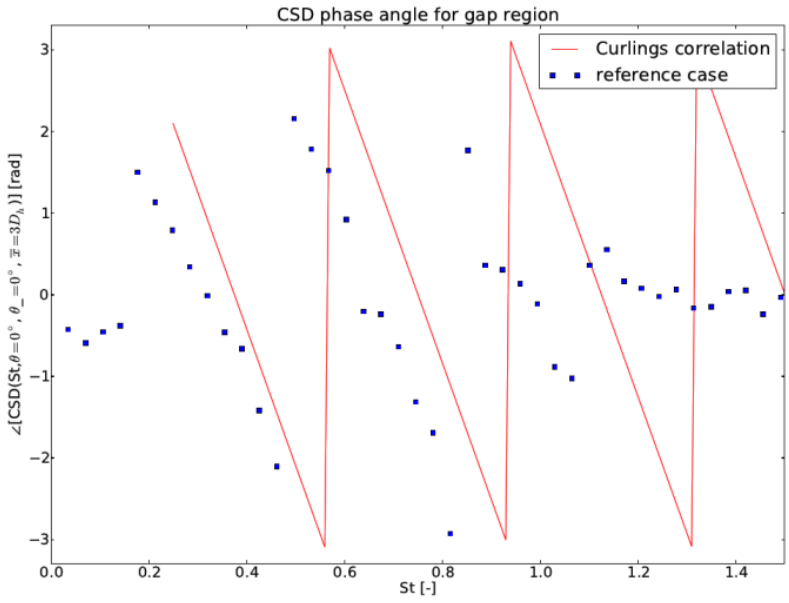

(b) phase

Figure 4.9: CSD plots between points in the same gap region, separated over an axial distance $3D_h$. The red curve represents Curling's correlation, the blue squares the reference case.

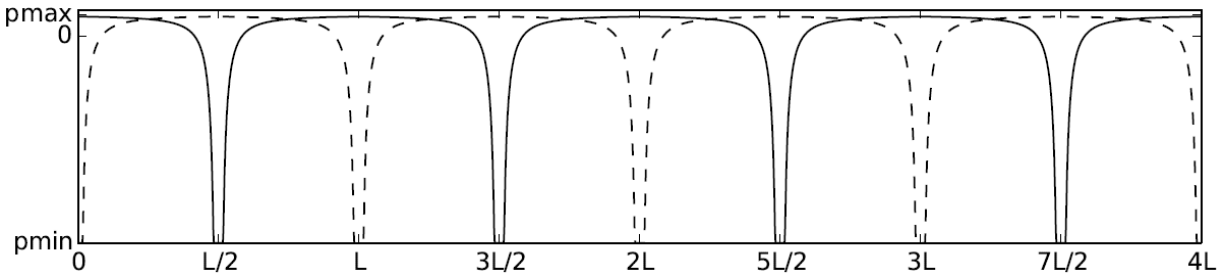

Figure 4.10: The pressure distribution of a series of irrotational vortices in solid line. The dashed line represents the same pressure distribution shifted over 180° (ref. [6]).

4.2.4 Axial cross-correlation in the subchannel region

In this section, the coherence between points in the subchannel region is investigated as a function of the Strouhal number and their axial spacing. The coherence amplitude and phase contour plots for the reference case and Curling's correlation are given in Figures 4.11 and 4.12 respectively.

The coherence amplitude and phase plots strongly resemble those in the gap region (sec. 4.2.3). The same discussion thus applies. The only difference, besides the increased noise in the subchannel figures, is the slightly longer distance over which vortices are correlated in the gap region. This is due to the higher convection speed in the subchannel, compared to the gap region. Indeed, the free-flow velocity in the subchannel is higher than in the gap region. This is visualised in Figure 4.13, depicting the coherence phase angle for two points in the subchannel and two points in the gap region, spaced over an axial distance $\overline{x} = 3D_h$, for both the reference case and Curling's correlation. While the reference case plots show no significant difference between the subchannel and the gap region, Curling's correlation shows that the phase drops faster in the subchannel region. This is self-evident, as the phase drop is proportional the eddy turn-over time (eq. 4.4), and the velocity in the subchannel region is higher than in the gap region.
In the next chapter, extracting the influence of some important geometric and flow parameters on the spectral functions, the discussion of the influence on the coherence between axially separated points will be limited to points in the gap region. This is because of the similarity of the coherence spectra of the reference case in both regions, and to avoid an excessive number of images.

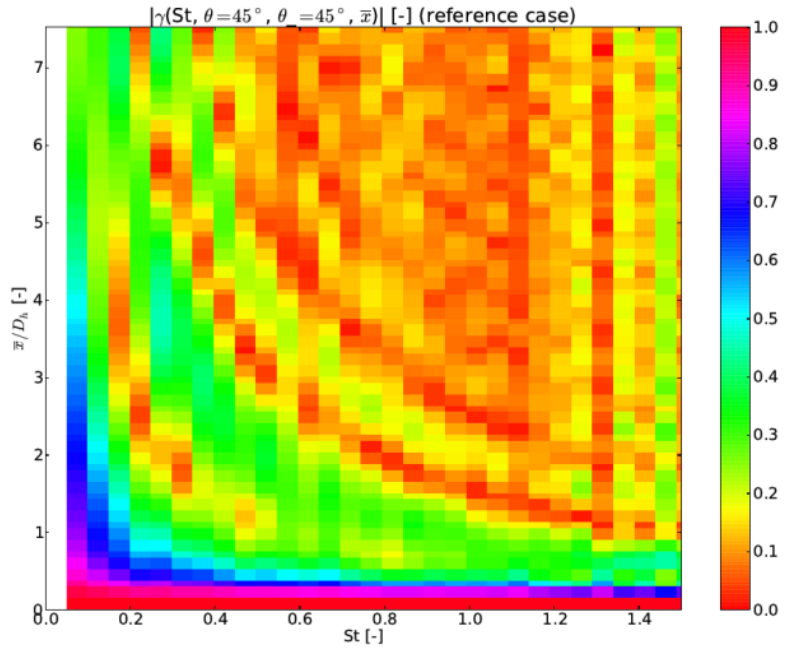

(a) Coherence amplitude

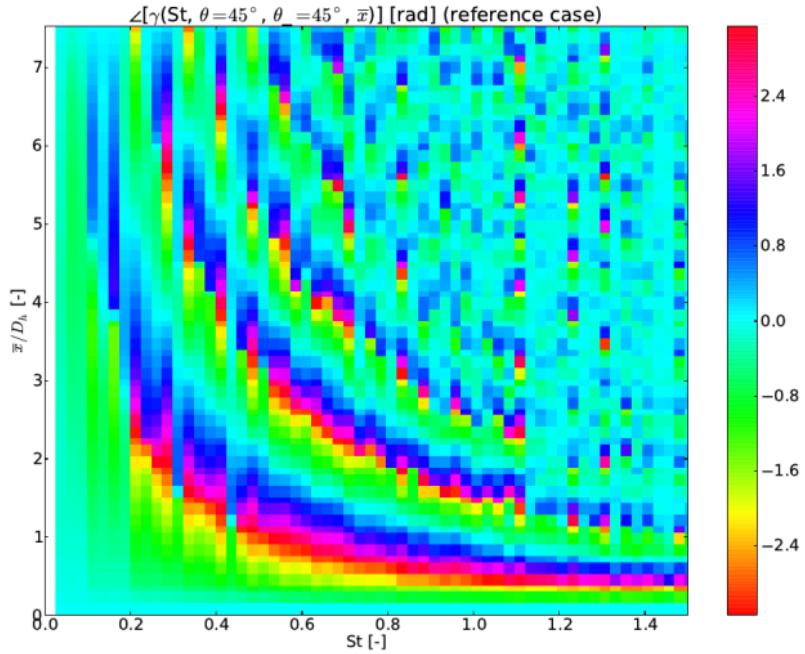

(b) Coherence phase

Figure 4.11: Contour plots of the coherence between points in the same subchannel region, separated over an axial distance, for the reference case.

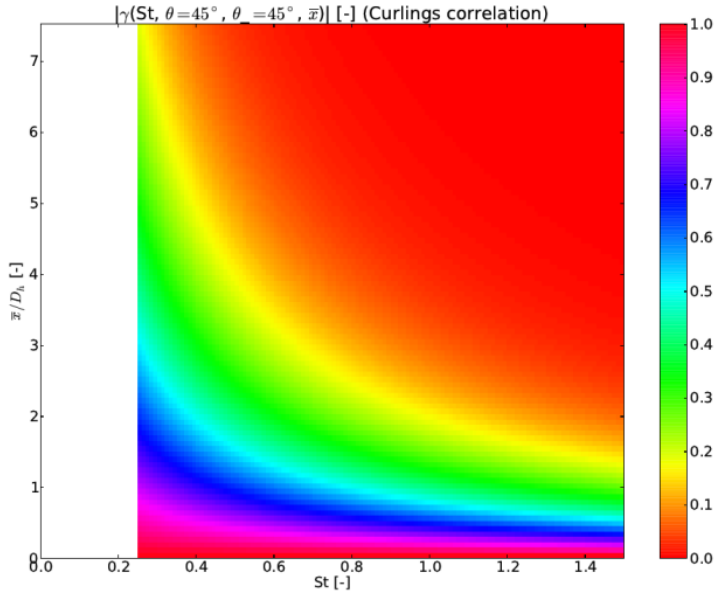

(a) Coherence amplitude

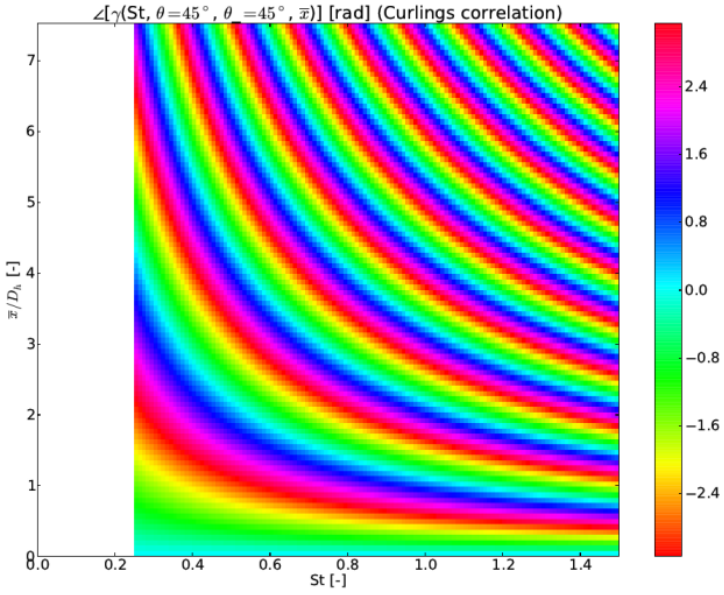

(b) Coherence phase

Figure 4.12: Contour plots of the coherence between points in the same subchannel region, separated over an axial distance, for Curling's correlation.

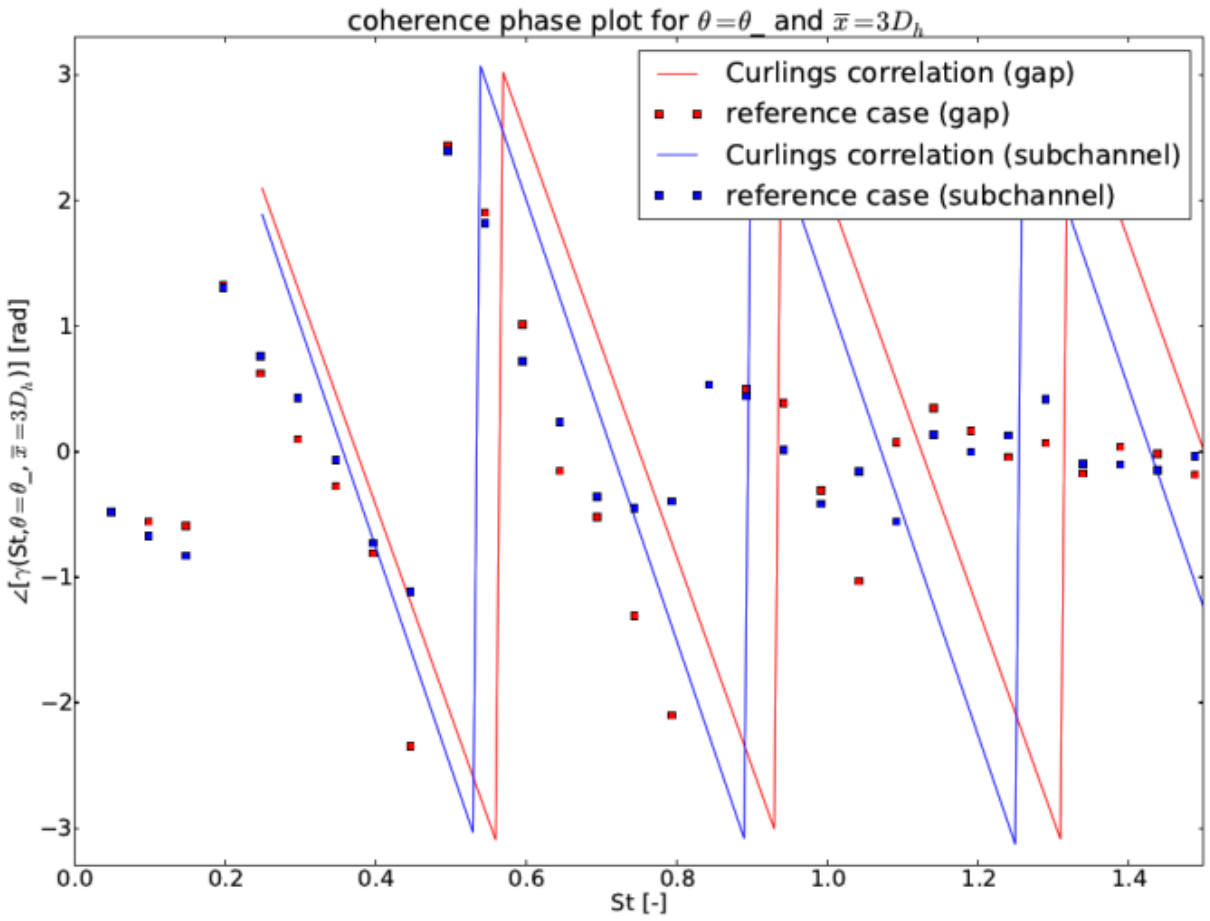

Figure 4.13: The coherence phase angle between points in the same subchannel and gap regions, separated over an axial distance $3D_h$.

4.3 Conclusions

In the final section of this chapter, the conclusions regarding the position and frequency influence on the pressure spectra for the reference case are listed. This is a brief summary of the results without further explanation, as all conclusions are already extensively discussed and explained in the previous sections.

A fixed circumferential coordinate on a geometric symmetry axis results in a symmetric frequency spectrum along this axis. This is due to the regular geometry. Because of the method of spectra calculation and symmetrical geometry, identical spectra are obtained when both coordinates are shifted over an angle of 90°.

As the frequency increases, the amplitudes of the pressure fluctuations decreases: vortices with smaller length and time scales induce smaller pressure amplitudes. There exists, however, a maximum in pressure fluctuation amplitude at a Strouhal number between 0.25 and 0.45. This maximum is due to the vortex street phenomenon. The maximum pressure amplitudes correspond with circumferential coordinates $\theta = 15°$ and $\theta = 75°$. The axes along which the vortex streets are convected, are located at these positions.
The high-frequency pressure spectra is broader in the subchannel region than in the gap region. In the latter, vortices are dissipated faster due to the close vicinity of the cylinder walls.

The cross-correlation amplitude between the pressures in two points is high for high fluctuation frequencies, only if the circumferential distance between them is small. The frequency then has little effect on the cross-correlation. For low fluctuation amplitudes, the pressures are highly correlated over the entire cylinder circumference: large vortices are able to span the entire subchannel width, inducing pressures over the entire subchannel perimeter. Fluctuation frequencies up to $St = 0.5$ are still significantly correlated, but only if they are located in the subchannel regions of the same or adjacent cylinders. The correlation between pressure fluctuations on diagonally adjacent cylinders, or in different gap regions, is non-existent for higher frequency fluctuations. The high cross-correlation between pressure fluctuations in opposite gap regions, shown in Figure 4.4(a), is mainly due to an artefact, especially for the high frequency fluctuations, created by the boundary conditions.
The coherence phase between pressure fluctuations in different points, only separated over a circumferential distance perpendicular to the main flow velocity, is identically zero over the entire cylinder surface and frequency range. This is because vortices cross these points at the exact same moment in time.

The cross-correlation between pressure fluctuations in points separated over an axial distance, parallel to the main flow, is significant only for low $St \cdot \overline{x}$-products. Large vortices do still exist a distance $\overline{x}$ more downstream, thus the pressure fluctuations induced there origin from the same vortices, and the cross-correlation remains high. Small vortices with high frequencies, are quickly dissipated and are replaced by other vortices a distance $\overline{x}$ more downstream. The pressure fluctuations in the two points origin from different vortices, hence they are not correlated.
The phase difference between highly correlated pressure fluctuations is due to the convection of the vortices: as vortices are convected with the flow, they complete a number of periods, proportional to the distance and eddy turn-over time. Large vortices have lower

eddy turn-over times and complete less periods over the same distance downstream than small high-frequency vortices. Therefore, the pressure fluctuation phase changes more over longer distances, and more rapidly for higher frequency fluctuations. The bands in the amplitude spectra can be explained by this phase distribution, and the assumption of irrotational vortex sequences. Indeed, the cross-correlation between pressures induced by vortices is at a maximum when the vortices are in phase, and zero when they are out of phase.

The cross-correlation of the pressure fluctuations between two points, separated over an axial distance, is almost independent of the circumferential position of the points. The gap and subchannel regions differ only in convection speed: the flow velocity is higher in the subchannel region, as the flow there is less influenced by the cylinder walls. Hence, the phase drops faster in the subchannel region, but this effect is only slightly visible in the plots.

Chapter 5

Parameter study

In the fifth chapter of this thesis, the influence of the Reynolds number, the pitch-over-diameter or $\frac{P}{D}$-ratio, and the array configuration on the pressure spectra is studied. Simulations with variations in one of these parameters are compared in order to extract their influence from the obtained results.

This comparison is performed on 3 quantities. Comparison of the PSD spectra reveals the parameter influence on the pressure fluctuation magnitudes. The second quantity is the coherence spectrum between two points with different circumferential coordinates. Therefore, the amplitude spectra are compared, once for a fixed coordinate in the gap region, and once for one in the subchannel region. The phase spectra of these coherences are omitted, because they are identically zero for a zero axial displacement between the points (sec. 4.2.1). The third quantity is the coherence spectrum between points in the gap region, axially spaced over a distance $\overline{x}$. Both phase and amplitude spectra are compared. Identical coherence spectra between points in the subchannel region have been omitted, because of the very close resemblance to the ones between the points in the gap region. No new information can be extracted from these plots.

The parameters of the simulations are changed such that the computational load of its simulation is lower than the one for the reference case.

5.1 Reynolds number influence

In this section, the influence of the Reynolds number is analysed. Two cases additional to the reference case are simulated, one with a Reynolds number of 10,000, and one with a Reynolds number 6,800. The change in Reynolds number is based on a change in flow velocity. Their characteristics are summarized in Table 5.1. These particular Reynolds numbers are chosen for two reasons. First, they allow for coarser meshes and thus lower grid sizes. Indeed, lower Reynolds numbers correspond with lower pressure drops over the flow domain length. The pressure drop per unit length - $\frac{\Delta p}{L}$ - is given in Table 5.1. From equations 2.2, 1.2 and 2.1, it follows that larger cell sizes can be chosen for the same dimensionless cell widths. The second reason, explaining their exact value, is because there is experimental data available to compare the results with. Curling (ref. [5]) performed experiments on cylinders in a square array, subjected an axial flow with these Reynolds numbers.

The PSD contour plots of the reference case, the Re 10000 case and the Re 6800 case are given in Figure 5.1.
The figures show a similar evolution of the PSD over the entire frequency range. However, the PSD magnitude is strongly dependent on the Reynolds number. Although the figures suggest that the amplitude of the pressure fluctuations increases with decreasing Reynolds number, especially with the different scaling, one must take into account that the dimensionless PSD magnitude is inversely proportional to the velocity U to the third power (eq. 1.11). Therefore, the actual amplitude of the pressure fluctuations is much larger for larger Reynolds numbers. This is self-evident: flows with larger Reynolds numbers exhibit higher turbulent intensities and contain more and stronger vortices. As these vortices are stronger, they obviously induce larger pressure fluctuations.
It seems like another feature is present in the figures: at lower Reynolds numbers, the tendency for small vortices to generate higher pressure amplitude fluctuations in the subchannel region than in the gap region, disappears, and the pressure fluctuation amplitude

Table 5.1: The properties of the cases used to check Reynolds number influence.

Name	D [m]	P [m]	D_h [m]	U $[\frac{m}{s}]$	ν $[\frac{m^2}{s}]$	Re_{D_h} [-]	$\frac{\Delta p}{L}$ $[\frac{Pa}{m}]$	# cells
reference case	0.2	0.217	0.1	140	0.001	14,000	2570	2,620,800
Re 10000 case	0.2	0.217	0.1	100	0.001	10,000	1480	1,463,000
Re 6800 case	0.2	0.217	0.1	68	0.001	6,800	830	739,200

decreases uniformly over the circumferential position with increasing Strouhal number, for large enough Strouhal numbers. However, this is contributed entirely to scaling effects: the higher pressure fluctuations at high frequencies in the subchannel region are present at all Reynolds numbers, although it is less visible in the plots with larger scales. This also means that the pressure fluctuations induced by smaller vortices, are less influenced by the Reynolds number.
The increase in PSD magnitude at $\theta = 15°$ and $\theta = 75°$ at $St = 0.3$ is present at all Reynolds numbers. This indicates the presence of a vortex street. Indeed, Figure 5.2 shows the velocity magnitude and velocity component perpendicular to the main flow along a flow domain side plane, for both the Re 10000 and Re 6800 cases. In both figures, a vortex street is visible. Although the vortex street is less strong for lower Reynolds numbers, its relative contribution to the PSD spectrum increases. The contribution of the main flow turbulence decreases fast with decreasing Reynolds numbers, while the vortex street phenomenon is still significant at lower Reynolds numbers (sec. 1.2.4).
Globally, it can be concluded that the Reynolds number has a profound influence on the magnitude of the pressure fluctuations, only little on their frequency distribution, and not on their spatial distribution.

Coherence amplitude contour plots, visualizing the cross-correlation between points with identical axial coordinates, with one point's circumferential coordinate fixed in the gap or subchannel region, are shown in Figure 5.3 and 5.4 respectively.
The distribution of the coherence looks similar over the entire circumferential and frequency range for all Reynolds numbers. The coherence magnitude increases slightly over the entire frequency and circumferential range for decreasing Reynolds number. This is due to an increase in noise because the overall lower PSD and CSD magnitudes for lower Reynolds numbers: division by a small PSD value increases the importance of random fluctuations on the coherence. Apart from this, it can be concluded that the Reynolds number has no influence on the coherence of pressure fluctuations in points at different circumferential positions.

Coherence phase and amplitude contour plots, visualising the cross-correlation between two points in the gap region, separated over an axial distance $\overline{x}$, are given in Figures 5.5 and 5.6.
The coherence phase and amplitude plots are identical for all three Reynolds numbers. The overall larger coherence magnitude for lower Reynolds numbers can again be attributed to the increased noise because of the low PSD value. The small differences present in the

figures at higher frequencies can be attributed to noise and randomness. It is concluded that the Reynolds number has no influence on the coherence of pressure fluctuations in points separated over an axial distance.

These plots are drawn on dimensionless frequency axes. The Strouhal number normalizes the frequency with the hydraulic diameter and the flow velocity ($St = \frac{fD_h}{U}$). Therefore, a given Strouhal number corresponds to a lower frequency for a flow velocity. Thus, the plots are quite similar on a dimensionless scale, but differ very much on an absolute scale. Figures 5.5 and 5.6 once again confirm the convection of vortices: at lower flow velocities, the vortices are transported slower. This means that their eddy turn-over time increases (eq. 4.4) and they complete more periods over the same axial distance. In absolute frequency, their phase drops more rapidly, and the bands in the amplitude spectrum are more closely spaced for lower flow velocities.

To summarize, lower Reynolds number flows induce smaller pressure fluctuations. The relative contribution of the vortex street to the pressure fluctuations increases. This shifts the PSD spectra to slightly higher frequencies, but the circumferential distribution is not influenced. The coherence amplitude spectra increase at lower Reynolds numbers, because the noise increases.
On dimensional frequency axes, the bands in the coherence spectra between axially spaced points are more closely spaced for decreasing flow velocity. This is due to the reduced speeds at which the vortices are convected.

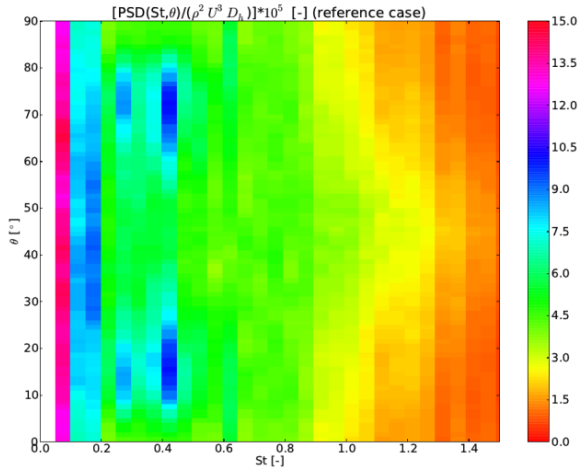

(a) reference case (Re 14,000)

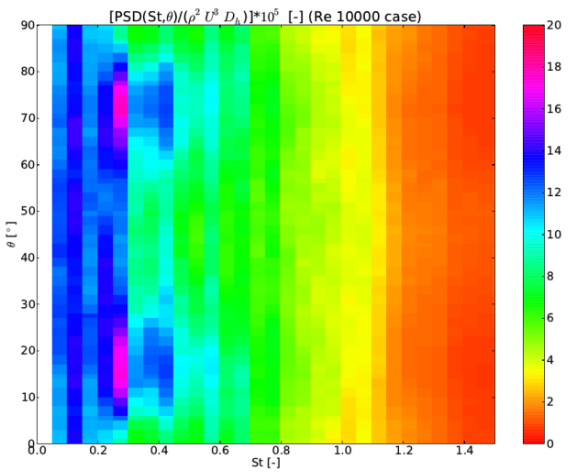

(b) Re 10000 case

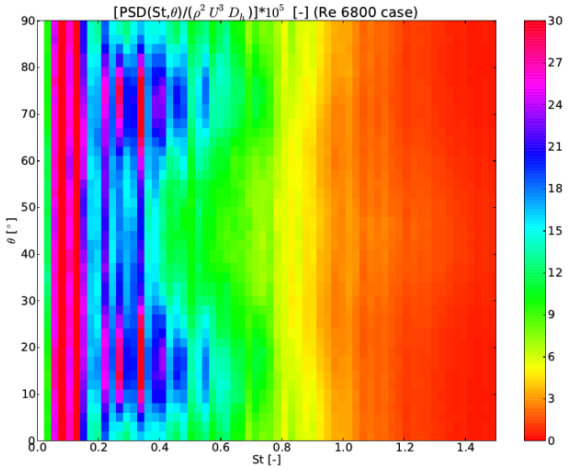

(c) Re 6800 case

Figure 5.1: Contour plots of the dimensionless PSD as a function of the position on the cylinder and Strouhal number, visualizing the influence of the Reynolds number.

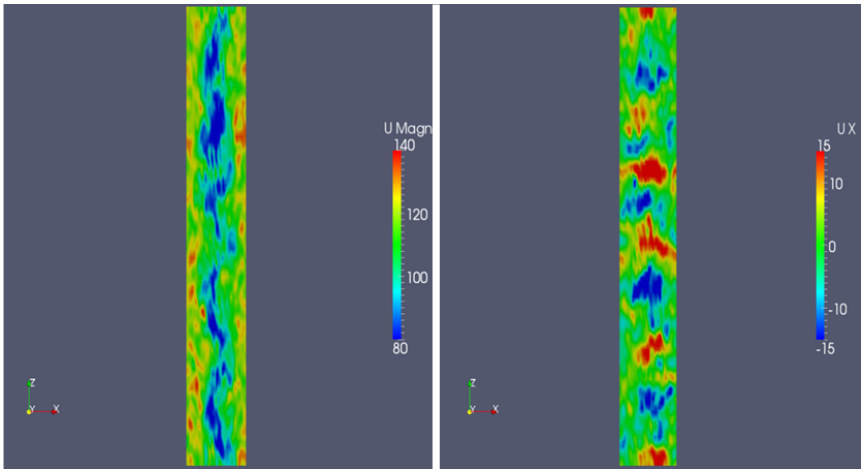

(a) Re 10000 case

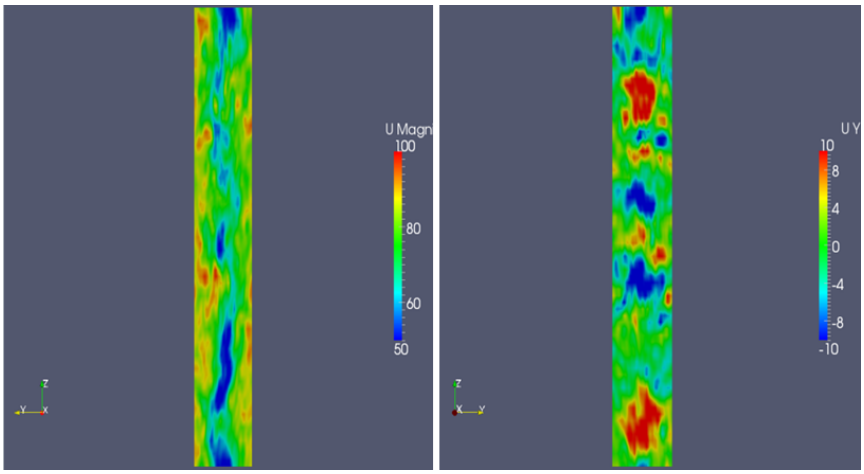

(b) Re 6800 case

Figure 5.2: Velocity magnitude (left) and velocity component perpendicular to the main flow (right) along a flow domain side plane.

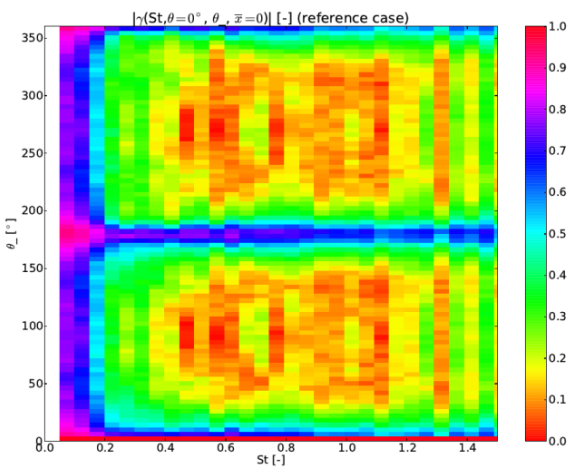

(a) reference case (Re 14,000)

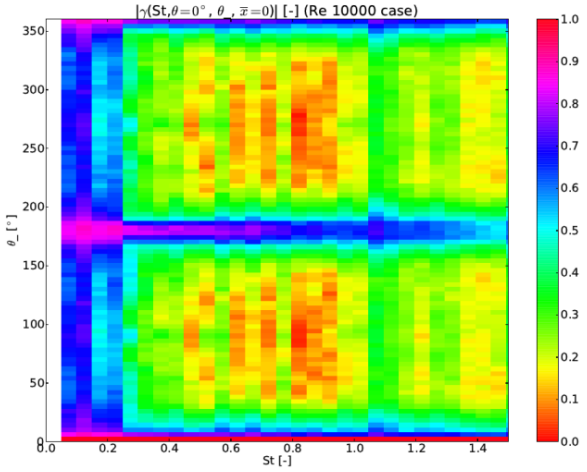

(b) Re 10000 case

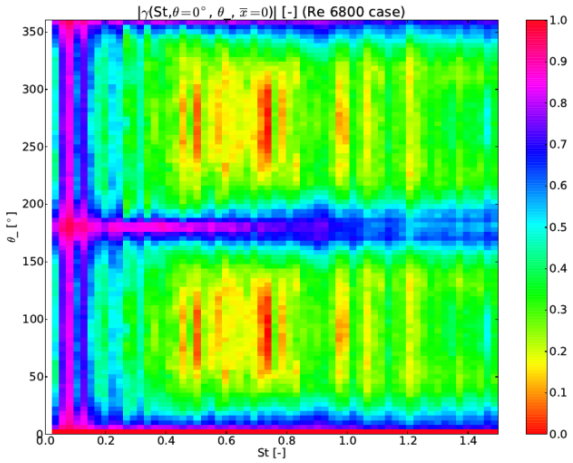

(c) Re 6800 case

Figure 5.3: Contour plots of the coherence amplitude between points at the same axial position, and one point's circumferential position fixed in the gap region, visualizing the influence of the Reynolds number.

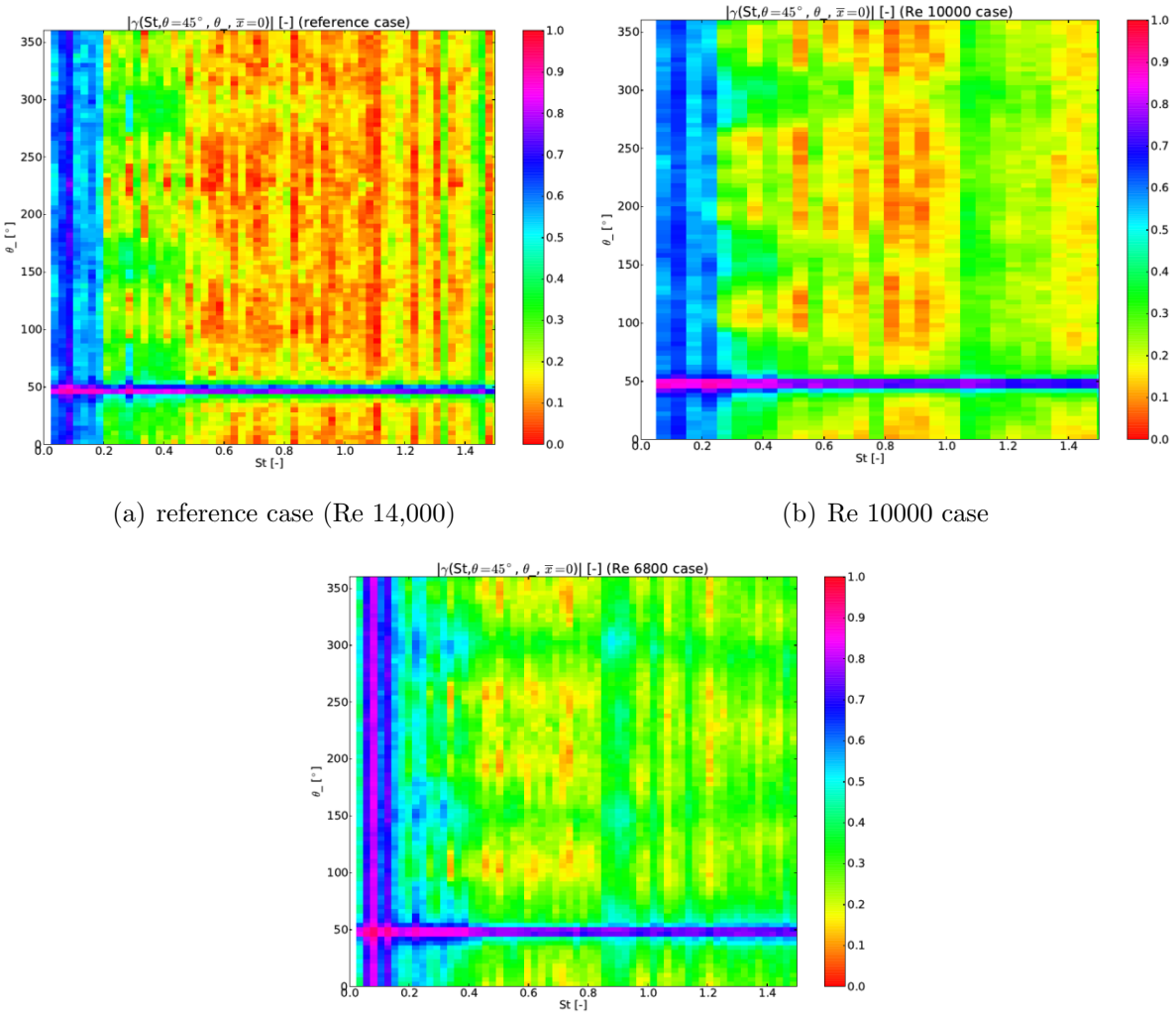

(a) reference case (Re 14,000)

(b) Re 10000 case

(c) Re 6800 case

Figure 5.4: Contour plots of the coherence amplitude between points at the same axial position, and one point's circumferential position fixed in the subchannel region, visualizing the influence of the Reynolds number.

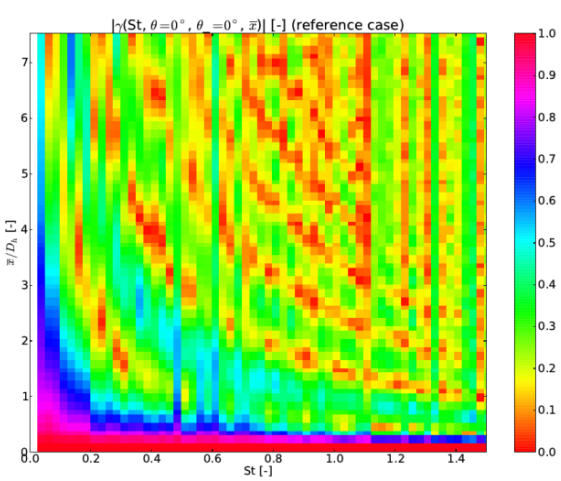

(a) reference case (Re 14,000)

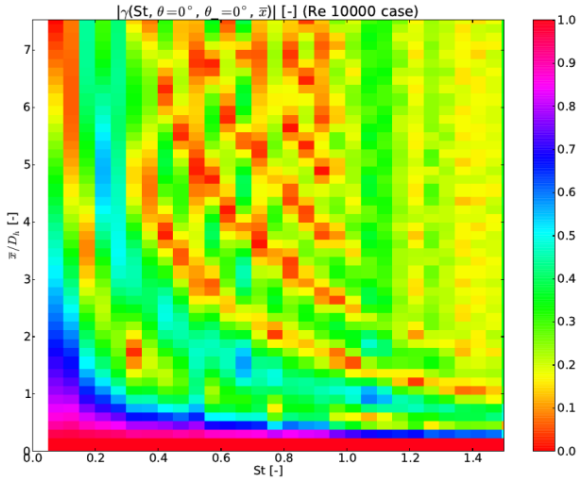

(b) Re 10000 case

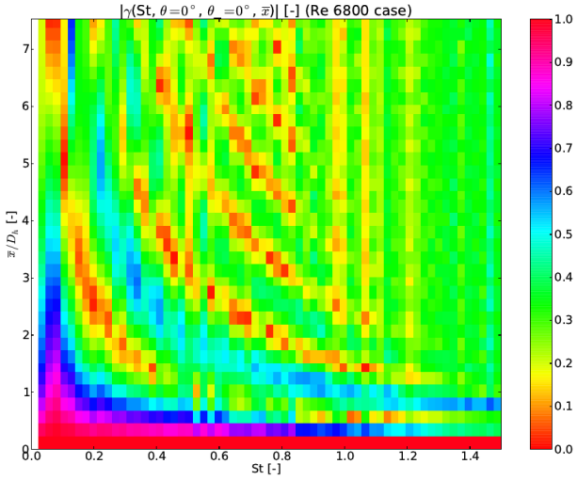

(c) Re 6800 case

Figure 5.5: Contour plots of the coherence amplitude between points in the same gap region, separated over an axial distance, visualizing the influence of the Reynolds number.

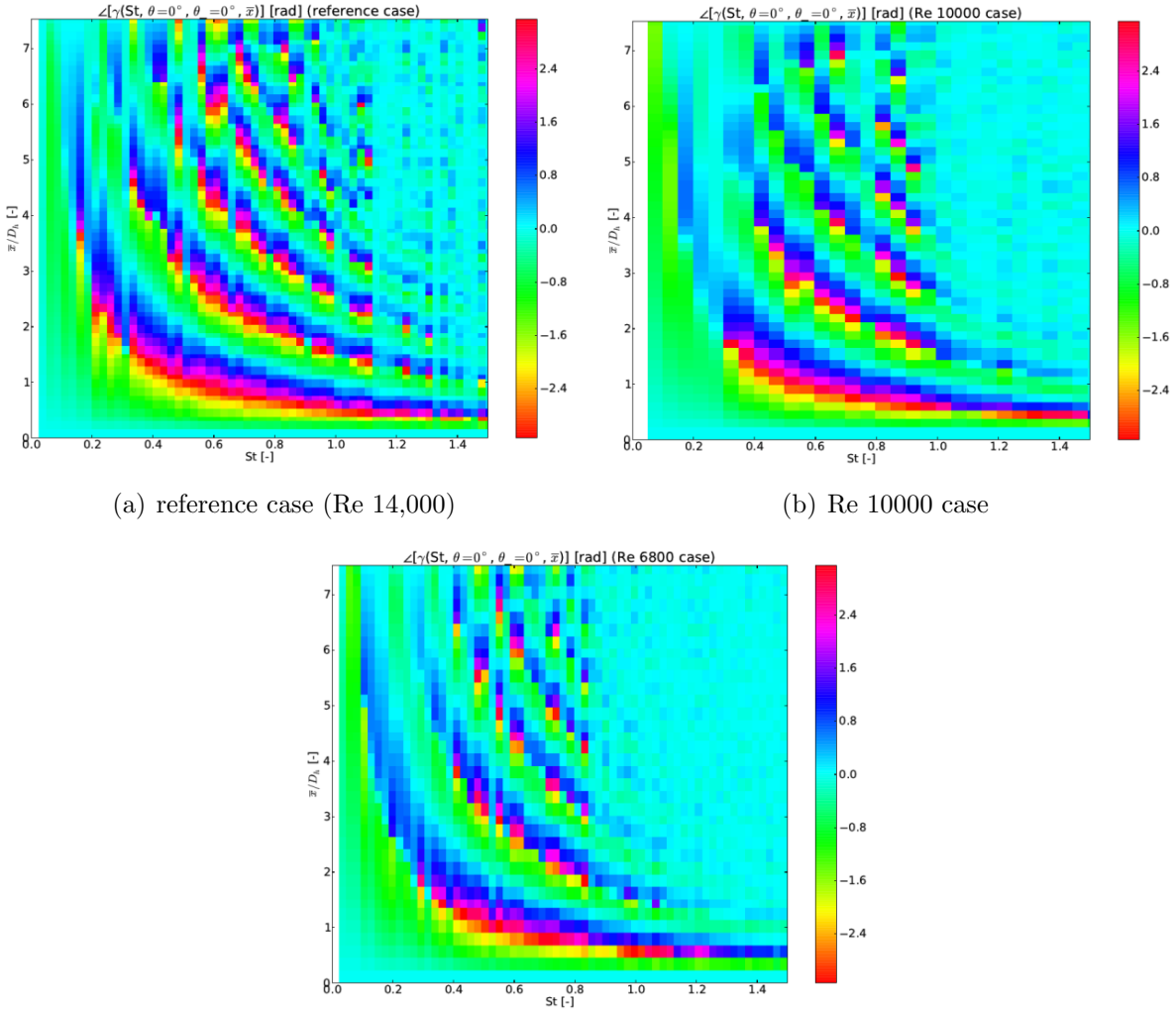

(a) reference case (Re 14,000)

(b) Re 10000 case

(c) Re 6800 case

Figure 5.6: Contour plots of the coherence phase between points in the same gap region, separated over an axial distance, visualizing the influence of the Reynolds number.

5.2 Pitch-over-diameter influence

The second parameter which has been varied, is the pitch-over-diameter ratio. This changes the dimensionless gap width $\frac{P-D}{D}$ in between adjacent cylinders. In the reference case, this $\frac{P}{D}$-ratio equals 1.085. It will be compared to another simulation with a $\frac{P}{D}$-ratio of 1.3, hence referred to as the PD 1.3 case. Their characteristics are given in Table 5.2. As the adapted geometry causes a variation in hydraulic diameter, the length and flow velocity

of the PD 1.3 case have to be adapted as well in order to maintain an $\frac{L}{D_h}$-ratio of 15 (sec. 2.1) and a Reynolds number equal to the one of the reference case. As in the previous section, the $\frac{P}{D}$-ratio is chosen in such a way that it reduces the grid size, hence reducing the computational load. Indeed, the increased free-flow section and decreased flow velocity strongly reduce the pressure gradient over the flow domain length (Table 5.2). This effect, allowing coarser meshes for equal dimensionless wall units, dominates the increase in flow domain, effectively reducing the grid size and computational load.

Figure 5.7 shows the dimensionless wall-pressure PSD distribution over the frequency range and position on the cylinder for the reference and PD 1.3 cases.
The increase in free flow section with increasing $\frac{P}{D}$-ratio strongly reduces the amplitudes of the pressure fluctuations on the cylinder wall. This is concluded by the small PSD amplitude of the PD 1.3 case compared to the reference case. This effect is even larger in absolute values, as the factor normalizing the PSD for the reference case, is 5.5 times as large as the one normalising the PSD for the PD 1.3 case. As stated before, the pressure drop over the PD 1.3 flow domain is much lower than for the reference case. This pressure drop results from wall friction losses and viscous losses. The decrease in wall friction losses is self-evident for larger flow sections, as relatively less friction surface is present. The decrease in viscous losses suggests the absence of a vortex street. Figure 5.8 shows the velocity magnitude and velocity component perpendicular to the main flow along a flow domain side plane. Although there is some randomness present in the flow field, this is entirely attributed to the main flow turbulence. The zigzagging pattern of the velocity magnitude, or the alternating positive and negative velocity spots of the component perpendicular to the wall, have completely disappeared. Hence, the vortex street is no longer present at high $\frac{P}{D}$-ratio geometries. As this vortex street no longer contributes the pressure fluctuations, inherently lower wall-pressure spectra are obtained.
The PSD distribution over the circumferential coordinate also changes with $\frac{P}{D}$-ratio: the maximum amplitude evolves from near the gap region to the center of the subchannel region. At higher $\frac{P}{D}$-ratios, the gap width between the cylinders grows in a relative sense. Therefore, the velocity reduction near the gap region relative to the subchannel flow ve-

Table 5.2: The properties of the cases used to check the $\frac{P}{D}$-ratio influence.

Name	D [m]	P [m]	$\frac{P}{D}$ [-]	D_h [m]	L [m]	$\frac{L}{D_h}$ [-]	U [$\frac{m}{s}$]	Re_{D_h} [-]	$\frac{\Delta p}{L}$ [$\frac{Pa}{m}$]	# cells
reference case	0.2	0.217	1.085	0.1	1.5	15	140	14,000	2570	2,620,800
PD 1.3 case	0.2	0.26	1.3	0.2304	3.5	15	60	14,000	200	1,022,400

locity, is less pronounced, and the importance of the vortex street phenomenon decreases (sec. 1.2.4). The largest vortex density is localized near the region with the largest velocity gradients. The largest velocities are in the largest free-flow section, and as there is no vortex street present, the velocity near the cylinder surface becomes approximately uniform over the entire circumference.Therefore the largest velocity gradients are present in the subchannel region, as are the largest pressure fluctuations.

The coherence amplitude contour plots between points with the same axial coordinate, and one point's circumferential coordinate fixed in the gap or subchannel region, are given in Figures 5.9 and 5.10 respectively.
The figures show a similar distribution of the coherence for both a fixed point in the gap region, and one in the subchannel region. The major difference between the plots is the coherence magnitude: pressure fluctuations in points on different circumferential positions are much more correlated for larger $\frac{P}{D}$-ratios, and this over the entire circumferential and frequency range. In geometries with larger gap widths, more vortices are able to traverse these gaps: the influence of the cylinder walls decreases and the vortices are less quickly dissipated. Due to the boundary conditions, transport through the gap regions allow vortices to reappear at a position 180° shifted to their original position. This way, correlation of pressure fluctuations is overestimated over the entire circumference. This overestimation remains lower for smaller gap widths, as in that situation, fewer vortices are able to cross the gap.
An effect unintentionally introduced when increasing the $\frac{P}{D}$-ratio, is the decrease of the flow velocity U. As in the Re 10000 and Re 6800 cases, where the free flow velocity was reduced, the PD 1.3 case also shows an increased coherence between pressure fluctuations in points with different circumferential coordinates, compared to the reference case. At lower flow velocities, the spanwise length of the vortices is larger and they are able to induce pressure fluctuations over longer circumferential distances. Also, the PSD reduces and noise becomes more important.

The influence of the axial distance between two points in the gap region on the coherence amplitude is shown in Figure 5.11 and on the coherence phase in Figure 5.12.
The low resolution in the PD 1.3 case figures along the vertical axis is because only a small section of the complete flow domain length is shown. This, combined with a low number of cells over the entire axial length of the flow domain, results in very pixelated figures.
A first important difference between the coherence plots of both cases, is the scaling of the vertical axis. In the PD 1.3 case figures, the maximum $\frac{\overline{x}}{D_h}$ shown is much smaller than in

the reference case. This is done on purpose: because of the larger hydraulic diameter of the PD 1.3 case, a certain $\frac{\overline{x}}{D_h}$ value corresponds with a larger $\overline{x}$, compared to the reference case. As was stated in section 4.2.3, the coherence between pressure fluctuations in two points quickly vanishes as the axial distance between them grows. If the coherence plots of the PD 1.3 case were given over half of the flow domain length, as is done for the reference case, only the lower part of the graph would contain meaningful information, while the rest would contain only noise.
Apart from the vertical axis scaling, the plots for the coherence amplitude and phasing correspond well for both cases. The only significant influence of the $\frac{P}{D}$-ratio on the axial coherence is the reduced distance over which pressure fluctuations are correlated.

To summarize, in geometries with larger $\frac{P}{D}$-ratios, the vortex street phenomenon decreases in importance, or even disappears completely. This causes the pressure fluctuations to strongly reduce in amplitude, and the maximum pressure amplitude shifts away from the gap region towards the subchannel region.
The coherence amplitude increases over the entire frequency and circumferential range for increasing $\frac{P}{D}$-ratio, although this might also be due to the lowered flow velocity needed to maintain a certain Reynolds number, and an increase in noise. Also, for increasing $\frac{P}{D}$-ratio, vortices and consequently pressure fluctuations, are less coherent over the same distance downstream.

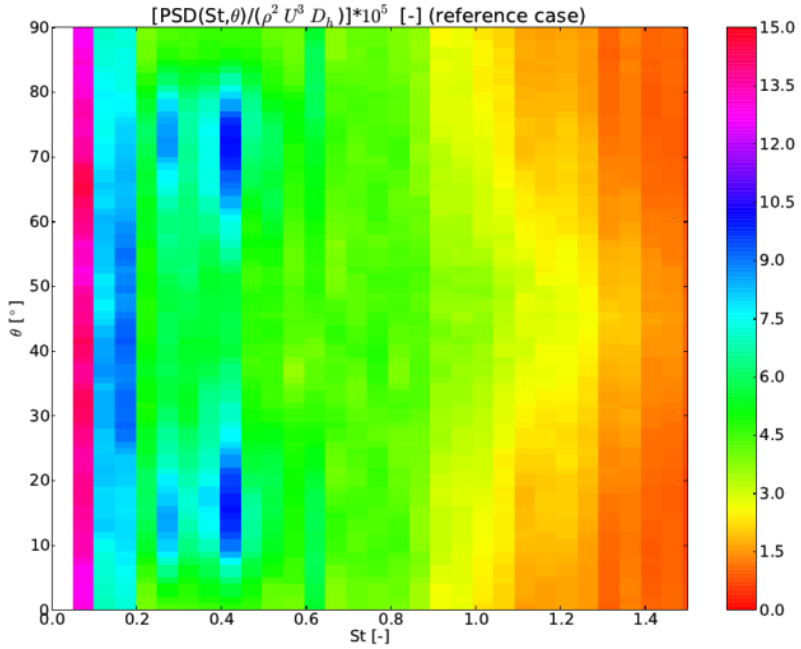

(a) reference case (PD 1.085)

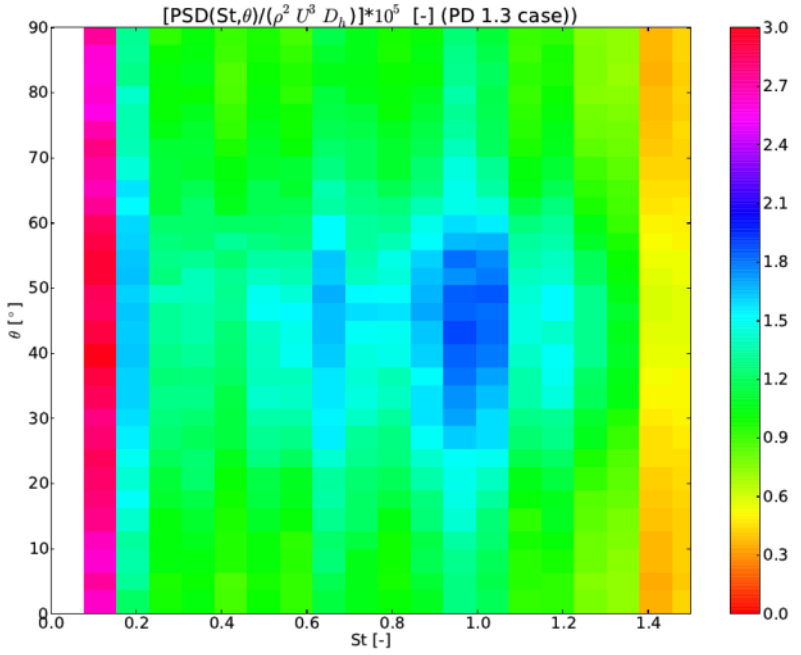

(b) PD 1.3 case

Figure 5.7: Contour plots of the dimensionless PSD as a function of the position on the cylinder and Strouhal number, visualizing the influence of the $\frac{P}{D}$-ratio.

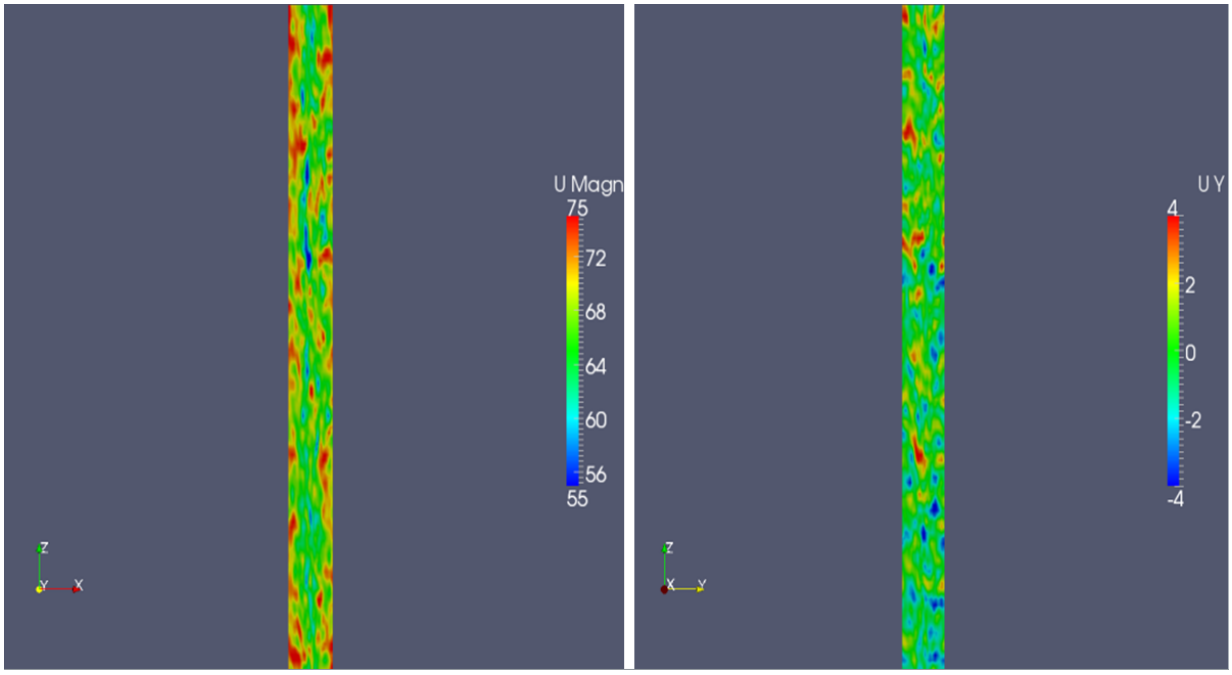

Figure 5.8: Velocity magnitude (left) and velocity component perpendicular to the main flow (right) along a flow domain side plane.

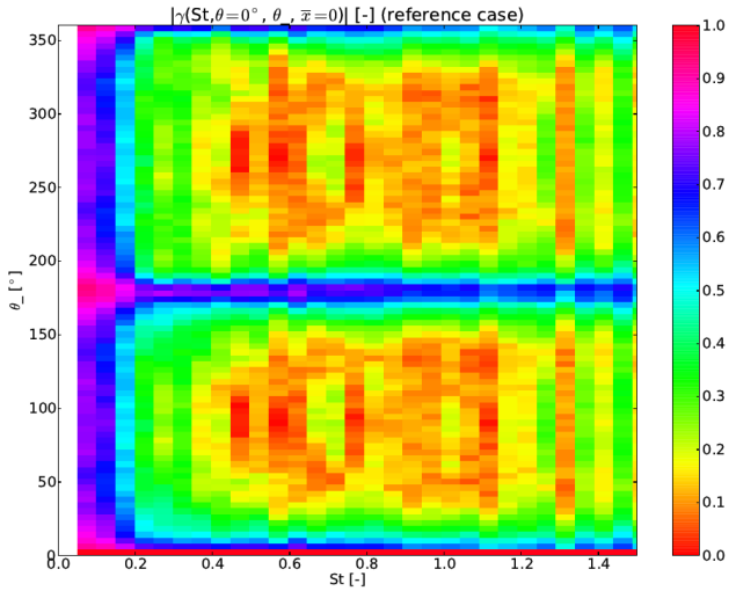

(a) reference case (PD 1.085)

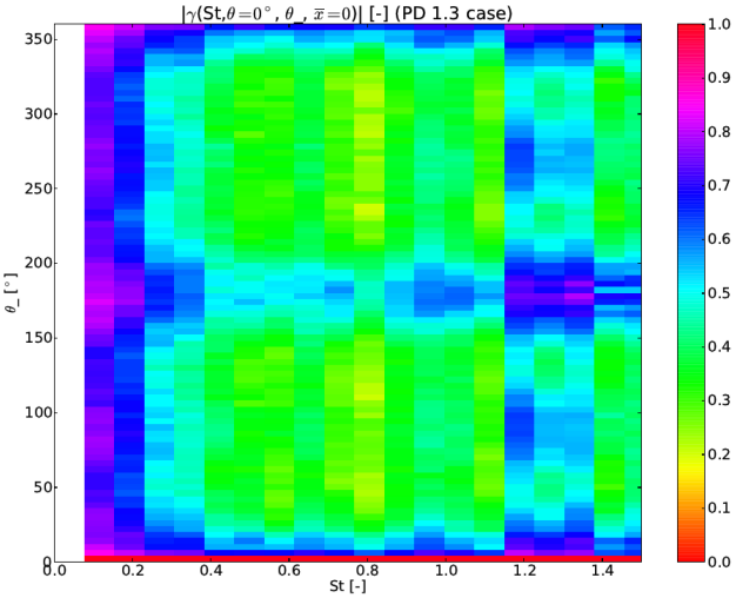

(b) PD 1.3 case

Figure 5.9: Contour plots of the coherence amplitude between points at the same axial position, and one point's circumferential position fixed in the gap region, visualizing the influence of the $\frac{P}{D}$-ratio.

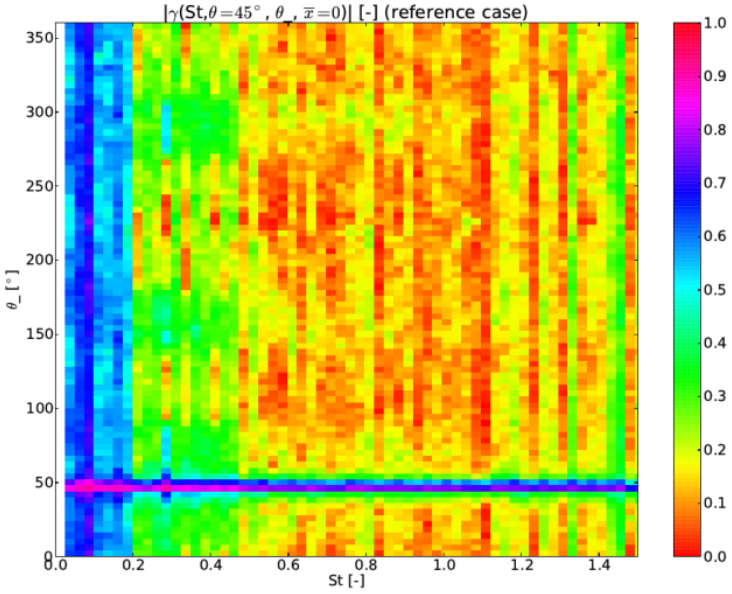

(a) reference case (PD 1.085)

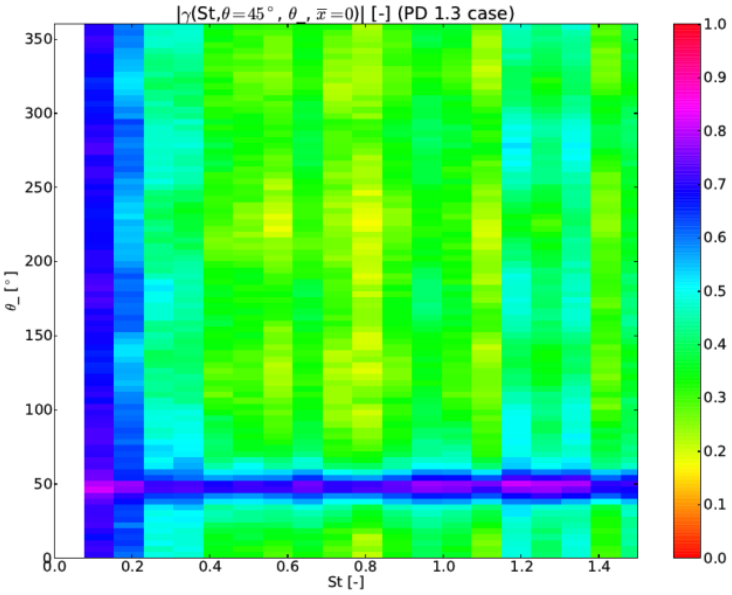

(b) PD 1.3 case

Figure 5.10: Contour plots of the coherence amplitude between points at the same axial position, and one point's circumferential position fixed in the subchannel region, visualizing the influence of the $\frac{P}{D}$-ratio.

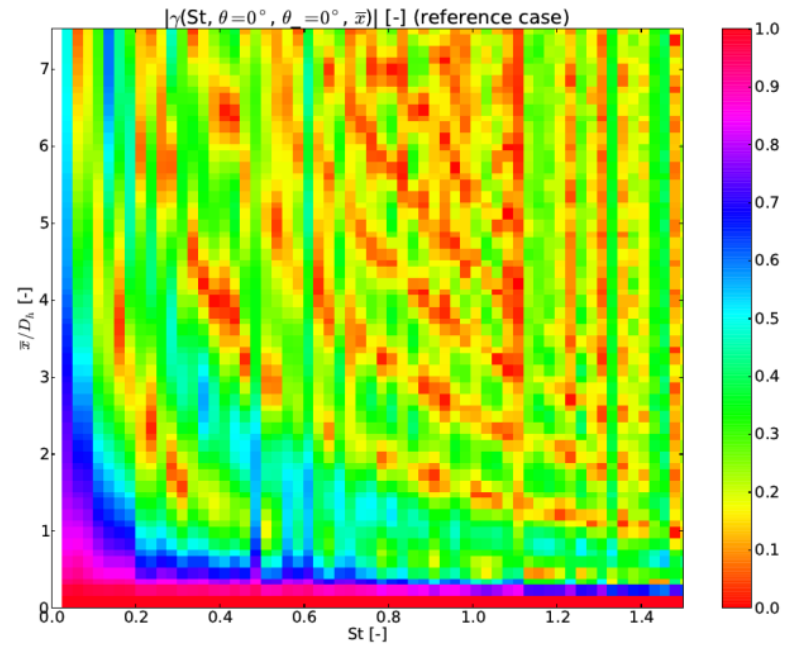

(a) reference case (PD 1.085)

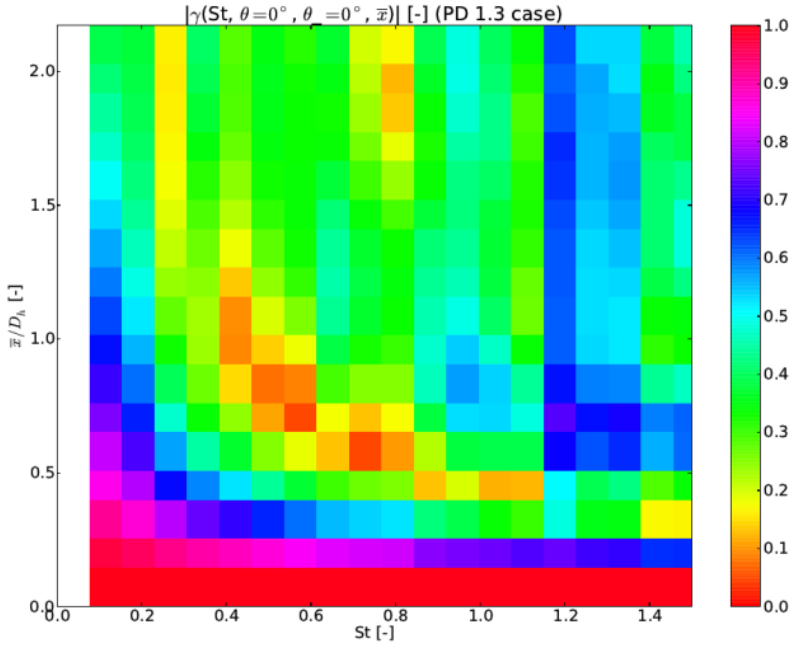

(b) PD 1.3 case

Figure 5.11: Contour plots of the coherence amplitude between points in the same gap region, separated over an axial distance, visualizing the influence of the $\frac{P}{D}$-ratio.

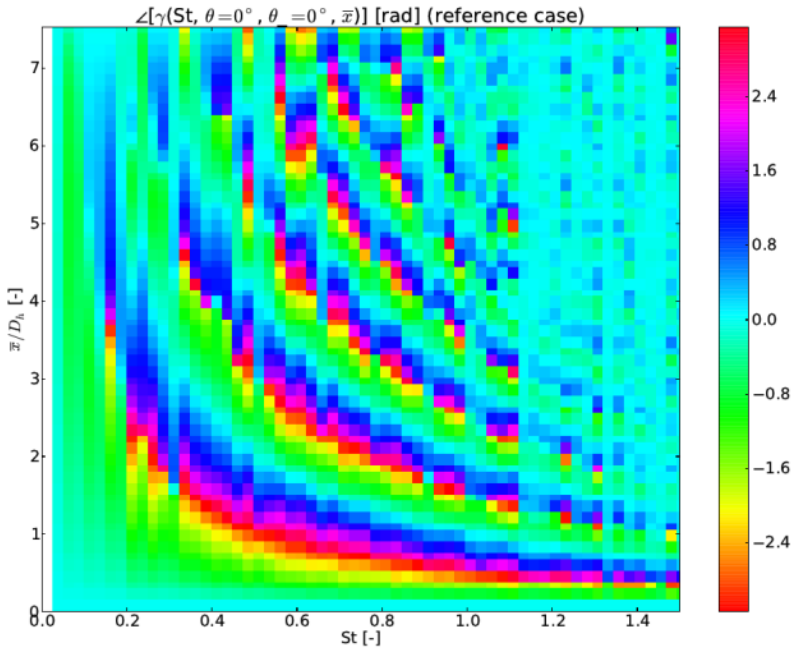

(a) reference case (PD 1.085)

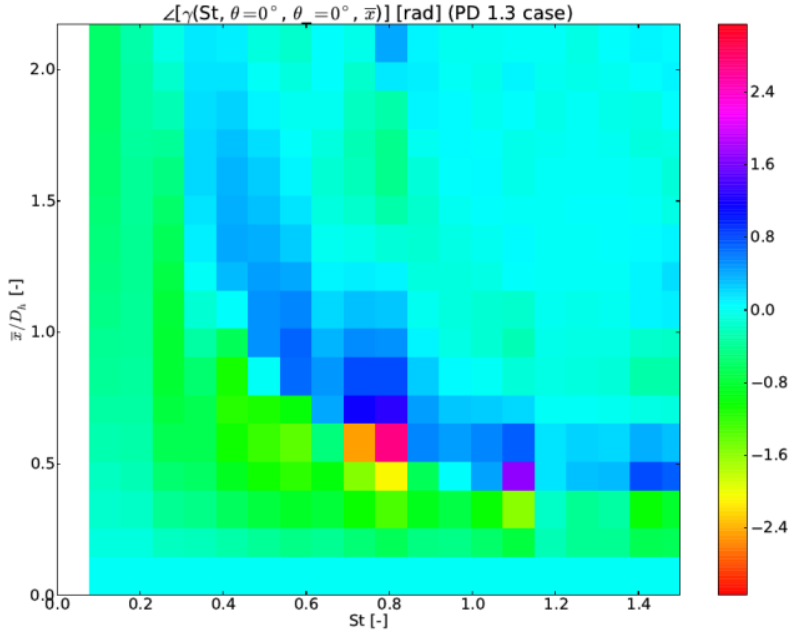

(b) PD 1.3 case

Figure 5.12: Contour plots of the coherence phase between points in the same gap region, separated over an axial distance, visualizing the influence of the $\frac{P}{D}$-ratio.

5.3 Array configuration influence

The final parameter whose influence on the spectra is discussed, is the array configuration. In the introduction (sec. 1.1) it was already pointed out that apart from square arrays, triangular arrays are often encountered nuclear reactor cores. In this section, the major differences in pressure amplitude and frequency distribution on the cylinder surfaces are studied, for a square array represented by a square flow domain, and a triangular array represented by a hexagonal flow domain (Fig. 2.1). The most important characteristics are given in Table 5.3
Because of the different geometric outline of the flow domains, it is impossible to vary only one parameter. For the hexagonal case, a cylinder and hydraulic diameter equal to the ones of the reference case are chosen. However, by fixing these variables and postulating a Reynolds number equal to the one of the reference case, the pitch inevitably changes. This causes pitch-over-diameter effects, described in section 5.2, to disturb the results. The influence of the array configuration can not be fully extracted by this comparison, but an attempt is made nevertheless.
Note that for the hexagonal case, there are 6 gap and subchannel regions present. Also, a shift of the spectra over 60° results in a similar spectrum (sec. 2.5.2).

The PSD spectra for both array configurations are given in Figure 5.13. The spectrum for the hexagonal case is only given up to $\theta = 60°$ due to symmetry reasons.
From the PSD spectra, the influence of the array configuration can not unambiguously be extracted. All the features present in the PSD plots - the lower PSD amplitude over the entire frequency and circumferential range, the PSD peak shifted towards the subchannel region - are also found in the previous section. Therefore, these features are attributed to a variation in the $\frac{P}{D}$-ratio between the cases.

The cross-correlation between different points, displaced over a circumferential distance, is evaluated by the coherence magnitude and is given in Figure 5.14 for a fixed circumferential coordinate in the gap region, and Figure 5.15 for a fixed circumferential coordinate in the

Table 5.3: The properties of the cases used to check the array configuration influence.

Name	Configuration	D [m]	P [m]	$\frac{P}{D}$ [-]	D_h [m]	U $[\frac{m}{s}]$	Re_{D_h} [-]	# cells
reference case	square	0.2	0.217	1.085	0.1	140	14,000	2,620,800
hexagonal case	triangular	0.2	0.2332	1.166	0.1	140	14,000	1,821,600

subchannel region.
Figure 5.14(b) shows what was to be expected, based on previous observations: a coherence amplitude equal to one where $\theta = \theta'$ because of the coherence definition (eq. 1.14), an increase in coherence between pressure fluctuations in opposite gap regions because of the periodic boundary conditions, and an increased coherence over the entire circumferential and frequency range compared to the reference case (Fig. 5.15(a)) due to the increase in $\frac{P}{D}$-ratio.
The enhanced coherence at $\theta' = 60°$ in Figure 5.15(b) is probably an error. An equally large coherence should be present in the gap region on the other cylinder side ($\theta' = 0°$), otherwise the plot would not be symmetrical along the geometric symmetry axis on which the fixed point is located ($\theta = 30°$).

The influence of the axial distance on the cross-correlation between two points in the gap region, is evaluated by the coherence amplitude and phase plots in Figures 5.16 and 5.17 respectively.
The low resolution in the hexagonal case figures along the vertical axis is because only a small section of the complete flow domain length is shown. This, combined with a low number of cells over the entire axial length of the flow domain, results in very pixelated figures, and makes comparison between the array configurations difficult.
Although the hydraulic diameter is the same for both cases, the vertical axis of the hexagonal case plots had to be rescaled because of the low levels of coherence and high levels of noise present at high $\frac{\overline{x}}{D_h}$. The pressure fluctuations are correlated over significantly shorter distances, compared to the reference case. The evolution of the coherence over the axial distance and frequency is however quite similar for both configurations. Also note that the plots are given on dimensionless axes, but because of the geometric and flow similarities between the two cases, the axes are normalised with the same coefficient. Hence, the plots could also be displayed on the same dimensional axes.

The only influence of the array configuration that was extracted by previous analysis, is that for triangular arrays, vortices and pressure fluctuations are correlated over significantly shorter distances downstream. The thesis mainly focusses on square arrays, and this excursion to triangular arrays was only a first attempt. Further study might be necessary.

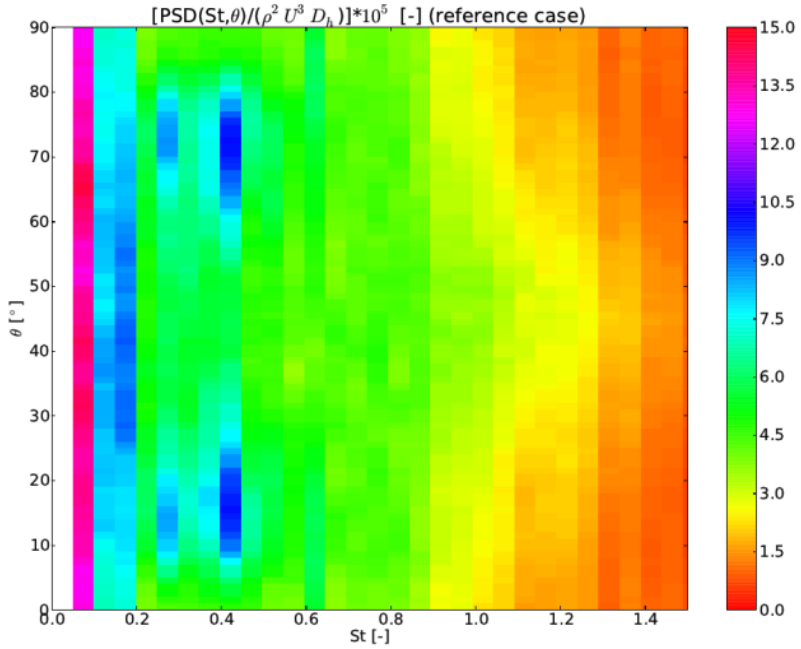

(a) square array configuration

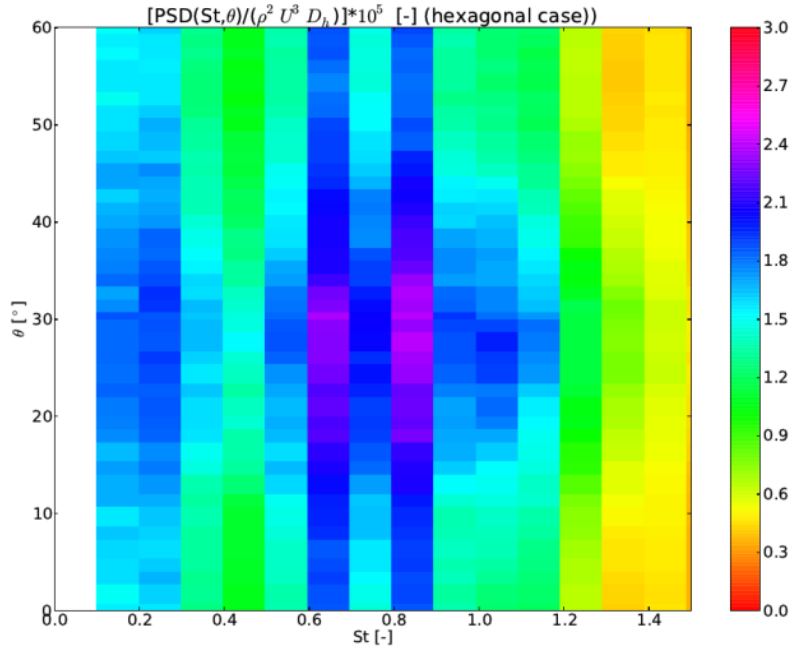

(b) triangular array configuration

Figure 5.13: Contour plots of the dimensionless PSD as a function of the position on the cylinder and Strouhal number, visualizing the influence of the array configuration.

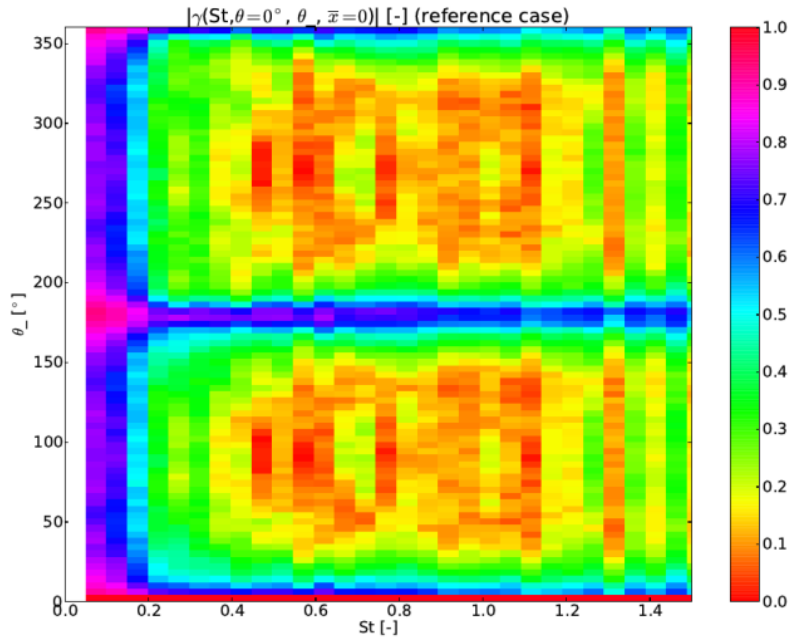

(a) square array configuration

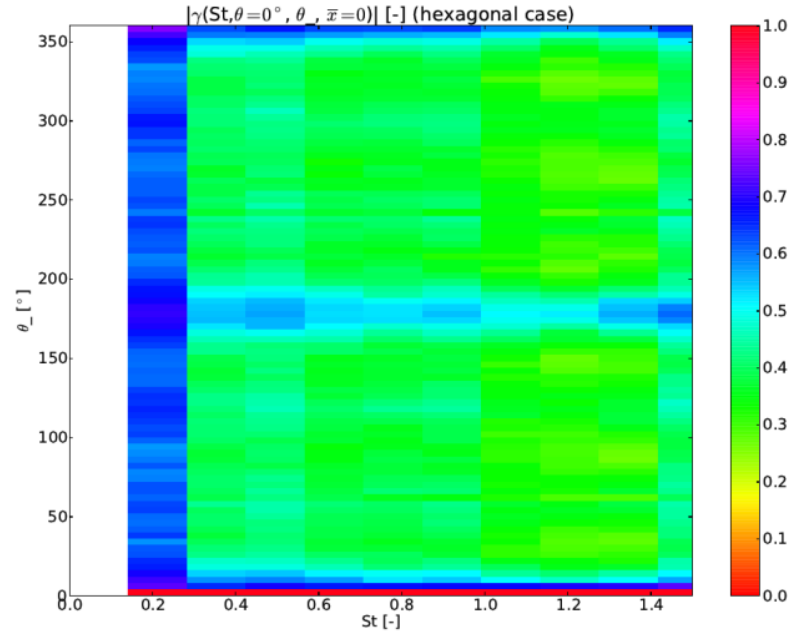

(b) triangular array configuration

Figure 5.14: Contour plots of the coherence amplitude between points at the same axial position, and one point's circumferential position fixed in the gap region, visualizing the influence of the array configuration.

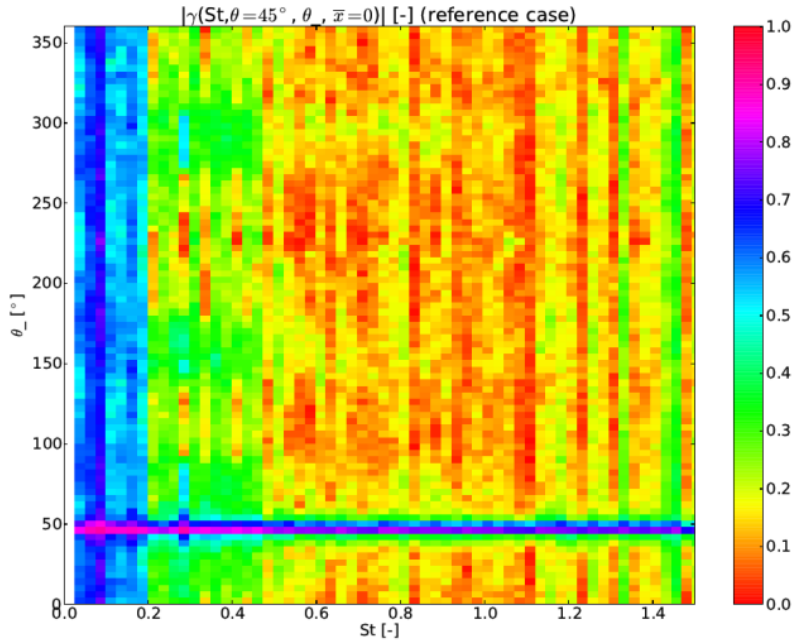

(a) square array configuration

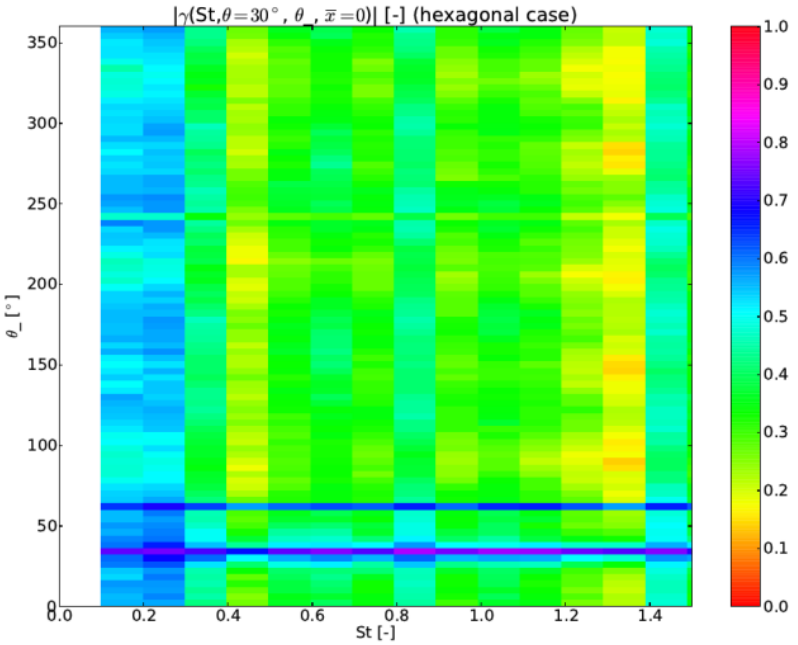

(b) triangular array configuration

Figure 5.15: Contour plots of the coherence amplitude between points at the same axial position, and one point's circumferential position fixed in the subchannel region, visualizing the influence of the array configuration.

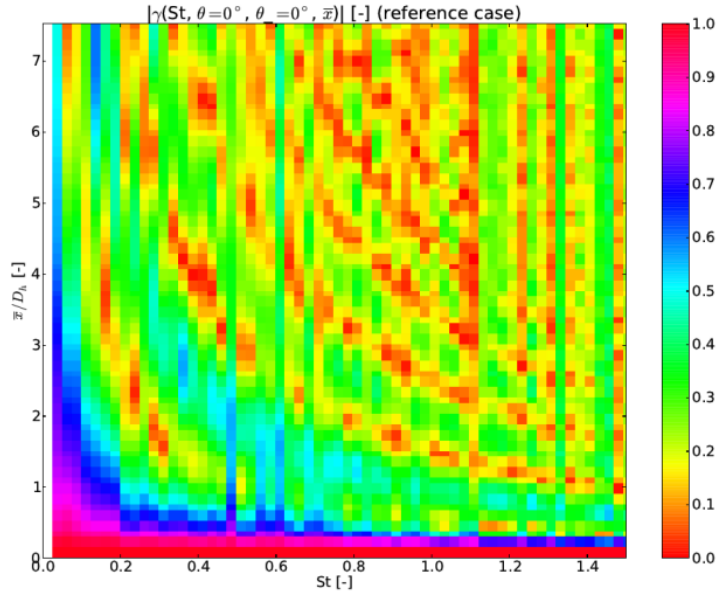

(a) square array configuration

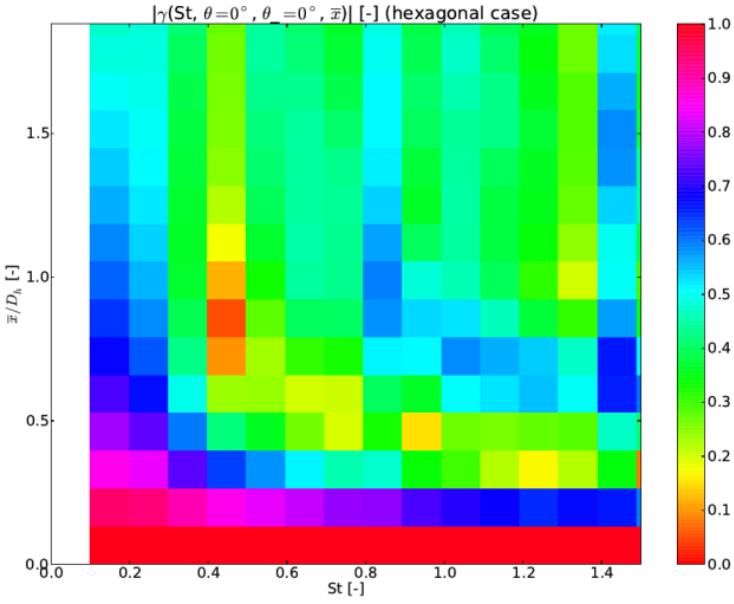

(b) triangular array configuration

Figure 5.16: Contour plots of the coherence amplitude between points in the same gap region, separated over an axial distance, visualizing the influence of the array configuration.

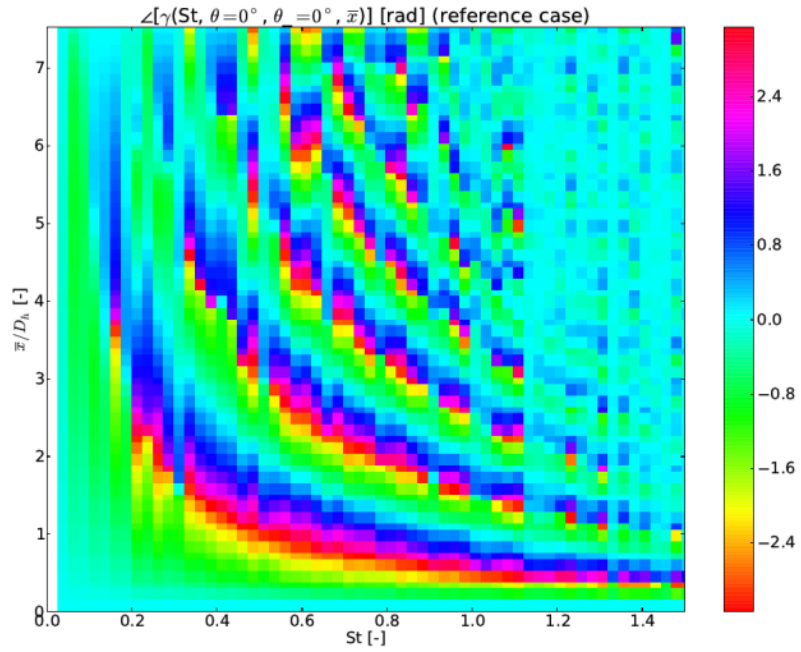

(a) square array configuration

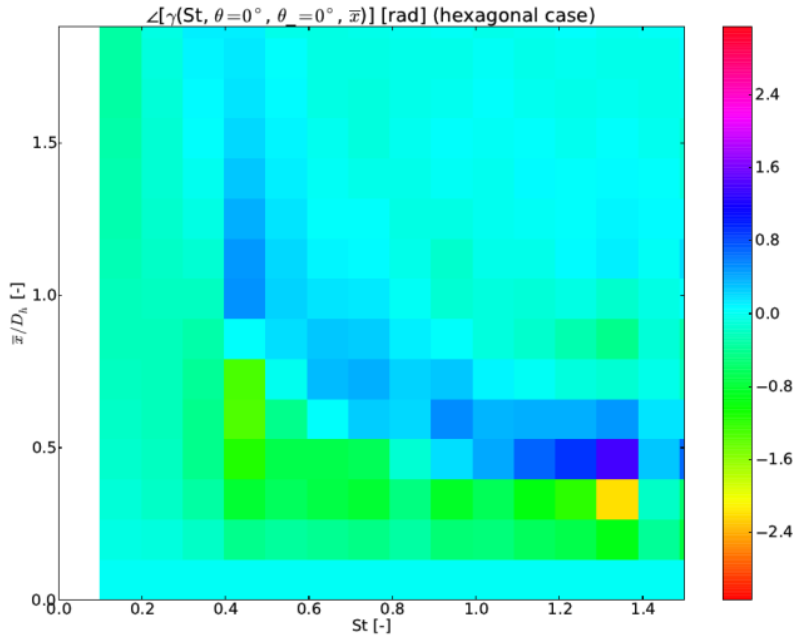

(b) triangular array configuration

Figure 5.17: Contour plots of the coherence phase between points in the same gap region, separated over an axial distance, visualizing the influence of the array configuration.

5.4 Conclusions

In the final section of this chapter, the conclusions regarding the Reynolds number, $\frac{P}{D}$-ratio and array configuration influence on the pressure spectra are listed. This is a brief summary of the results without further explanation, as all conclusions are already extensively discussed and explained in the previous sections.

The global pressure fluctuation amplitude is mostly influenced by the Reynolds number of the flow and the $\frac{P}{D}$-ratio of the array geometry. Either decreasing the Reynolds number or increasing the array spacing results in a decrease in pressure loss over a certain length. By decreasing the Reynolds number, the shear stresses on the cylinder wall reduce, and the vortices present in the flow are weaker and fewer in number. The increased $\frac{P}{D}$-ratio increases the free-flow section, hence the lower pressure drop.
As with a lower pressure drop, lower viscous losses and a weaker vortex street corresponds, it can be concluded that the vortices or turbulence in the flow is less strong, and the pressure fluctuation amplitudes decrease for decreasing Reynolds number and increasing $\frac{P}{D}$-ratio.
The influence of the array configuration on the pressure fluctuations could not be extracted.

The pressure fluctuation amplitude distribution over the cylinder surface is independent of Reynolds number, but heavily influenced by array geometry. As the spacing between the cylinders increases, the vortex street phenomenon decreases in importance. At low $\frac{P}{D}$-ratios, the vortex street is present and stronger pressure fluctuations are located on the axis along which the street is convected. At high $\frac{P}{D}$-ratios, the peak pressures shift towards the subchannel region. The strongest vortices are present at the location where the velocity gradient is the strongest. If a strong vortex street is present, this is near the gap region. If the vortex street is absent, this is in the subchannel region.
As a result of the reduced PSD at these conditions, the influence of the noise also increases, increasing the coherence amplitude over the entire frequency and circumferential range.
The influence of the array configuration on the circumferential coherence could not be extracted.

Cross-correlation between pressure fluctuations in circumferentially separated points, becomes higher for decreasing Reynolds number and increasing $\frac{P}{D}$-ratio. For both, the reduced flow velocity allows the vortices to span longer distances perpendicular to the main flow. Therefore, they can induce pressures over longer circumferential distances. At lower

Reynolds numbers, or larger gap widths, the flow experiences less pressure loss when traversing the gap region. More vortices are able to cross the gap and induce pressure fluctuations on the other side, correlating these pressures.

The correlation between pressure fluctuations shifted over axial distances, only changes when switching array geometry. For both triangular arrays and increased $\frac{P}{D}$-ratios, the pressure fluctuations are correlated over significantly smaller distances. On an absolute frequency scale, the bands present in the coherence amplitude spectra are more closely spaced for decreasing flow velocity and increasing hydraulic diameter (or increasing free-flow section). The Strouhal number is defined as $St = \frac{fD_h}{U}$, thus the frequency becomes $f = \frac{StU}{D_h}$.
These phenomena can be explained by the convection of vortices: at lower flow velocity, the eddy turn-over time increases, and the vortices complete more periods over shorter axial distances, hence their phase drops more quickly in an absolute sense. The bands in the spectra then are more closely spaced.

Chapter 6

Conclusion

In this thesis, the forces on a cylinder bundle, induced by an axial flow, are evaluated by computing the frequency spectra of the pressures on the cylinder walls. These pressures need to be limited to avoid excessive cylinder vibration, causing failure in the long run. The influence of the position, Reynolds number, cylinder pitch-over-diameter ratio, and array configuration on the pressure fluctuation amplitude and frequency are extracted by performing LES simulations on a flow domain containing a single cylinder.

The highest pressures were generated by the large scale vortices and have low fluctuation frequencies. The majority of these high pressures are generated by a vortex street: an alternating sequence of large scale eddies, transporting mass, momentum and energy between adjacent subchannels. This vortex street is formed by a Kelvin-Helmholtz instability between the mixing layer of the high flow velocity in the subchannel region, and the lower flow velocity in the gap.
The amplitude of higher pressure fluctuation frequencies first decreases, independent of the position on the cylinder, then increases to a maximum at a Strouhal number between 0.25 and 0.45, whereafter it again decreases and approaches zero. The position of the maximum, both in space and frequency, is dependent on the array geometry, more specifically the distance between adjacent cylinders. The spectrum extends to higher frequencies in the subchannel region.
Larger pressure drops over a unit length correspond to globally higher amplitude pressure fluctuations over the entire cylinder surface, as they indicate the presence of large amounts of strong vortices or a vortex street. Therefore the pressure amplitudes increase with increasing Reynolds number, and more closely spaced cylinders.

The cross-correlation between pressures induced in points on the same and different cylinders at different circumferential positions, proofs to be dependent on the positions of the points. Pressures in points near gaps in between cylinders are only correlated with pressures in other points in that same gap, or in the gap on the other side of the subchannel. However, the latter is mainly due to an artefact introduced by the boundary conditions. Pressures in points on the cylinder in the subchannel region, are highly correlated with pressures in points near the same channel on adjacent cylinders, but only for low frequency fluctuations.
The cross-correlation between pressure fluctuations, globally increases in magnitude with decreasing Reynolds number and less closely spaced arrays.

Pressures induced in points at the same circumferential position, but separated axially, are highly correlated at low frequency and low axial spacing combinations, due to the dissipation of vortices. In these spectra, alternating bands between maximum and zero coherence are present. This results from the convection of vortices with the flow.
For more open geometries, and triangular array configurations compared to square ones, the distance over which vortices are coherent is significantly smaller.

The highest pressure fluctuations are obtained for high Reynolds number flows in closely spaced arrays. While disadvantageous for the structural safety, these conditions are wanted for high efficiency in compact geometries.
As the highest pressure amplitudes are generated by the largest vortices, it is advised to avoid these large scales by introducing mechanical obstructions in the flow, breaking these vortices. However, the vortex street is the main source of mass, momentum and heat transfer between adjacent subchannels, and therefore is desired for good heat transfer.
A trade-off between structural safety, spatial compactness, and heat transfer efficiency, is inevitable.

Chapter 7

Discussion

In the final chapter of the thesis, comments on the obtained results are given. The shortcomings of this research are described, and suggestions are made for improving further research on similar subjects.
Some phenomena observed in the simulations that are not further described in the main text because of time pressure or irrelevancy to the subject, are quickly listed here. Let them be a starting point for further research.

7.1 Shortcomings and suggestions

As the simulation method employed in this thesis is LES, there are inevitably some errors induced due to the modelling of small vortices instead of resolving them. Instead DNS analyses can be performed, or a finer grid, especially in the flow direction (Fig. 3.2), can be used. This way, more accurate result can be obtained, and pressure fluctuations at higher Strouhal numbers can be studied.
Previous suggestions inherently give rise to larger grid sizes and higher computational loads. Another possibility to obtain smaller wall units without increasing the grid size, is simulating lower Reynolds numbers or geometries with larger $\frac{P}{D}$-ratios. This way, the characteristic length scale increases and coarser grids correspond with equal dimensionless wall units (sec. 5.1 & 5.2). Although, the turbulence decreases with decreasing Reynolds number, the vortex street is still present at low Reynolds numbers (sec. 1.2.4).

The influence of the boundary conditions should be reduced in further research. Periodic boundary conditions between inlet and outlet plane posed no problem. Because of the suffi-

ciently long flow domain and coherences between pressure fluctuations in axially separated points disappearing for larger distances, this has no significant influence on the solution, and even proved to be a good method to reduce the grid size. The influence of the periodic boundary conditions on opposite side planes, however, was clearly visible in the spectra.
Because in the author's opinion, no boundary condition is better fit to simulate the continuity of the cylinder array, starting from a flow domain enveloping one cylinder, further research should simulate multiple cylinders. Although this implies a much larger flow domain, grid size, and computational load, it is believed that the obtained results will more accurately describe the flow behaviour in a real array. Additionally, coherence spectra will no longer be limited to two points, adjacent to the same subchannel.

Because of the large grid size and consequently high computational load, the representativity of the flow domain containing one cylinder, to the entire array, was not verified. It might be necessary to check the representativity before continuing cylinder array research on one-cylinder flow domains.

Some figures of spectra, given in chapters 4 and 5, are of poor resolution. The resolution along θ or $\overline{x}$ axes can be improved by refining the grid in circumferential or longitudinal direction respectively. This way, more points are available at which the pressure is evaluated. However, this method also incurs higher computational loads, as the grid size is increased.
The resolution along the St axis is limited by the Nyquist theorem (sec. 1.3.1). The number of frequencies at which the pressure is evaluated, can be increased by obtaining data over a longer time. Again, the computational load increases because the simulations now have to run longer. Another approach is decreasing the amount of time-averaging: the length of the time intervals becomes longer, as the time over which data is obtained is chopped into fewer batches. However, this increases the contribution of outliers and spectral variance becomes important.

As this thesis focusses on square arrays, and only a quick excursion to triangular arrays was made, further research on flow induced vibrations on triangular array configurations, subjected to axial flow, is encouraged. Especially the influence of the array configuration on the pressure spectra is of interest, as the extraction of this parameter was not a success.

7.2 Undescribed phenomena

A first phenomenon, encountered in the simulations but not described in the thesis, is the lossless transmittance of the pressures through the boundary layer. Figure 7.1 shows this. Note that in this figure, the z axis is parallel with the flow velocity, in contrast to the x axis being perpendicular to the flow velocity in other parts of the thesis. On the left are the contours of the pressures on one of the side walls. On the right is the same view, but this time of the pressure contours on the cylinder surface. The similarity between both figures is striking.
This transmittance of pressures through the boundary layer originates from boundary layer analysis. The pressures are transported at the speed of sound in the fluid. For incompressible fluids, as used in this thesis, the speed of sound becomes infinite and pressures are transmitted instantaneously.

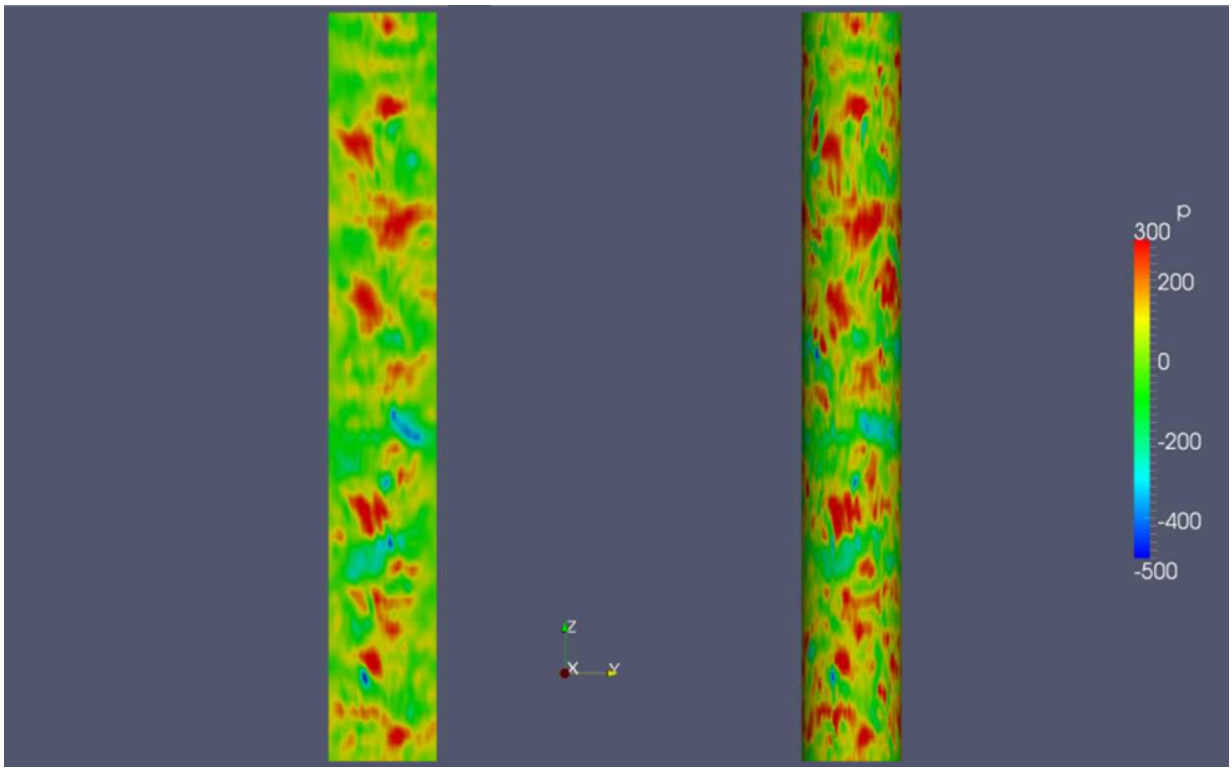

Figure 7.1: The pressure distribution on the flow domain side wall (left) and cylinder surface (right).

Another phenomenon, mentioned a few times in the main text, is the vortex street. These

vortex street enhance mixing and heat transfer in closely spaced arrays, even at low Reynolds numbers and low pressure drops. A study further investigating this vortex street phenomenon in cylinder arrays, and their practical application, seems in place.

Bibliography

[1] J. S. Bendat & A. G. Piersol, (2010), Random Data: Analysis and Measurement Procedures, 4^{th} edition, Wiley

[2] L.C. Berselli & T. Ileiscu & W. J. Layton, (2006), Mathematics of large eddy simulation of turbulent flows, Springer, Germany

[3] J. Bredberg, (2000), On the Wall Boundary Condition for Turbulence Models, Chalmers University of Technology, Göteborg (Sweden)

[4] S. Y. Chung & G. H. Rhee & H. J. Sung, (2002), Direct numerical simulation of turbulent concentric annular pipe flow Part 1: Flow field, International Journal of Heat and Fluid Flow 23 (2002) 426-440

[5] L. R. Curling & M. P. Paidoussis, (1991), Measurements and characterisation of wall-pressure fluctuations on cylinders in a bundle in turbulent axial flow; Part 1: Spectral characteristics, Journal of Sound and Vibration (1992) 157 (3) pg 405-433

[6] J. De Ridder & J. Degroote & K. Van Tichelen et. al, (2015), Predicting turbulence-induced vibration in axial annular flow by means of large-eddy simulations, Journal of Fluids and Structures, Draft under review

[7] M. Di Paola & F. P. Pinnola, (2012), Cross-power spectral density and cross-correlation representation by using fractional spectral moments, Meccanica dei meteriali e delle Strutture vol 3 no. 2, pg 9-16

[8] Germano et. al., (1991), A dynamic subgrid-scale eddy viscosity model, Physics of Fluids A 3 (7): pg 1760-1765

[9] M. S. Guellouz & S. Tavoularis, (2000), The structure of turbulent flows in a rectangular channels containing a cylindrical rod, Experimental Thermal and Fluid Science 23, pg 59-91

[10] G. Heinzel & A. Rüdiger & R. Schilling, (2002), Spectral and spectral density estimation by the Discrete Fourier Transform (DFT), including a comprehensive list of window functions and some new flat-top windows, Max-Planck-Institut für gravitationphysik, Hannover (Germany)

[11] M. Loccufier, (2014), Mechanical Vibrations, Ghent university, Ghent (Belgium)

[12] C. Meneveau & T. S. Lund & W. H. Cabot, (1995), A Lagrangian dynamic subgrid-scale model of turbulence, J. Fluid Mech. (1996) vol. 319 pg 353-385

[13] L. Meyer, (2010), From discovery to recognition of periodic large scale vortices in rod bundles as source of natural mixing between subchannels - a review, Nuclear Engineering and Design 240 (2010) 1575-1588

[14] S. V. Moller, (1991), On phenomena of turbulent-flow through rod bundles, Experimental Thermal and Fluid Science 4, pg 25-35

[15] M. P. Paidoussis, (2004), Fluid-structure interactions: slender structures and axial flow, Volume 2, Elsevier academic press, London, Great Britain

[16] U. Piomelli, (2012), Large-eddy simulation of turbulent flows part 1: introduction, Von Karman institute for fluid dynamics: lecture series 2012, Lecture in Sint-Genesius-Rode, Belgium

[17] J. Vierendeels, (2013-2014), Fluid Mechanics, course material, Ghent university, Ghent (Belgium)

[18] E. Merzari & P. Fisher & K. Van Tichelen et. al., (2015), Benchmark Exercise for Fluid Flow Simulations in a Liquid Metal Fast Reactor Fuel Assembly, Nuclear Engineering & Design, under review

[19] Blockmesh grading calculator, `https://openfoamwiki.net/index.php/Scripts/blockMesh_grading_calculation`, 20/12/2014

[20] Cell size at the wall, Card BPG 3, `http://code-saturne.org/cms/sites/default/files/file_attach/BPG/BPG-3-Cell-Size-At-The-Wall.pdf`, 15/04/2015

[21] `http://www.eng.utah.edu/~mcmurtry/Turbulence/turblt.pdf`, 16/05/2015

Appendix A

Curling's CSD-correlation

The formula for Curling's dimensionless CSD-correlation is (ref. [5])

$$
\begin{aligned}
CSD\ \ (St,\theta,\theta',\overline{x}) = \\
& b_s\left[a\left(\tfrac{2\theta_d}{\pi}\right)^2 sin\left(\tfrac{\pi\theta_d}{l}\right) - \left(1+a\cdot sin\left(\tfrac{\pi^2}{2l}\right)\right)\left(\tfrac{2\theta_d}{\pi}\right)^3\right] \\
& \cdot\left[exp\left(-0.7\tfrac{St}{D_h}\left|\overline{x}\right|\right)\left[1+\left(exp\left(-0.2\tfrac{St}{D_h}\left|\overline{x}\right|\right)-1\right)sin^2\left(2\theta'\right)\right]\right] \\
& \cdot\sqrt{1-sin^2\left(2\theta\right)\left[0.36-50St^3exp\left(-3St^2\right)\right]} \\
& \cdot\sqrt{1-sin^2\left(2\theta'\right)\left[0.36-50St^3exp\left(-3St^2\right)\right]} \\
& \cdot\left(\left[\left(1-\left(\tfrac{St}{3}\right)^2\right)^2+\left(2\zeta_1\tfrac{St}{3}\right)^2\right]^{-\frac{1}{2}}+31.986\left[\left(1-\left(\tfrac{St}{0.1349}\right)^2\right)^2+\left(2\zeta_2\tfrac{St}{0.1349}\right)^2\right]^{-\frac{1}{2}}\right) \\
& \cdot\left[Re^{-1}exp\left(-j2\pi\tfrac{1+0.05sin^2(2\theta')}{1.129}\tfrac{St}{D_h}\overline{x}\right)\right]\ .
\end{aligned}
\tag{A.1}
$$

This correlation is valid for Strouhal numbers larger than 0.25. The used coefficients are

$$
\begin{aligned}
& b_s = 0.305 \\
& a = \tfrac{7.68}{8+St^3} \\
& \theta_d = \left|\theta'-\theta\right| - \tfrac{\pi}{2} \\
& l = 0.384St^3 + 0.899 \\
& \zeta_1 = 0.6 \\
& \zeta_2 = 8.68582\ .
\end{aligned}
\tag{A.2}
$$

Assessment of the force spectrum induced by turbulence on an array of cylinders in incompressible axial flow

Pieter Aerts

Supervisors: Prof. dr. ir. Joris Degroote, Prof. dr. ir. Jan Vierendeels
Counsellor: Ir. Jeroen De Ridder

Master's dissertation submitted in order to obtain the academic degree of
Master of Science in Electromechanical Engineering

Department of Flow, Heat and Combustion Mechanics
Chairman: Prof. dr. ir. Jan Vierendeels
Faculty of Engineering and Architecture
Academic year 2014-2015

UNIVERSITEIT
GENT